Comprehensive Analysis of the Geoeffective Solar Event of 21 June 2015: Effects on the Magnetosphere, Plasmasphere, and Ionosphere Systems

Mirko Piersanti[1,2] · Tommaso Alberti[3] · Alessandro Bemporad[4] · Francesco Berrilli[5] · Roberto Bruno[6] · Vincenzo Capparelli[7] · Vincenzo Carbone[3] · Claudio Cesaroni[8] · Giuseppe Consolini[6] · Alice Cristaldi[9] · Alfredo Del Corpo[1] · Dario Del Moro[5] · Simone Di Matteo[1,2] · Ilaria Ermolli[9] · Silvano Fineschi[4] · Fabio Giannattasio[6] · Fabrizio Giorgi[9] · Luca Giovannelli[5] · Salvatore Luigi Guglielmino[7] · Monica Laurenza[6] · Fabio Lepreti[3] · Maria Federica Marcucci[6] · Matteo Martucci[5,10] · Matteo Mergè[5] · Michael Pezzopane[8] · Ermanno Pietropaolo[1] · Paolo Romano[11] · Roberta Sparvoli[5] · Luca Spogli[8,12] · Marco Stangalini[9] · Antonio Vecchio[13] · Massimo Vellante[1] · Umberto Villante[1,2] · Francesca Zuccarello[7] · Balázs Heilig[14] · Jan Reda[15] · János Lichtenberger[16]

Earth-affecting Solar Transients
Guest Editors: Jie Zhang, Xochitl Blanco-Cano, Nariaki Nitta, and Nandita Srivastava

✉ M. Piersanti
mirko.piersanti@aquila.infn.it

1 Department of Physical and Chemical Sciences, University of L'Aquila, L'Aquila, Italy

2 Consorzio Area di Ricerca in Astrogeofisica, L'Aquila, Italy

3 Department of Physics, University of Calabria, Cosenza, Italy

4 INAF, Osservatorio Astrofisico di Torino, Turin, Italy

5 Physics Department, University of Rome "Torvergata", Rome, Italy

6 INAF, Istituto di Astrofisica e Planetologia Spaziali, Rome, Italy

7 Department of Physics and Astronomy, University of Catania, Catania, Italy

8 Istituto Nazionale di Geofisica e Vulcanologia, Rome, Italy

9 INAF, Osservatorio Astronomico di Roma, Rome, Italy

10 INFN, Laboratori Nazionali di Frascati, Frascati, Italy

11 INAF, Osservatorio Astrofisico di Catania, Catania, Italy

Abstract A full-halo coronal mass ejection (CME) left the Sun on 21 June 2015 from active region (AR) NOAA 12371. It encountered Earth on 22 June 2015 and generated a strong geomagnetic storm whose minimum Dst value was −204 nT. The CME was associated with an M2-class flare observed at 01:42 UT, located near disk center (N12 E16). Using satellite data from solar, heliospheric, and magnetospheric missions and ground-based instruments, we performed a comprehensive Sun-to-Earth analysis. In particular, we analyzed the active region evolution using ground-based and satellite instruments (Big Bear Solar Observatory (BBSO), *Interface Region Imaging Spectrograph* (IRIS), *Hinode, Atmospheric Imaging Assembly* (AIA) onboard the *Solar Dynamics Observatory* (SDO), *Reuven Ramaty High Energy Solar Spectroscopic Imager* (RHESSI), covering Hα, EUV, UV, and X-ray data); the AR magnetograms, using data from SDO/*Helioseismic and Magnetic Imager* (HMI); the high-energy particle data, using the *Payload for Antimatter Matter Exploration and Light-nuclei Astrophysics* (PAMELA) instrument; and the Rome neutron monitor measurements to assess the effects of the interplanetary perturbation on cosmic-ray intensity. We also evaluated the 1 – 8 Å soft X-ray data and the ∼ 1 MHz type III radio burst time-integrated intensity (or fluence) of the flare in order to predict the associated solar energetic particle (SEP) event using the model developed by Laurenza *et al.* (*Space Weather* **7**(4), 2009). In addition, using ground-based observations from lower to higher latitudes (*International Real-time Magnetic Observatory Network* (INTERMAGNET) and *European Quasi-Meridional Magnetometer Array* (EMMA)), we reconstructed the ionospheric current system associated with the geomagnetic sudden impulse (SI). Furthermore, *Super Dual Auroral Radar Network* (SuperDARN) measurements were used to image the global ionospheric polar convection during the SI and during the principal phases of the geomagnetic storm. In addition, to investigate the influence of the disturbed electric field on the low-latitude ionosphere induced by geomagnetic storms, we focused on the morphology of the crests of the equatorial ionospheric anomaly by the simultaneous use of the *Global Navigation Satellite System* (GNSS) receivers, ionosondes, and Langmuir probes onboard the *Swarm* constellation satellites. Moreover, we investigated the dynamics of the plasmasphere during the different phases of the geomagnetic storm by examining the time evolution of the radial profiles of the equatorial plasma mass density derived from field line resonances detected at the EMMA network ($1.5 < L < 6.5$). Finally, we present the general features of the geomagnetic response to the CME by applying innovative data analysis tools that allow us to investigate the time variation of ground-based observations of the Earth's magnetic field during the associated geomagnetic storm.

Keywords Solar trigger · Flare forecasting · Halo CME · SEP forecasting · Cosmic ray · Magnetospheric response to a CME · Ground response to a CME · Ionospheric response to a CME · Ionospheric polar convection

[12] SpacEarth Technology, Rome, Italy

[13] LESIA, Observatoire de Paris, 5 place Jules Janssen, 92190 Meudon, France

[14] Geological and Geophysical Institute of Hungary, Tihany, Hungary

[15] Institute of Geophysics, PAS, Warsaw, Belsk, Poland

[16] Space Research Group, Department of Geophysics and Space Sciences, Eötvös University, Budapest, Hungary

1. Introduction

Coronal mass ejections (CMEs) are large-scale eruptions of plasma and magnetic fields from the Sun (Hundhausen, 1993). When the associated ejecta (interplanetary CME, ICME) hit the Earth's magnetosphere, they can generate temporary disturbances known as geomagnetic storm (GS) (Tsurutani and Lakhina, 2014). The strongest GSs are usually generated by the interaction of the magnetosphere with an incoming ICME plasma and the associated magnetic field. The physical mechanism for the energy transfer is the magnetic reconnection between the possible occurrence of the southward interplanetary magnetic field (IMF) and the northward geomagnetic field (Dungey, 1961). Indeed, it has been fully established that the existence of a strong long-duration southward IMF component ($B_{z,\mathrm{IMF}}$) in some part of the ejecta (loop, magnetic cloud, or filament) or in the shear region ahead of the ejecta (Gonzalez *et al.*, 1994; Gonzalez, Tsurutani, and de Gonzalez, 1999) make these structures highly geoeffective. GSs are characterized by the injection of energetic electrons and ions into the inner magnetosphere (Li *et al.*, 2003). As a consequence, the magnetosphere enters a strongly disturbed state because of the intensification of the ring current (Dessler and Parker, 1959; Sckopke, 1966; Daglis *et al.*, 1997) and the other current systems (*i.e.* Chapman–Ferraro current, tail current and auroral electrojets (Dungey, 1961; Davis and Sugiura, 1966; Gonzalez *et al.*, 1994; Kamide and Kokubun, 1996; Consolini and De Michelis, 2005)), whose effects can be seen both at the ground and near-Earth space (Villante and Piersanti, 2008, 2009). The strength of GSs is typically measured by the Dst index (Gonzalez *et al.*, 1994), which is the hourly average of the deviation of the horizontal component (measured in nT) of the magnetic field measured at several ground stations in mid and low latitudes. The Dst index is considered to reflect the variations in the intensity of the symmetric part of the ring current (Dessler and Parker, 1959; Sckopke, 1966). In recent years, a higher resolution index (SYM-H, 1 min resolution) has been adopted. It has been demonstrated that SYM-H better reflects the effects of the solar wind dynamic pressure variations (Wanliss and Showalter, 2006). The effect of a GS at the ionospheric level presents specific peculiarities depending on the latitudinal and longitudinal sector of the Earth. At ionospheric low latitudes, the so-called equatorial ionospheric anomaly (EIA) occurs because of the interplay between the $\vec{E} \times \vec{B}$ drift ($\vec{E}$ and $\vec{B}$ are the electric and the magnetic fields, respectively), resulting in a daytime uplift of the ionospheric F layer, and because of the pressure gradient and gravity, resulting in a falling back of the plasma (equatorial fountain effect). This interplay leads to the formation of two ionization maxima in the daytime ionosphere, located at about $\pm 15° - \pm 20°$ off the magnetic equator and termed "crests of the EIA" (Rishbeth, 1971). During a GS, the morphology of the northern and southern crests of the EIA can be significantly modified. The modifications can be due to both an intensification and a suppression of the fountain effect, depending on the local time and on the longitudinal sector of the arrival of the disturbance at equatorial latitudes (Aarons, 1991). In the case of intensification, the occurrence of a "super-fountain effect" is sometimes recorded. This effect results in an enhanced uplift of the plasma, leading to the formation of more intense crests that are shifted poleward with respect to the quiet condition (Tsurutani *et al.*, 2004, 2008; Mannucci *et al.*, 2005; Balan *et al.*, 2010; Zong *et al.*, 2010; Venkatesh *et al.*, 2017).

High-energy particles can originate at the Sun in association with solar flares and/or CMEs. They consist mainly of protons and electrons, with a lower percentage of heavier nuclei, with energy ranging from a few tens of keV to several GeV. They are called solar energetic particles (SEPs) or solar cosmic rays. The generation of SEPs is linked to the various highly dynamic processes (on short timescales) in the magnetized coronal and interplanetary plasma. Several mechanisms of particle acceleration during solar flares have

been proposed, such as resonant wave-particle interactions and stochastic acceleration with a complex spectrum of cascading waves (Aschwanden, 2002). These processes occur in conjunction with magnetic reconnection in the flare development. In addition, interplanetary shocks are known to be largely responsible for the acceleration of energetic particles (Pesses *et al.*, 1979; Kennel *et al.*, 1984a,b; Tsurutani *et al.*, 1982, 2009; Tsurutani and Lin, 1985; Reames, 1999). Several processes (*e.g.* first-order Fermi acceleration, shock drift acceleration) are mainly invoked to explain SEP acceleration by strong CME-driven shocks (Giacalone and Kóta, 2006; Reames, 1999) as well. In particular, flares and CME-driven shocks are believed to be responsible for particle acceleration in impulsive and gradual events, respectively, although this classic paradigm has been challenged by the observations of hybrid events (Kocharov and Torsti, 2002). At present, the principal acceleration mechanisms for solar energetic particles are still under debate.

SEPs propagate in the interplanetary space along the lines of force of the interplanetary magnetic field and are detectable as sudden increases in the particle fluxes measured by instruments onboard satellites and space probes. Moreover, relativistic SEPs in the Earth's atmosphere can produce showers of secondary particles with sufficient energy to be detected by ground-level neutron monitors and with intensities that exceed the Galactic cosmic-ray (GCR) background, *i.e.* the so-called ground-level enhancements (GLEs).

The observed SEP event time profiles have to be understood as a superposition of particles accelerated during the solar eruptive event as well as particles continuously accelerated at the CME-driven shock front, when present, with their characteristics modified by their subsequent propagation. Hence, an SEP event is the result of the interplay of many factors, such as the existing conditions for solar eruptive event and/or shock-particle acceleration, the local geometry and strength of the traveling shock, the relative position in space of the observer with respect to the position of the parent solar source, and the transport conditions in interplanetary space.

SEPs constitute a hazardous condition in interplanetary and near-Earth space as they can damage electronic components on satellites, lead to spacecraft malfunction (Iucci *et al.*, 2005), and pose a radiation threat for astronauts (Hoff, Townsend, and Zapp, 2004) and crews of high-flying aircraft and commercial airlines in polar routes (Getley *et al.*, 2005). They can influence the polar ionosphere, causing absorption of high-frequency radio waves, thereby affecting long-distance radio communication and radar systems (Hunsucker, 1992), and can even contribute to the creation of a new radiation belt (Blake *et al.*, 1992; Li *et al.*, 1993; Tsurutani and Lakhina, 2014; Lorentzen *et al.*, 2002; Valtonen, 2005). Hence, SEP warning systems (*e.g.* the Empirical Model for Solar Proton Events Real Time Alert (ESPERTA), Laurenza *et al.* (2009) and Alberti *et al.* (2017a)) have been developed in order to predict SEP event occurrence and mitigate their impacts.

As the Saint Patrick Day storm on 17 March 2015, the event on 22 June 2015 was one of the largest geomagnetic storms of the past decade. The southern hemisphere of the Sun was quite active in June 2015, showing both extensive transequatorial coronal hole structures and large magnetic active regions (ARs) (Baker *et al.*, 2016a). Between 21 and 22 June 2015, three CMEs struck the Earth. The first and the second caused two sudden impulses (SI), while the third caused a large geomagnetic storm on 22 June (Baker *et al.*, 2016a,b; Reiff *et al.*, 2016). Liu *et al.* (2015) examined the sources of the 22 June geomagnetic storm, analyzing how the plasma and magnetic field characteristics of the ICME control the geomagnetic storm intensity and variability. By reconstructing the cross sections of two magnetic clouds and/or flux ropes identified inside the ICME, they found that the 22 June event is a single ejecta instead of multiple ICMEs like the Saint Patrick Day storm. Reiff *et al.* (2016) made an *in situ* analysis of the 22 June 2015 GS using observations from the *Magnetospheric Multiscale Mission* (MMS), the *Van Allen Probes* (VAP), the *Active Magnetosphere*

and Planetary Electrodynamics Response Experiment (AMPERE), and the *Defense Meteorological Satellite Program* (DMSP). As shown by the magnetic fields observed at MMS in the tail and by VAP closer to Earth, a dramatic dipolarization at the magnetotail occurs in response to the northward turnings of the IMF. Moreover, Liu and coauthors interpreted the transitions of MMS from the plasma sheet to the lobe in terms of a concurring contribution of the thinning and expansion of the plasma sheet, and of an up- and down-flapping of the magnetotail current-sheet. Furthermore, the DMSP plasma flow data showed both a single-cell convection pattern in the northern hemisphere and a drop in the cross-polar cap potential. Astafyeva, Zakharenkova, and Patrick (2016) studied the ionospheric response using three SWARM (*i.e.* geomagnetic low Earth orbiting constellation) satellite data. They showed that on the dayside, the prompt penetration electric fields (PPEF) were the main drivers for the observed extreme ionospheric response, while on the nightside, the topside ionosphere responded to the combination of the PPEF and the storm-time thermospheric circulation. They concluded that the disturbance dynamo might have reinforced the effect of the PPEF.

Using data from solar, heliospheric, magnetospheric missions and ground-based instruments, in this article we perform a cross-platform analysis of the geoeffective solar event of 21 June 2015. In particular, we analyze the active region evolution using ground-based and satellite instruments (Big Bear Solar Observatory (BBSO), *Interface Region Imaging Spectrograph* (IRIS), *Hinode, Atmospheric Imaging Assembly* (AIA) onboard the *Solar Dynamics Observatory* (SDO), *Reuven Ramaty High Energy Solar Spectroscopic Imager* (RHESSI), covering Hα, EUV, UV, and X-ray data), the AR magnetograms (SDO/*Helioseismic and Magnetic Imager* (HMI)), the early evolution in the lower corona of the solar eruption (white-light data from the *Large Angle and Spectrometric Coronagraph* (LASCO) onboard the *Solar and Heliospheric Observatory* (SOHO)), the high-energy particle data (*Payload for Antimatter Matter Exploration and Light-nuclei Astrophysics* (PAMELA), *Geostationary Operational Environmental Satellite* (GOES), and the Rome neutron monitor), and the effects of interplanetary perturbation on cosmic-ray intensity. For this specific eruption, no data were available from the *Solar Terrestrial Relations Observatory* (STEREO) mission because the contact with the STEREO-B spacecraft was lost 1 October 2014, while the *In-situ Measurements of Particles and CME Transients* (IMPACT), the *Plasma and Suprathermal Ion Composition* (PLASTIC), and the *Sun Earth Connection Coronal and Heliospheric Investigation* (SECCHI) instruments on STEREO-A were turned off for superior solar conjunction from March 2015 until July 2015. We also apply the ESPERTA model, developed by Laurenza *et al.* (2009) and validated by Alberti *et al.* (2017a), in order to predict the associated SEP event. Furthermore, to investigate the influence of the disturbed electric field on the low-latitude ionosphere induced by geomagnetic storms (Muella *et al.*, 2010; Alfonsi *et al.*, 2013; Tulasi Ram *et al.*, 2016; Spogli *et al.*, 2016), we focus on the morphology of the crests of the EIA. To do this, we concentrate on the ionospheric characterization provided by the simultaneous use of the *Global Navigation Satellite System* (GNSS) receivers, ionosondes, and Langmuir probes onboard the Swarm constellation. In addition, we analyze the response of the different magnetospheric current systems to the ICME arrival by a comparison between the TS04 model (Tsyganenko and Sitnov, 2005) predictions, magnetospheric observations, and geomagnetic measurements during the SI. In particular, using ground-based observations from low to high latitudes, we reconstruct the ionospheric current system associated with the SI. We also investigate the dynamics of the plasmasphere during the different phases of the geomagnetic storm by examining the time evolution of the radial profiles of the equatorial plasma mass density as inferred from field line resonances detected by the *European Quasi-Meridional Magnetometer Array* (EMMA) network ($1.5 < L < 6.5$). We present the general features of the

geomagnetic response to the ICME by applying innovative data analysis tools that allow us to investigate the time variation of ground-based observations of the Earth's magnetic field during the associated geomagnetic storm. A description of the polar ionospheric convection is also presented. Finally, using *Superdual Auroral Radar Network* (SuperDARN) measurements, we analyze the polar ionospheric convection during the SI, the main phase, and the recovery phase of the GS.

2. Solar Data

The CME that encountered the Earth and generated the geomagnetic storm on 22 June 2015 originated in AR NOAA 12371. This appeared on the eastern limb of the solar disk on 16 June 2015. At that time, its magnetic configuration was classified as β, evolving into $\beta\gamma\delta$ in the following days. On 21 June, two subsequent flares were observed in the AR, and their X-ray flux was measured by the GOES 15 satellite: `SOL2015-06-21T01:02` and `SOL2015-06-21T02:06`, classified as M2.0 and M2.6, respectively. At 02:36 UT, the LASCO coronagraphs onboard the SOHO satellite first observed the halo CME expanding into the heliosphere.

A number of solar facilities observed AR NOAA 12371 during its passage across the solar disk, and during time intervals close to the CME as well.

The *Helioseismic and Magnetic Imager* (HMI, Scherrer *et al.*, 2012) onboard SDO (Pesnell, Thompson, and Chamberlin, 2012) took full-disk spectropolarimetric measurements in the Fe I line at 617.3 nm with a resolution of $1''$. The SDO/HMI data used in this article cover 11 days of observations, starting from 15 June until 26 June, with a cadence of 12 min.

In this analysis, we used SDO/HMI cylindrical equal area (CEA) Space-weather Active Region Patches (SHARPs) data (Hoeksema *et al.*, 2014). The CEA SHARP data provide maps of the photospheric magnetic field of the AR projected and remapped to a cylindrical equal-area Cartesian coordinate system centered on the tracked AR. Continuum intensity, Doppler velocity, and line-of-sight (LOS) magnetic field are also provided for this region. We refer to Bobra *et al.* (2014) for a comprehensive explanation of the SHARP pipeline. We selected a field of view (FOV) of these CEA SHARP data of about $476'' \times 228''$ that encompasses the AR. The Doppler velocity has been corrected for the effect of solar rotation, which is not removed in these SDO/HMI measurements (see, *e.g.* Welsch, Fisher, and Sun, 2013), by subtracting the mean velocity averaged over ten days, which is available in the SDO/HMI data series relevant to Carrington rotation 2165. Finally, these Doppler velocities were calibrated assuming umbral regions (*i.e.* with normalized continuum intensity < 0.4) at rest. This is a reasonable assumption that is usually adopted in high-resolution observations, provided that convection is inhibited in umbral regions.

Furthermore, filtergrams acquired by the *Atmospheric Imaging Assembly* (AIA, Lemen *et al.*, 2011) onboard the SDO mission were used to study the evolution of the flare in the coronal and upper chromospheric layers in detail. We extracted a series of cutout images with an FOV that covers $515'' \times 388''$; this also covers the FOV used for the CEA SHARP data. SDO/AIA cutouts comprise the time interval between 00:00 UT and 02:30 UT on 21 June with the highest available cadence (12 s for the EUV passbands, 24 s for the UV 1600 and 1700 Å images).

The spectropolarimeter (SP) of the *Solar Optical Telescope* (SOT: Tsuneta *et al.*, 2008; Lites *et al.*, 2013) onboard the *Hinode* satellite (Kosugi *et al.*, 2007) acquired various raster scans over AR NOAA 12371, recording the Stokes profiles along the Fe I line pair at 630.15 nm and 630.25 nm. In particular, four scans were acquired with a pixel sampling of $0''.32$

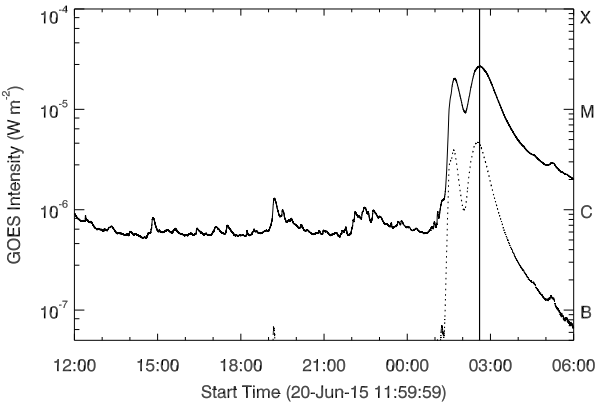

Figure 1 GOES X-ray flux curves in the 1 – 8 Å channel (*solid line*) and in the 0.5 – 4 Å channel (*dotted line*). The *vertical line* indicates the time of first detection of the halo CME.

Table 1 Characteristics of the two flares observed by the GOES 15 satellite in AR NOAA 12371 before the CME.

Flare	Class	Time (UT)		
		Begin	Peak	End
SOL2015-06-21T01:02	M2.0	01:02	01:42	02:00
SOL2015-06-21T02:06	M2.6	02:06	02:36	03:02

and a polarimetric signal-to-noise ratio of about 10^3 (fast mode), starting at 14:47 UT and 19:41 UT on 20 June and at 00:37 UT and 06:11 UT on 21 June. The first three scans covered a region of about $274'' \times 162''$, while the last scan covered only the central region of the AR with an FOV of $110'' \times 162''$.

The reconstructed SOT/SP continuum maps were aligned with the SDO/HMI continuum images closest in time using the IDL SolarSoft mapping routines (Freeland and Handy, 1998). Level 2 data derived using the Milne–Eddington Grid Linear Inversion Network (MERLIN) code (Lites *et al.*, 2007) were used in our analysis. We performed azimuth disambiguation of the Level 2 data using the non-potential magnetic field calculation technique (NPFC, Georgoulis, 2005), obtaining inclination and azimuth angles in the local solar frame.

2.1. Solar Trigger

In Figure 1 we plot the X-ray emission flux as measured by the GOES 15 satellite from 12:00 UT on 20 June until 06:00 UT on 21 June. Two M-class flares were observed before the appearance of the halo CME. Their characteristics are listed in Table 1. The first detection of the CME occurs near the peak of the second flare. These energetic events occurred after a rather long interval of low activity in the AR, as the previous flare (M1.0) occurred at 06:28 UT on 20 June. Note that the C-class flare at around 19:00 UT on 20 June occurred in a different AR (NOAA 12367).

First, we analyzed the large-scale structuring of AR 12371 and its eruptive potential by estimating the fractal and multifractal properties of its photospheric configuration. Indeed, several studies in the literature indicate that measurements of these properties may help assessing, and even predicting, the flare activity of magnetic regions (for a list of studies carried out during the past decade, see *e.g.* Ermolli *et al.*, 2014). Thus, we first explored the sensitivity of measurements of fractal and multifractal parameters on the eruptive activity observed for AR 12371.

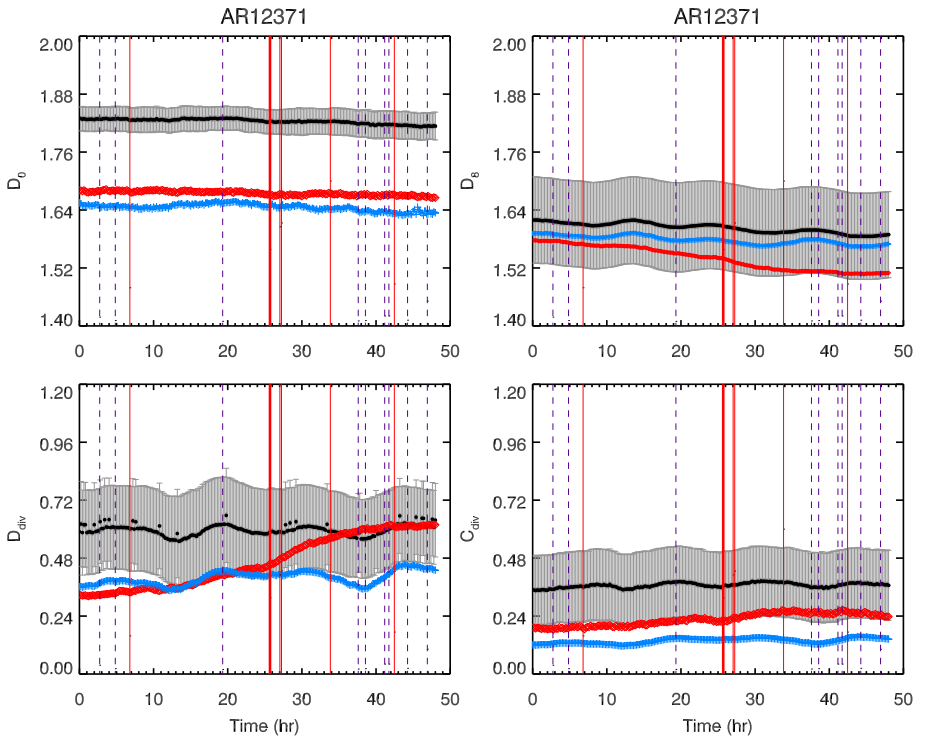

Figure 2 Time series of the fractal and multifractal parameters measured on AR 12371 by considering both unsigned (*black circles*) and signed flux data (positive and negative, *red diamonds* and *blue crosses*, respectively). *Top*: fractal parameters D_0 (*left*) and D_8 (*right*). *Bottom*: $C_{\rm div}$ (*left*) and $D_{\rm div}$ (*right*). Time 0 corresponds to 00:00 UT on 20 June 2015. *Vertical thin-solid* (*thin-dashed*) *lines* indicate the time of occurrence of M-class (C-class) flares hosted by the AR. Flares associated with the CME occurred on 21 June 2015 are indicated by the *thick-solid line*. *Error bars* show the uncertainty associated with the measured values; details are given in the text. For clarity, the error bars are only shown for the results from unsigned flux data.

To this purpose, we analyzed the time series of SDO/HMI CEA SHARP line-of-sight (LOS) magnetic field data described above. Following the data and methods applied in Giorgi *et al.* (2015) and Ermolli *et al.* (2014), we computed the fractal D_0 and D_8 and the multifractal contribution diversity, $C_{\rm div}$, and dimensional diversity, $D_{\rm div}$, parameters on the subfield of about 256 arcsec × 256 arcsec centered on the AR.

Figure 2 shows the temporal evolution of the fractal D_0 and D_8 (top panels) and of the multifractal contribution diversity, $C_{\rm div}$, and dimensional diversity, $D_{\rm div}$ (bottom panels), parameters estimated for the studied region. In this figure, red (blue) symbols show the results of measurements carried out by considering the positive (negative) flux in the AR, while black symbols display the results of measurements from the unsigned magnetic flux data. Positive (negative) flux corresponds to trailing (leading) regions in the AR. Time 0 corresponds to 00:00 UT on 20 June 2015. Error bars indicate the standard deviation of the measured values as in Ermolli *et al.* (2014). For the sake of clarity, the deviation is only shown for the values derived from unsigned flux data. We also show the flaring activity of AR 12371 over the analyzed period. In each plot, the vertical thin-solid (thin-dashed) lines indicate the time of occurrence of M-class (B- and C-class) flares. Flares associated with the CME that occurred on 21 June 2015 are indicated by the thick-solid line.

The studied region exhibits significant fractality because the D_0 (D_8) values measured for its photospheric configuration range between ≈ 1.64 and ≈ 1.84 (≈ 1.52 and ≈ 1.72). With respect to the average and standard deviation of the parameters reported by Giorgi *et al.* (2015) for ARs hosting different flare classes, the values measured for the AR 12371 would have allowed targeting it as a likely M- and X-class flaring region ahead of the eruptive events observed on 21 June 2015. However, the trends in Figure 2 seem to lack any further signature of the eruptive events hosted by the region. In agreement with results reported in the literature, the fractal and multifractal parameters estimated for the region have opposite temporal evolution. Indeed, the time series of the fractal (multifractal) parameters measured on the AR 12371 look rather similar and flat over time, but for the results of the D_0 and D_8 ($C_{\rm div}$ and $D_{\rm div}$) measurements derived from the positive flux data that show a net decrease (increase) during the analyzed period. The trends of the values estimated for the same quantities from unsigned and negative flux data are rather unvaried over time. We conclude that while the above measurements point out the eruptive potential of AR 12371 ahead of the events occurred on 21 June 2015, they also suggest the lack of clear effects of these events on the photospheric configuration of the magnetic field of AR 12371.

Figure 3 (top panel) shows the photospheric configuration of AR NOAA 12371 a few minutes before the start of `SOL2015-06-21T01:02`. The AR exhibited a central part with opposite polarities in contact, sharing some penumbral filaments (δ configuration, see Figure 3, middle panel). At chromospheric heights, a sigmoidal-like structure is visible along the polarity-inversion line (PIL) present in the region (bottom panel).

Along the PIL, peculiar upflows and downflows of about ∓ 1.5 km s^{-1}, which are not related to the classical Evershed flow observed in sunspots, were found. These flows are reminiscent of the velocity field configuration found in δ complexes by Shimizu, Lites, and Bamba (2014) and Cristaldi *et al.* (2014) that has been attributed to shear accumulation (see Figure 4).

Taking advantage of the resolving power of the *New Solar Telescope* at Big Bear Solar Observatory (BBSO, see also Jing *et al.*, 2016), we can image the fine details of the photospheric configuration of AR12371. In Figure 5 (*left*) we show a continuum HMI image displaying the photospheric configuration of AR NOAA 12371 marked with a red box indicating the IRIS FOV, while the blue box indicates the BBSO FOV centered on the δ complex. Figure 5 (*right*) shows an image acquired by BBSO in the TiO band, centered on 705.7 nm, which shows the details of the δ complex. The eastern umbra is characterized by light bridges, and the penumbral filaments located between the two opposite-polarity umbrae are highly sheared.

The M2.0 flare is located along the PIL, as shown in Figure 6. Figure 7 displays the morphology of the coronal regions of AR NOAA 12371 close to the flare peak, as visible in SDO/AIA images. The online movies in the various passbands show that the evolution between the two M2.0 and M2.6 flares occurs without interruption. During the event, several coronal structures are destabilized in a succession that is reminiscent of a domino-like effect (*e.g.* Zuccarello *et al.*, 2009), triggered by an activation process occurring in the δ complex. In this sense, `SOL2015-06-21T01:02` and `SOL2015-06-21T02:06` can be considered as a unique event.

In particular, Figures 8 and 9 show the evolution of the event at two different atmospheric heights, as seen in AIA 211 Å and 304 Å images, respectively. The event, triggered in the region hosting the δ sunspot, also involves locations quite far from this sunspot (see, *e.g.*, at coordinates $[-200:-100]$ and $[-50:50]$, horizontal and vertical, respectively), where the signatures of a filament activation and eruption are visible. As these images show, the size of the region that was involved is quite large, implying a considerable amount of mass that could be ejected and be later observed as a CME.

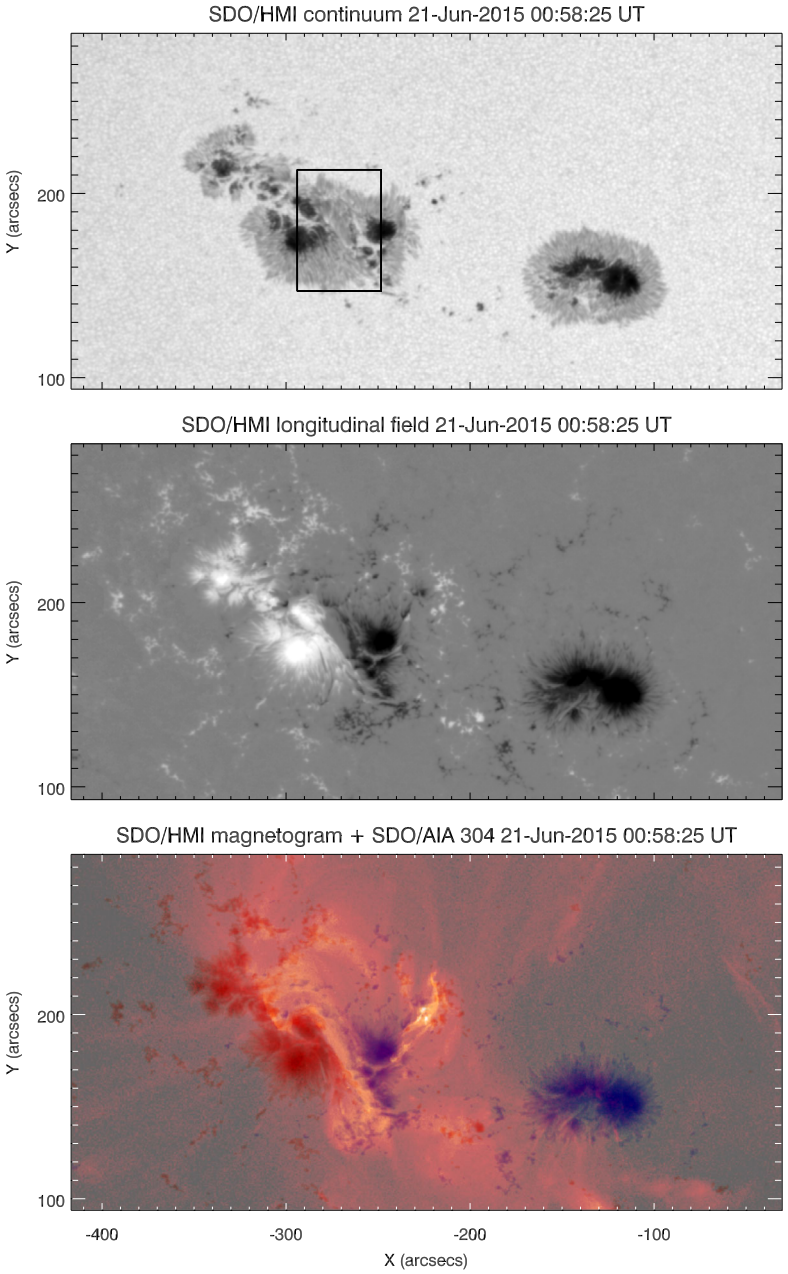

Figure 3 *Top*: Map of the photospheric continuum of AR NOAA 12371, acquired by SDO/HMI some minutes before `SOL2015-06-21T01:02`. The region indicated with a *solid line* shows the FOV used for the analysis of SOT/SP data. *Middle*: Simultaneous SDO/HMI magnetogram. The values of the longitudinal field are saturated at $\pm$2000 G (*white/black* correspond to positive/negative field values). *Bottom*: Simultaneous SDO/HMI magnetogram. *Red* (*blue*) *areas* indicate positive (negative) polarity. SDO/AIA emission at 304 Å passband is superimposed on the magnetogram.

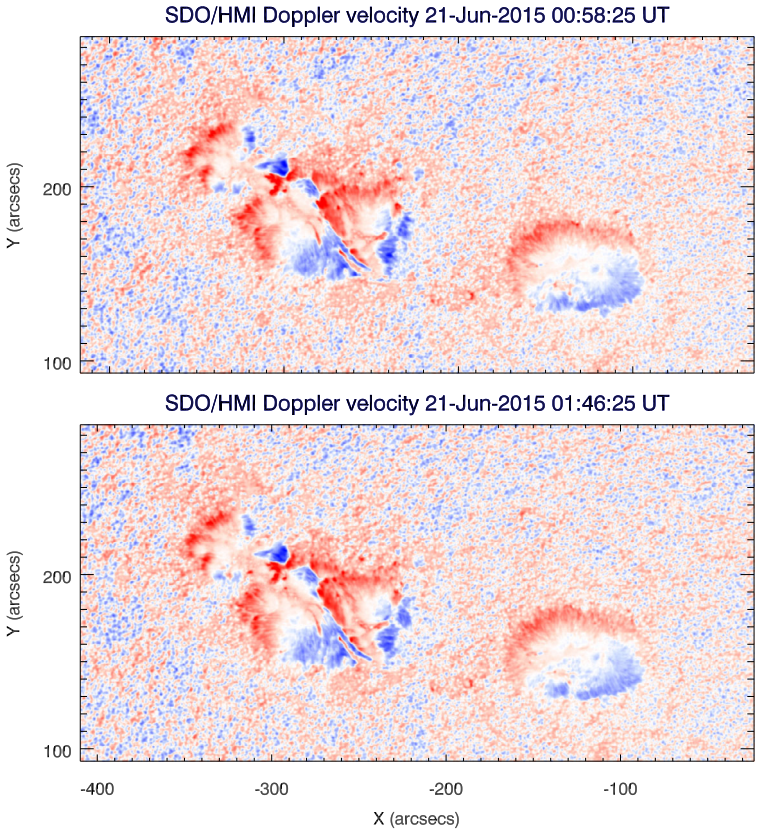

Figure 4 *Top*: Map of the Doppler velocity of AR NOAA 12371 acquired by SDO/HMI some minutes before `SOL2015-06-21T01:02`. *Bottom*: Same at the time of the flare peak. The values of the Doppler velocities are saturated at $\mp 1.5\ \mathrm{km\,s^{-1}}$ (*blue/red* correspond to positive/negative values).

To investigate the configuration of the coronal magnetic field of AR NOAA 12371 at coronal levels, we used a linear force-free extrapolation code based on a method introduced by Alissandrakis (1981). The model assumes that the magnetic field is force-free both in the corona and at lower levels, and that it vanishes at infinity. We used as input parameters the values of the longitudinal magnetic field component at the boundary (*i.e.* the photosphere), provided by SDO/HMI at 00:58:25 UT. We used a force-free parameter equal to $-0.01\ \mathrm{pixel}^{-1}$ to reconstruct the coronal magnetic field configuration and to provide a good fit with the coronal loops observed by SDO/AIA. The result is shown in Figure 10, where we distinguish the main flux tubes involved in the event. The blue field lines seem to reproduce the brightest loops in Figure 6 quite well. We also highlight the overlying arcade that was involved in this solar eruption.

In order to provide a global view of the magnetic field configuration of the whole Sun, we also outline the magnetic configuration of the corona by extrapolating the coronal magnetic field lines according to the model developed by Schrijver and DeRosa (2003); this is included in the SolarSoft package and is called the potential field source surface (PFSS) model. The coronal magnetic field is extrapolated from the photospheric field via the PFSS approximation, in which the field is assumed potential in the coronal volume between the

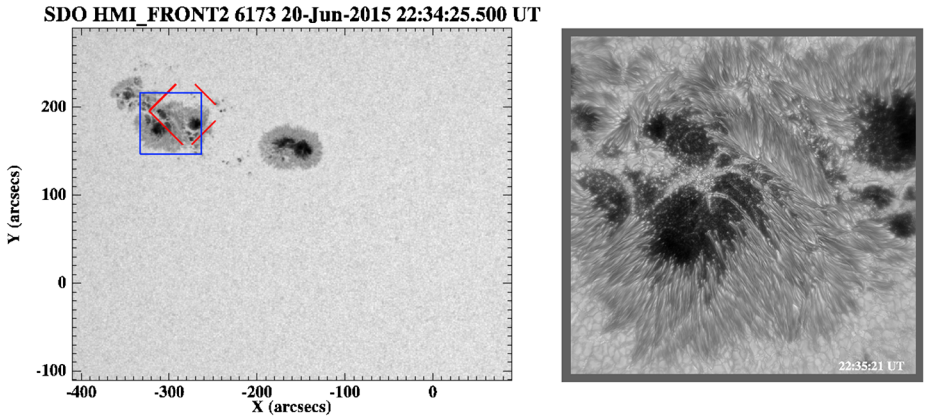

Figure 5 *Left*: Continuum SDO/HMI image showing the photospheric configuration of AR NOAA 12371. The *red box* indicates the FOV observed by IRIS. *Right*: BBSO image acquired in the TiO band.

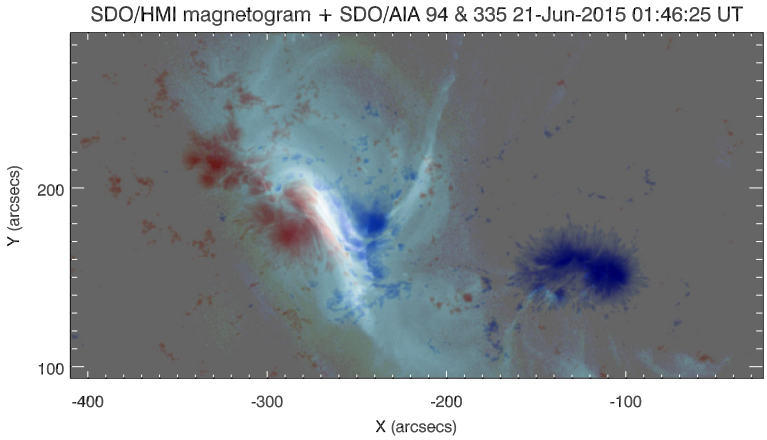

Figure 6 SDO/HMI magnetogram at the peak of `SOL2015-06-21T01:02`. *Red* (*blue*) *areas* indicate positive (negative) polarities. A composite image of SDO/AIA emission at the 94 Å and 335 Å passbands is superimposed on the magnetogram map.

photosphere and a spherical source surface at 2.5 solar radii. Since the coronal field models are provided at a 6 hr cadence by the online database using the PFSS approach, Figure 11 shows the magnetic configuration closest in time to the beginning of the flare, *i.e.* 21 June 2015 at 00:04 UT. The extrapolations have been generated considering the point of view of an observer along the LOS from Earth. We note several open magnetic field lines around NOAA 12371 that are directed toward Earth (indicated in green in Figure 11).

The sub-FOV $110'' \times 162''$ indicated with a solid line in Figure 3, which corresponds to the PIL region, was observed during all four raster scans made with the SP of the SOT. Figure 12 (left panel) shows the vertical component of the solar magnetic field (Bs_z) in this region. The red line indicates the strong PIL, *i.e.* the region where Bs_z changes sign and Bs_t (the transverse component) is stronger than 500 G.

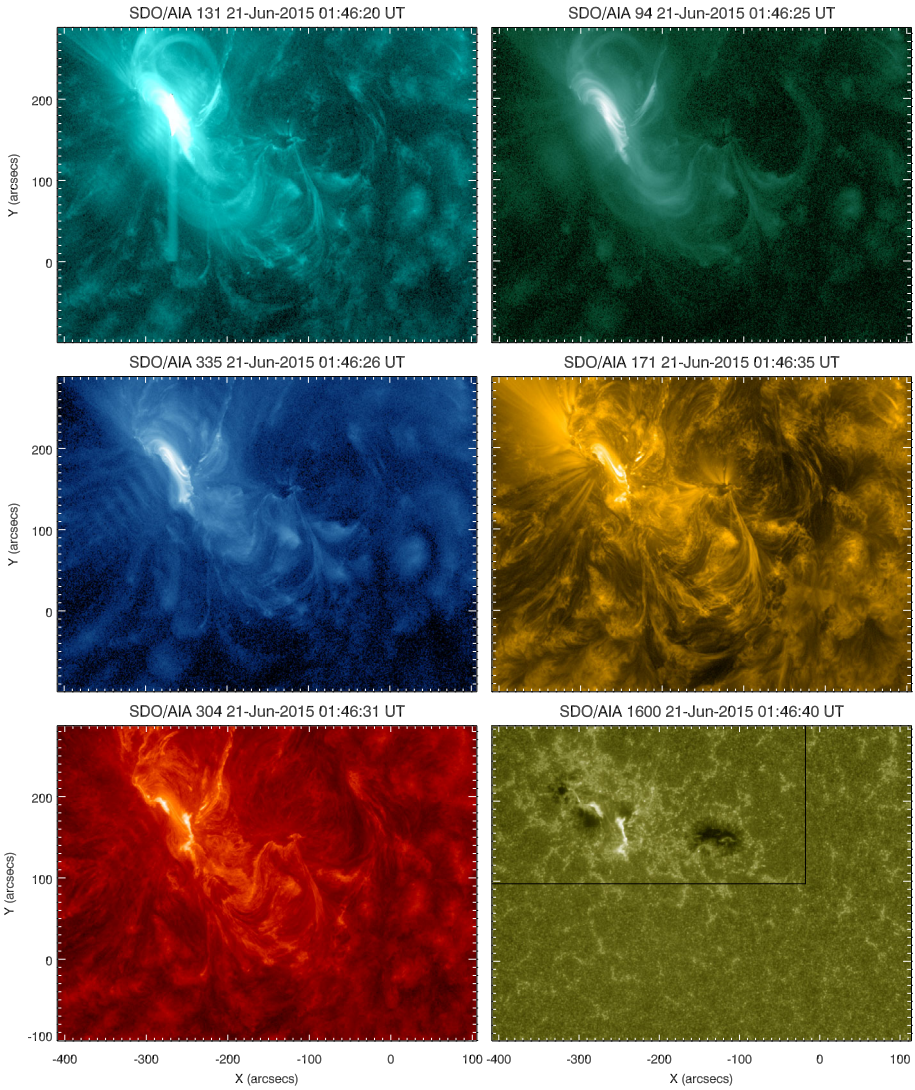

Figure 7 Morphology of AR NOAA 12371 at the peak of `SOL2015-06-21T01:02`. The *rectangle* in the 1600 Å map indicates the FOV shown in Figure 6 as a reference. An animation of this figure is available as electronic supplementary material.

We estimated the shear between the observed (measured) horizontal field and the horizontal field derived through a potential field extrapolation (Wang *et al.*, 1994) according to Falconer, Moore, and Gary (2002) and Jiang *et al.* (2016). The potential field was computed using the method described by Alissandrakis (1981). As a proxy of this shear, we used the horizontal shear angle, θ, as defined in Romano *et al.* (2014) and Gosain and Venkatakrishnan (2010).

We computed the dip angle, which measures the difference between the inclination angle of the observed field and that of the potential field (see, *e.g.*, Gosain and Venkatakrishnan,

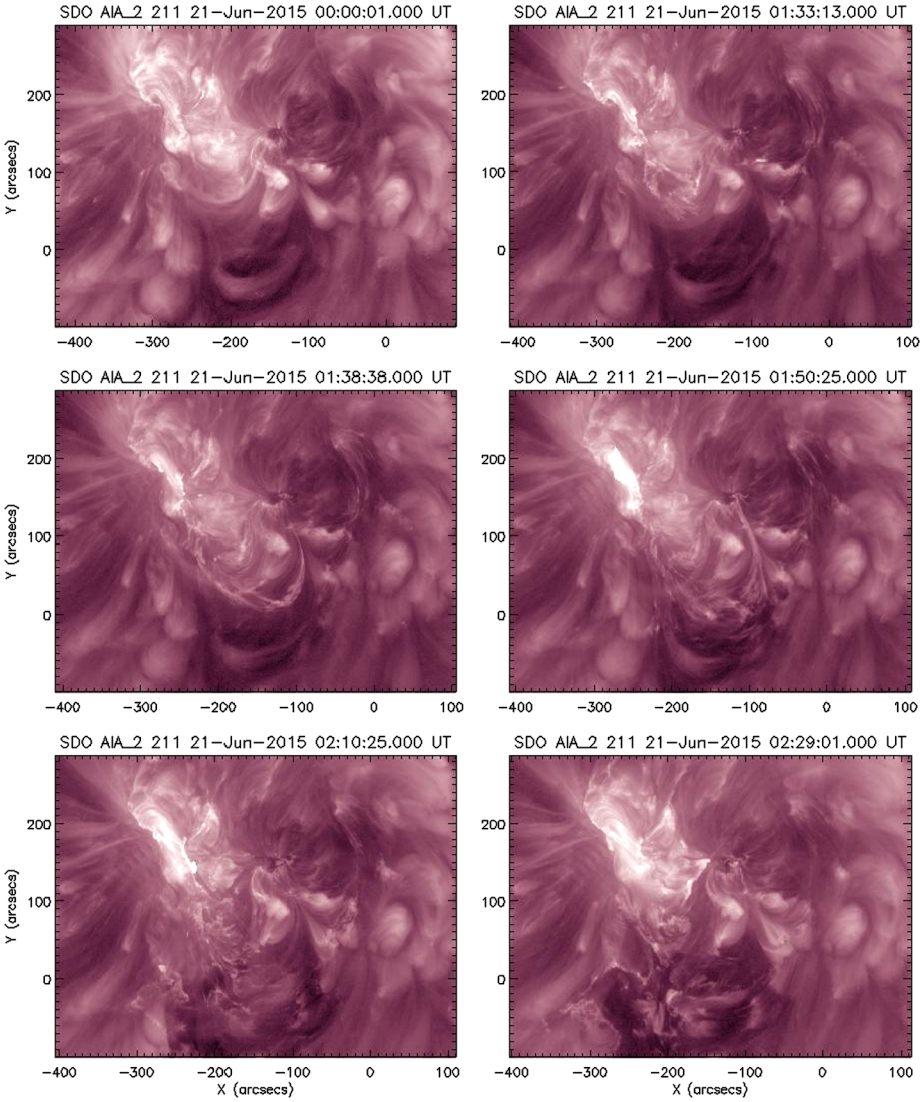

Figure 8 Sequence of AIA 211 Å images showing the evolution of the flare that occurred in AR NOAA 12371. The two ribbons of the flare are clearly visible at [−300 : −180] and at [80 : 300] (horizontal and vertical coordinates, respectively) in all the images. The destabilization and later eruption of a filament can be observed starting at 01:38 UT at coordinates [−200 : −100] and [−50 : 50] (horizontal and vertical coordinates, respectively). An animation of this figure is available as electronic supplementary material.

2010; Petrie, 2012; Romano *et al.*, 2014). This quantity is defined as

$$\Delta\gamma = \gamma^{\mathrm{obs}} - \gamma^{\mathrm{pot}}, \tag{1}$$

where is the inclination angle derived in both cases is equal to $90^\circ - \arctan\left(Bs_z/Bs_t\right)$.

The resulting maps of the shear angle are shown in Figure 12, just a few minutes before the M2.0 flare (bottom left panel) and after some hours (bottom right panel). The region be-

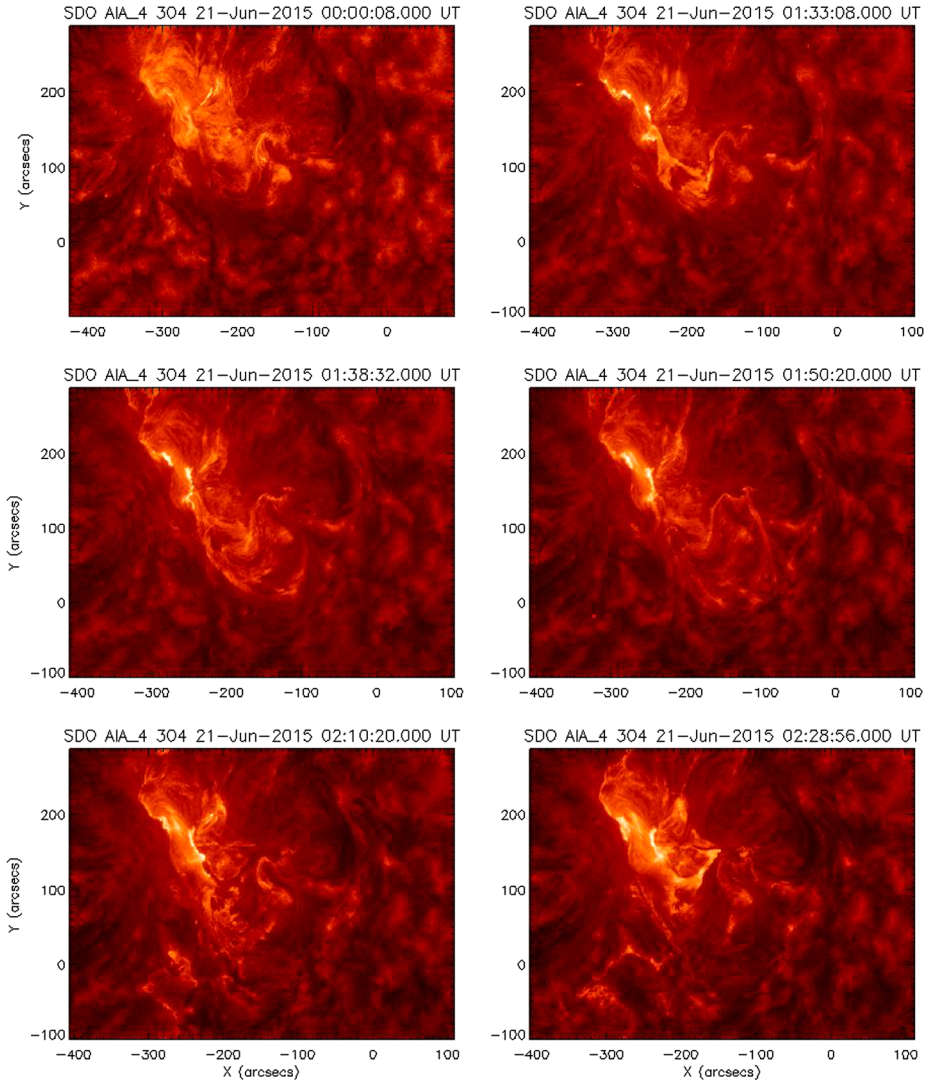

Figure 9 Same as in Figure 8, but for a lower atmospheric level, as observed by AIA at 304 Å. An animation of this figure is available as electronic supplementary material.

tween the opposite polarities of the δ complex underlying the filament seen in the SDO/AIA 304 passband is characterized by high values of the shear angle, larger than 45°. Note that small patches in the FOV far from the PIL, showing a large shear angle, near regions with Bs_t lower than 200 G (white background) may be affected by errors in the 180° azimuth ambiguity resolution. The shear angle exhibits a slight decrease after the flare.

We also used the results obtained with the NPFC code to estimate the electric current in the vertical direction, $|j_z|$, and the gradient of the vertical component of the magnetic field, $|\nabla Bs_z|$, following Georgoulis and LaBonte (2004).

In Table 2 we report the mean (unsigned) values of the shear angle, dip angle, $|j_z|$, and $|\nabla Bs_z|$ calculated along the PIL. The shear angle increases until the flares occur, and de-

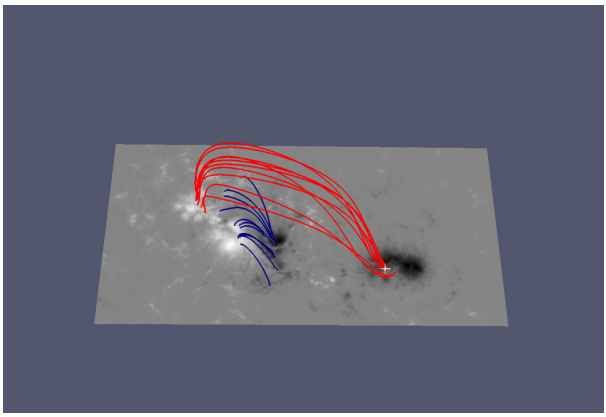

Figure 10 Linear force free extrapolation of the photospheric magnetic field of the AR NOAA 12371.

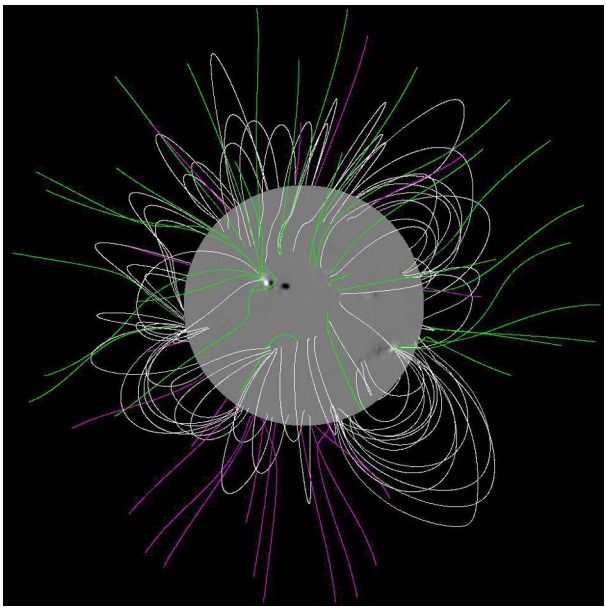

Figure 11 PFSS extrapolation of the full-disk magnetic field on 21 June at 00:04 UT. We show the longitudinal component of the photospheric magnetic field on the solar surface obtained by SDO/HMI.

creases at the end. The dip angle exhibits a similar behavior. In addition, the $|j_z|$ values grow until the eruptive event occurs and diminish after the flares, while $|\nabla Bs_z|$ begins to decrease before the events. This trend indicates that a dynamical process of energy storage is taking place in the hours before the eruptive phenomena, through shear accumulation. Then, after the energy release events, a relaxed state is reached.

3. Flare Forecasting Parameters from SDO/HMI Magnetograms

A variety of magnetic field proxies is used to characterize ARs and to try to forecast the flaring event occurrence, see *e.g.* Falconer, Moore, and Gary (2002), Leka and Barnes (2003, 2007), and Schrijver (2009). In this section we concentrate on four variables that have been

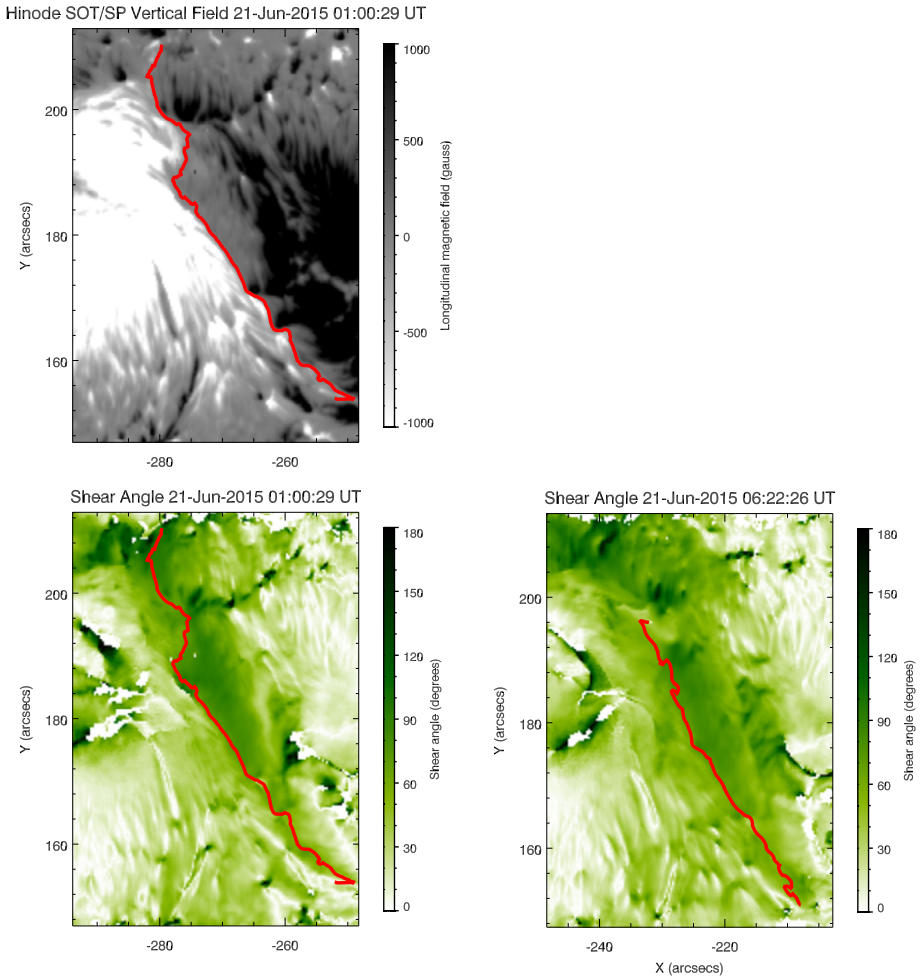

Figure 12 *Left top*: Map of the vertical component Bs_z some minutes before the start of the flaring activity in AR NOAA 12371. *Bottom left*: Simultaneous map of the shear angle. *Bottom right*: Map of the shear angle three hours after the flares. The *solid red line* indicates the PIL.

Table 2 Evolution of the mean value of the shear angle θ, dip angle $\Delta\gamma$, current $|j_z|$, and gradient $|\nabla Bs_z|$ along the PIL of AR NOAA 12371.

Time (UT)	$\langle\theta\rangle$ (degrees)	$\langle\Delta\gamma\rangle$ (degrees)	$\langle\lvert j_z\rvert\rangle$ (mA/m^2)	$\langle\lvert\nabla Bs_z\rvert\rangle$ (G/m)
2015-06-20 15:10:48	42.7	0.94	16.0	14.4
2015-06-20 20:03:52	43.9	−2.19	17.9	25.2
2015-06-21 01:00:29	67.6	−1.23	18.2	12.4
2015-06-21 06:22:26	64.1	−0.93	13.4	9.8

proved to provide a statistical forecast estimation of flares: log(R), the total unsigned vertical current (TOTUSJZ), the total unsigned current helicity (TOTUSJH), and the total photospheric magnetic free energy density (TOTPOT).

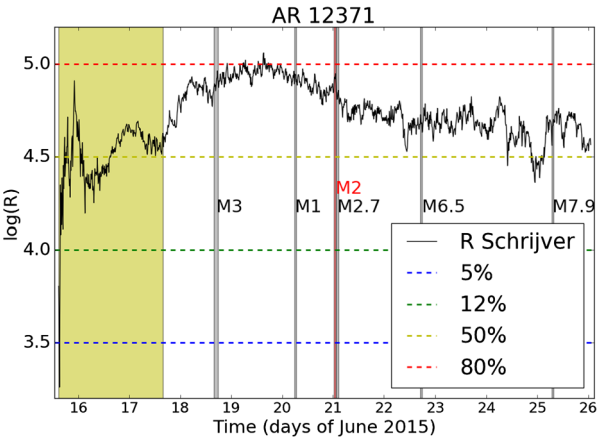

Figure 13 log(R) parameter as a function of time. We report the probability of a flare > M1 occurring in the next 24 hours based on Schrijver (2007). *Shaded yellow area*: Solar longitude > 60°. *Shaded gray* and *red*: Flares > M1 produced by AR12371.

The log(R) parameter is a measure of the unsigned flux near the magnetic polarity separation lines. The log(R) is a proxy of the photospheric electrical currents introduced in Schrijver (2007) and is a measure of the maximum energy available in the AR. Using a vast dataset from the *Michelson Doppler Imager* (MDI), we established the probability of flare occurrence given a certain log(R) value. We chose these parameters as they have high scores in a machine-learning-based algorithm that uses vast statistics of HMI data to derive flaring ARs (Bobra and Couvidat, 2015).

We retrieved the time series of the four magnetic parameters from the HMI data repository, located at the Joint Science Operations Center (JSOC). In particular, we used the SHARP data (Bobra *et al.*, 2014), which calculate the selected parameters with a 12 min cadence for the whole AR region.

The time evolution of the four parameters for NOAA AR 12371, spanning from 15 June (AR emerging from east limb) to 26 June, are shown in Figures 13 to 15. We mark in yellow the portion of the dataset with a solar longitude > 60°, which should be disregarded because of projection effects. We report as shaded gray areas the time spanned by the flares produced by AR 12371 alone and in red the M2 flare that produced the full-halo CME we are investigating. The intensity of the flare is marked on the plot at the flare peak intensity position.

We note from Figure 13 that the log(R) value, and therefore the probability of having an M flare, is high for the whole period. We remark here that while the log(R) values are based on HMI magnetograms, the occurrence rates of M- or X-class flares for a given log(R) value have been computed on MDI data and are therefore only indicative. The flare prediction is in good agreement with the observed sequence of six M-class flares, spanning up to an M7.9. The flare sequence starts with an M3 while the log(R) is still rising but already has a high value. After a peak on 19 June, the log(R) begins to decrease while the flares release magnetic energy from AR 12371. As also visible in Figure 15, in which all parameters taken in consideration are in qualitative agreement with the log(R) values, the eruptive potential of AR 12371 remains high for the whole period taken into account. The trend over 24h has a minor decrease well after the flare eruption. In particular, the zoom on the log(R) value close to the flare event plotted in Figure 14 shows that the flare probability stays the same after the event, with a similar behavior as those reported in Figure 2 for the multifractal parameters. This supports the conclusions reported in Section 2.1, stating that there is little or no evidence at all of a change in configuration of the magnetic field at the photospheric level associated with the flare.

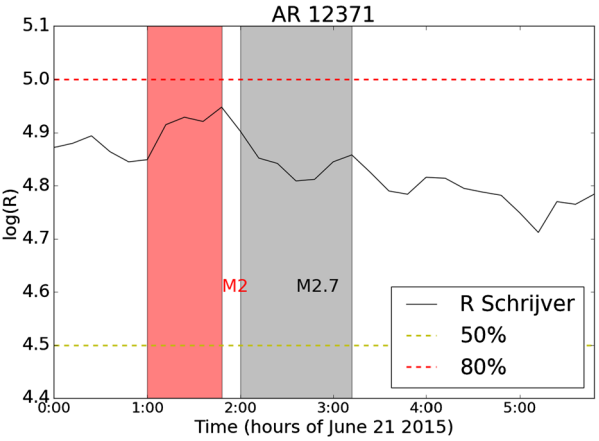

Figure 14 log(R) parameter as a function of time. We here concentrate on the initial hours of 21 June 2015. We report the probability of a flare > M1 occurring in the next 24 hours based on Schrijver (2007). *Shaded areas*: Flares > M1 produced by AR12371; in *red* we show the flare investigated in this article.

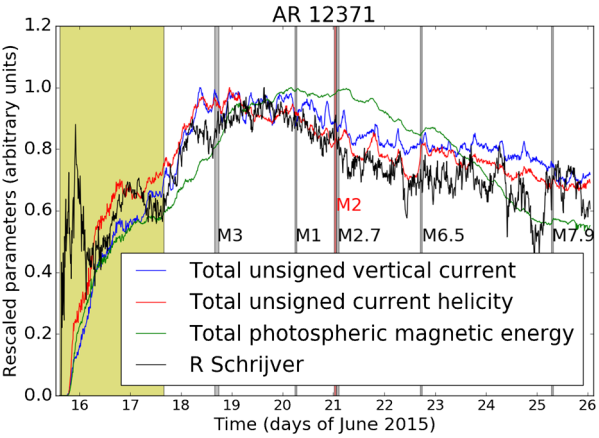

Figure 15 Rescaled parameters as a function of time. We rescaled all the parameters to unity in order to compare the trends. *Shaded yellow area*: Solar longitude > 60°. *Shaded gray* and *red*: Flares > M1 produced by AR12371.

4. Associated Halo CME of 21 June 2015

As we mentioned, during the 21 June 2015 event, none of the space-based coronagraphs onboard the STEREO spacecraft were acquiring data. Nevertheless, the LASCO-C2 and -C3 visible-light coronagraphs onboard SOHO acquired a very nice sequence of images showing the halo CME and the CME-driven shock expanding toward Earth. In particular, during the event, the LASCO-C2 coronagraph (with a FOV from 2 to 6 solar radii) acquired images with the orange filter (O, $\sim 540-640$ nm) at 02:36 UT (the last frame just before the CME enters the LASCO-C2 FOV) and at 02:48, 03:12, 03:24, and 03:36 UT. This sequence clearly shows the early expansion of the halo CME, as well as the propagation of the CME-driven shock ahead of the CME front. The subsequent expansion of the CME was captured higher up by the LASCO-C3 coronagraph (with a projected FOV from 3.6 to 33 solar radii), which acquired images with the O filter at 03:06 UT (the last frame just before the CME enters the LASCO-C3 FOV) and at 03:18, 03:12, 03:24, and 03:36 UT. This sequence shows the interplanetary expansion of the halo CME very well.

Based on standard LASCO running-difference sequences, this event has been preliminarily analyzed in different automatic and semi-automatic CME catalogs, such as the Solar Eruptive Events Detection System (SEEDS), Computer Aided CME Tracking (CAC-

Tus), coronal image processing (CORIMP), and the Coordinated Data Analysis Workshop (CDAW) catalogs available online. In particular, the SEED catalog gives on average (after linear fitting of the automatic determination of the CME front location in two LASCO-C2 frames) a projected plane-of-sky speed of ~ 1000 km s^{-1}. The other two catalogs provide broad and quite complex velocity distributions depending on the considered feature along the expanding CME front. The CACTUS catalog divided the event into two partial-halo fronts and provided median velocities of (980 ± 300) km s^{-1} and (840 ± 300) km s^{-1} for the upper and lower half of the halo-CME front, while the CORIMP catalog provides clear filtered LASCO-C2 and C3 composite movies of the event, as well as time-distance, time-velocity, and time-acceleration curves for different position angles along the CME front. According to the CORIMP catalog, the CME slightly accelerated ($a \simeq 150$ m s^{-2}) during the early expansion phase (between ~ 3 and ~ 6 UT), and then slightly decelerated ($a \simeq -150$ m s^{-2}) higher up in the LASCO-C3 FOV. This results in a projected speed that increases to $\sim 600-1100$ km s^{-1} around ~ 6 UT and then progressively decreases to a terminal speed between $\sim 200-500$ km s^{-1}. The CDAW catalog estimates (with linear fitting of the CME front location in LASCO-C2 and -C3 images) a CME starting time at 02:06:49 UT, which agrees very well with the occurrence of the M2.6-class flare.

Very interestingly, the LASCO-C2 instrument acquired a polarized sequence just at the right time when the CME front crossed the instrument FOV. In particular, the three images of the polarized sequence were acquired at 02:54:08 UT (polarization angle $+60$ degree), 02:57:58 UT (polarization angle 0 degree), and 03:01:48 UT (polarization angle -60 degree). Moreover, another polarized sequence was acquired just a few hours before the CME, and in particular, on 20 June at 21:00:03 UT (polarization angle $+60$ degree), 21:03:53 UT (polarization angle 0 degree), and 21:07:43 UT (polarization angle -60 degree). All these images, with a size of 512×512 pixels, were acquired with an exposure time of 100 s. This allowed us to perform the polarization ratio analysis of this event and to determine the 3D distribution of the emitting plasma. As was first pointed out by Moran and Davila (2004), because of the Thomson scattering geometry, the ratio between the polarized, pB, and unpolarized, uB, white-light brightness for a single electron is dependent only on its location along the LOS. For any coronal feature, the ratio pB/uB has a more complex dependence on the distribution of the electron density integrated along the LOS (Bemporad and Pagano, 2015), and the possibility that the feature is located near the plane of the sky makes the interpretation of the results more complex. On the other hand, for a halo CME, the computation has some simplifications because the emitting CME plasma is located almost entirely ahead or behind the plane of the sky. In our analysis, we first derived base-difference pB and uB images (see Figure 16, left panel) neglecting all the pixels where the difference was negative, in order to isolate only the pixels with additional emission due to the CME expansion and/or compression. From the observed pB/uB ratio, we then determined the location z of the emitting plasma along the LOS with the standard technique described by Moran and Davila (2004).

The resulting map of z values is shown in Figure 16 (right panel). This map suggests a correlation between distances ρ from the Sun projected on the plane of the sky and distances z along the LOS, indicating that the reconstructed cloud of 3D points has a distribution similar to the surface of a cone with vertex located on the CME source region on the Sun and axis parallel to the LOS. In order to better understand the resulting 3D structure of the halo CME, we built bar-plots (Figure 17) showing the distribution of plane-of-sky (POS) distances, ρ (top left panel), LOS distances, z (top right), and the distribution of polar angles, ϕ on the POS (bottom left), and of angles, θ from the POS. These plots show that the points where the polarization ratio technique is successful are distributed quite homogeneously in

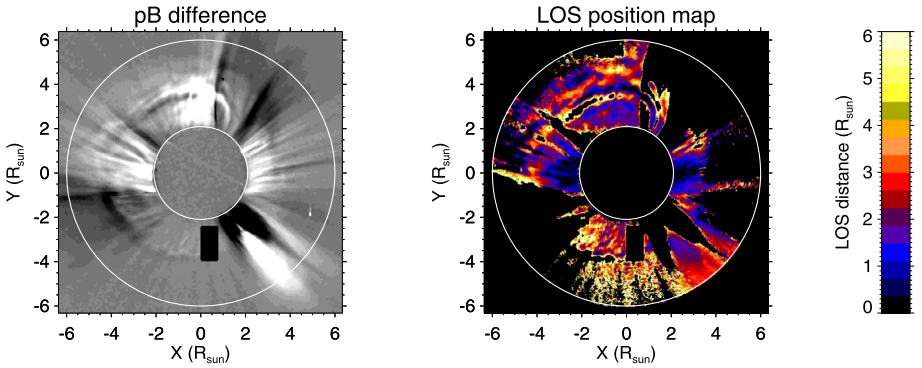

Figure 16 *Left panel*: Difference between the pB image acquired during the halo CME (polarized sequence acquired on 21 June between 02:54 and 03:02 UT) and the last pB image available before the eruption (polarized sequence acquired on 20 June between 21:00 and 21:08 UT). Negative values (*black*) have been excluded in the polarization ratio analysis to consider only pixels (*white*) where the CME transit leads to a density increase. *Right panel*: Map of the position along the LOS of the density increases associated with the CME as obtained with the polarization ratio technique (see text).

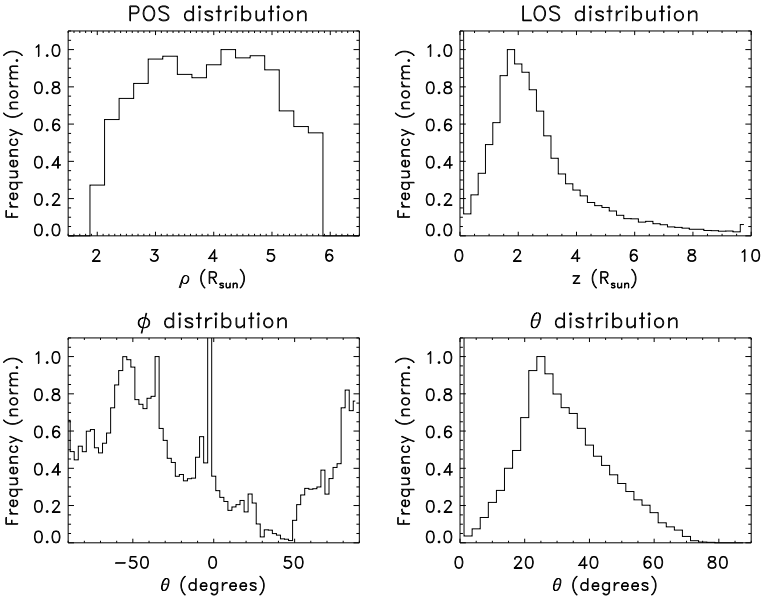

Figure 17 Bar-plots showing the distributions (as obtained from the polarization ratio) in the analyzed pixels of the emitting plasma located on the POS (*top left*), along the LOS (*top right*), at the latitude angles ϕ of these points (*bottom left*), and at their θ angles with respect to the POS (*bottom right*).

projected distance on the POS and less homogeneously in polar angle; moreover, the bulk of reconstructed points is located at a distance of about 2 solar radii from the POS and they are expanding at an angle from that plane of about 25°. We point out that a great source of uncertainty is related with the total time required to acquire the whole polarized sequence in about 7 m 20 s with an M7/3B flare at 08:16 UT; during this time, any CME feature with

projected speed of 1000 km s^{-1} moved by $\sim$600 arcsecs, corresponding to $\sim$25 pixels (for a 512 $\times$ 512 pixel LASCO-C2 image).

All the above information derived from white-light images is crucial to predict the CME arrival time at 1 AU and to study the CME interplanetary propagation. For instance, a simple estimate of the ICME arrival time at 1 AU can be determined by using the online forecasting tool provided by the Hvar Observatory (http://oh.geof.unizg.hr/DBM/dbm.php) and described by Žic, Vršnak, and Temmer (2015). The tool runs a 1D drag-based model given some input parameters. In particular, we can assume that (as provided by the CORIMP catalog) the CME was at a projected altitude of 25 solar radii on 21 June around 08:00 UT with a projected speed of about 300 km s^{-1}. These quantities can be deprojected using the propagation angle of 25° from the POS as we determined for the halo-CME front: in this way, we estimate that on 21 June 08:00 UT, the CME front was at a deprojected altitude of 25 $R_{sun}/\cos 25° \simeq 27.6$ R_{sun} with a deprojected speed of 330 km s^{-1}. With these input parameters, by also assuming a background solar wind speed of 400 km s^{-1} as measured by the *Advanced Composition Explorer* (ACE) spacecraft in the days before the eruption, the propagation tool provides an estimated arrival time on 25 June 19:04 UT (by assuming the lowest allowed value for the drag parameter of $\Gamma = 0.1 \times 10^{-7}$ km^{-1}). This is much later than the observed arrival time of the interplanetary shock. In particular, ACE observed the arrival of the shock on 22 June $\sim$18 UT. This early arrival time can be reproduced by the drag-based model only by assuming (again with the lowest allowed value for the drag parameter) an initial speed at 1 R_{sun} equal to 1440 km s^{-1}; this very high velocity is likely compatible only with the shock propagation velocity. The possible reasons for these discrepancies are hard to understand. The drag-based model is a simplified and semi-empirical description of the magnetic drag forces acting on ICMEs, whose physical origins are not understood. Moreover, the overall 3D geometry of the ICME and how this evolves during the interplanetary propagation are basically unknown, and this information is of fundamental importance for the reliability of this type of predictions; a much better knowledge could be provided by stereoscopic observations provided by the STEREO *Heliospheric Imager* (HI) instruments, but these data were not available for this specific eruption, as mentioned in the Introduction.

5. The 21 June 2015 SEP Event

An SEP event was observed on 21 June 2015, which can be associated with the M2.6 flare (peak time on 21 June at 02:36 UT) occurring in AR 12371, located at N13 W00, and the concomitant full-halo CME at 02:36 UT. This SEP event was also accompanied by Type II and Type IV radio bursts, indicating the presence of a propagating interplanetary shock, and Type III radio signatures.

At geosynchronous orbit, the *Energetic Proton, Electron and Alpha Detector* (EPEAD) fluxes sensor of the GOES satellites recorded an increase in the proton and electron fluxes. The top panel of Figure 18 shows the flux profiles for protons of energies >10, >30, and >60 MeV. The observed proton fluxes at all of the energy channels show a gradual rise in the prompt phase (as expected for a central meridian event) and a maximum value. On the other hand, the following decrease is quite slow at >10 MeV and sharp at high energies (>30 and >60 MeV). Specifically, the >10 MeV proton flux crossed the 10 pfu threshold (*i.e.* start of the SEP event according to the NOAA definition) at 21:35 UT on 21 June, reached the maximum flux value of 1070 pfu at 19:00 UT on 22 June, and fell below 10 pfu (end of the SEP event) at 07:05 UT on 24 June. The observed enhancement around the peak

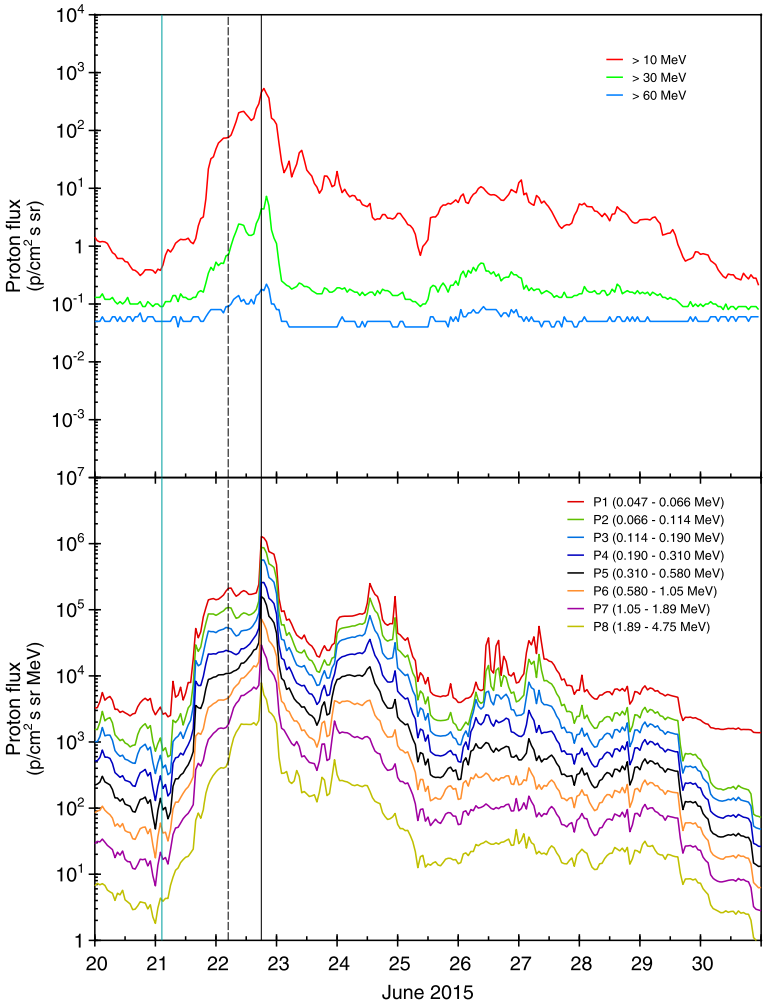

Figure 18 Temporal behavior of the proton integral (*top*) and differential (*bottom*) flux as recorded in different energy channels (energy reported in the legend) by EPEAD/GOES and EPAM/ACE, respectively, during the 21 June SEP event (http://omniweb.gsfc.nasa.gov). The *cyan*, *dashed black*, and *solid black lines* mark the time of the associated flare maximum, the 19 June CME-driven shock, and the 21 June CME-driven shock at ACE, respectively.

value at 19:00 UT (on 22 June), which reaches the strong radiation level (S3, according to the NOAA definition) is due to a shock arrival at Earth. At 17:59 UT (vertical black line in Figure 18) on 22 June, a shock was observed in ACE spacecraft solar wind and magnetic field data, driven by the 21 June CME, and an SI was registered at 18:37 UT at Earth (see Section 9.1). In addition, the enhancement around the proton flux local peak at 11:00 UT on 22 June could be the effect of a small shock (related to a previous CME on 19 June), which was observed at 04:51 UT (vertical dashed black line in Figure 18) at the ACE spacecraft location, followed by a geomagnetic SI at 05:49 UT. Note that the 21 June 2015 SEP event did not extend to very high energies (> 100 MeV), as discussed in the following subsection.

The bottom panel of Figure 18 depicts the particle flux recorded by the *Low Energy Magnetic Spectrometer* of the *Electron, Proton and Alpha Monitor* (EPAM) onboard the ACE spacecraft in differential energy channels from 0.047 to 4.75 MeV/n. It is apparent that the SEP event almost matches the > 10 MeV time profile at lower energies.

Another greater-than-10 MeV proton event can be distinguished in Figure 18, starting at 03:50 UT on 26 June (in association with an M7/3B flare at 08:16 UT on 25 June from AR 12371), reaching a maximum of 22 pfu (S1, minor) at 00:30 UT on 27 June, and ending 07:55 UT (on 27 June).

5.1. High-Energy Observations and the PAMELA Instrument

The PAMELA (Adriani *et al.*, 2014) instrument provides the opportunity to extend the analysis of the SEP event to higher energies.

For the analysis of the 21 June 2015 solar event with PAMELA, a preliminary real-time data reduction has been used, together with the standard data selection criteria reported in Adriani *et al.* (2011). We selected events that did not produce secondary particles in the first two scintillator planes and in the tracker, with a single fitted track within the spectrometer fiducial acceptance. We also required the absence of hits in the anticoincidence plates. Using the timing information of the time-of-flight (ToF) system to evaluate the velocity of the incoming particle and by requiring a positive value of the velocity itself, we rejected particles coming from the bottom of the apparatus, which may be part of a population of particles trapped in the geomagnetic field and not directly coming from the Sun. To reinforce this condition, constraints on the geomagnetic cutoff were added. Finally, proton selection was carried out using the information on the energy loss inside the tracker planes and the Bethe–Bloch formula.

Figure 19 shows the preliminary rate of protons measured by PAMELA in three rigidity channels (from 450 MV to approximately 1500 MV) collected every three hours. To allow an easier comparison, we also depict the integrated proton flux data from the GOES 15 (see http://satdat.ngdc.noaa.gov/sem/goes/) spacecraft in three lower energy channels. The vertical line represents the time of the maximum (02:36 UT) of the associated M2.6 flare on the Sun. From the time-profiles of the particles, some features can be inferred. The flux profiles show a relatively slow rise to the maximum, as the SEP event originates from a central portion of the solar disk. Moreover, the PAMELA rate shows a little energy extension, falling into background above ~ 600 MV (black circles in the bottom panel of Figure 19); this means that a small number of particles have reached the distance of 1 AU, and this may be linked to the fact that the event itself was not powerful enough to accelerate particles beyond this threshold. As stated in the previous section, the two main peaks visible in the GOES observations are possibly related to two different shocks.

From these data, we can also obtain some more information regarding the CME generated during the event. The PAMELA highest energy rate counts suggest a Forbush decrease after 23 June (Forbush, 1937; Cane, 2000) which is due to the interplanetary counterpart of the full-halo CME leaving the solar surface at about 02:30 UT of 21 June.

The Forbush decrease was also observed by the worldwide neutron monitor (NM) network. For instance, the Rome NM (geographic coordinates: 41.86°N, 12.47°E, sea level; effective vertical cutoff rigidity – Epoch 1995: 6.27 GV) registered a variation of about 5% in the cosmic-ray intensity, as displayed in Figure 20 (from http://webusers.fis.uniroma3.it/svirco/Dati).

Figure 21 shows the event-integrated differential proton flux as a function of rigidity measured by PAMELA in the time interval 22 – 23 June with respect to the galactic flux

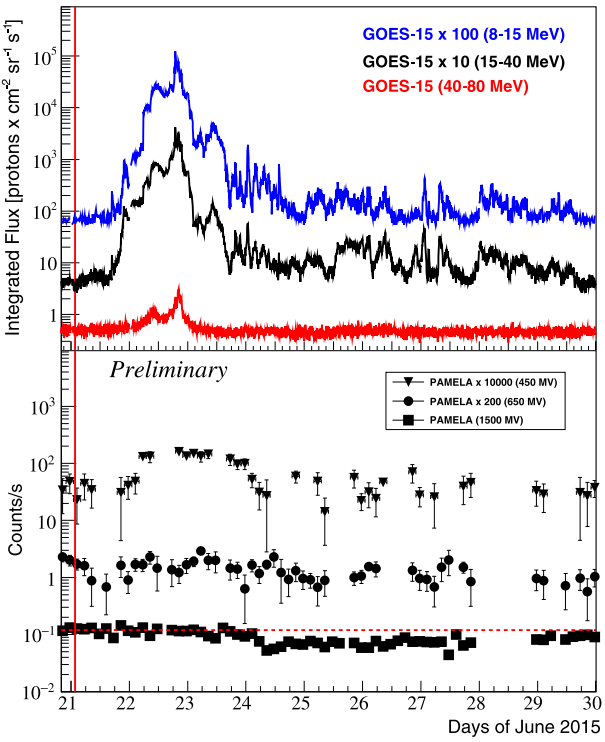

Figure 19 GOES proton fluxes as a function of time in three energy intervals is presented in the *top panel*. In the *bottom panel*, PAMELA counts per second are shown for three different rigidity channels. The *vertical line* indicates the time of maximum of the M2.6 flare on the Sun, while the *horizontal line* highlights the almost undisturbed ∼1500 MV count rate plus the Forbush decrease created by the halo CME associated with the flare. The longer data sampling for PAMELA (3 hours) with respect to the GOES sampling (only 32 seconds) is due to both statistical and orbital limitations. The latter are caused by the magnetic cutoff threshold that blocks the arrival of very low energy particles in specific regions of Earth. Data from PAMELA are preliminary.

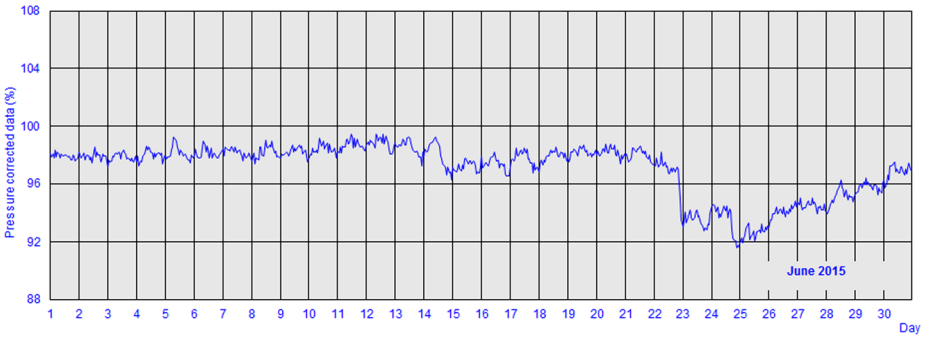

Figure 20 Time history of the cosmic-ray intensity recorded at the Rome NM (SVIRCO Observatory) for June 2015.

measured in the first 20 days of June. Both fluxes are scaled to better show the amount of the increase due to the 21 June SEP event.

5.2. 21 June 2015 SEP Event Forecasting

The forecast of the 21 June 2015 SEP event is provided using the ESPERTA model (Laurenza *et al.*, 2009; Alberti *et al.*, 2017a). The inputs of the model are three solar parameters, *i.e.* the associated flare location, the 1 – 8 Å soft X-ray (SXR) integrated intensity, and ∼1 MHz Type III time-integrated intensity to give a warning for the occurrence of an

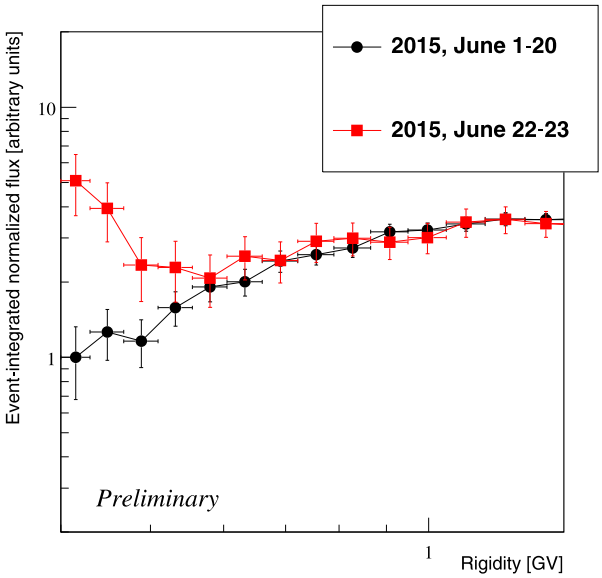

Figure 21 Normalized event-integrated proton flux in the interval 22 – 23 June (*red squares*) as a function of rigidity, superimposed on the background proton flux from 1 to 20 June (*black circles*).

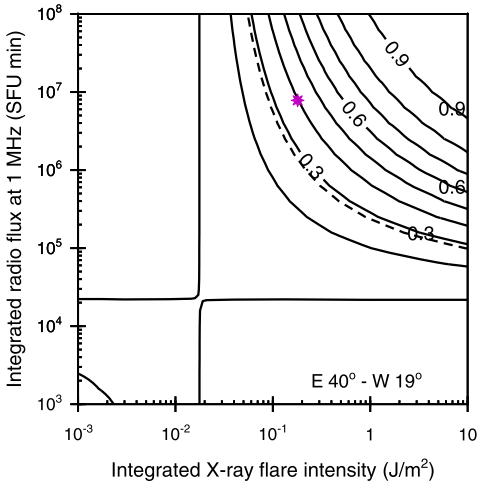

Figure 22 Integrated 1 MHz radio intensity *versus* integrated 1 – 8 Å soft X-ray intensity for > M2 soft X-ray flares located in the longitude range E40–W19: *solid lines* represent the probability contours, the *dashed line* is the probability threshold, and the *magenta asterisk* corresponds to the values obtained for the X-ray flare associated with the 21 June SEP event.

SEP event within 10 min following the flare maximum. The time-integrated SXR intensity is performed between the points corresponding to one-third of the power before and after the X-ray peak, while, because of the lower regularity of the radio emission, the radio time-integration starts 10 min before the time of the SXR integration until 10 min after the X-ray peak (see Laurenza *et al.* (2009) and Alberti *et al.* (2017a) for more details).

Figure 22 shows the probability contours (solid lines) for SEP forecasting obtained by Laurenza *et al.* (2009), Alberti *et al.* (2017a) as a function of the time-integrated radio intensity at 1 MHz and the time-integrated X-ray flare intensity for the flare longitude range E40 – W19. The dashed line represents a threshold for the occurrence of an SEP event: if the values of the associated flare parameters are located above the curve, an SEP event is predicted to occur; if they are below the curve, no SEP event is expected. The values ob-

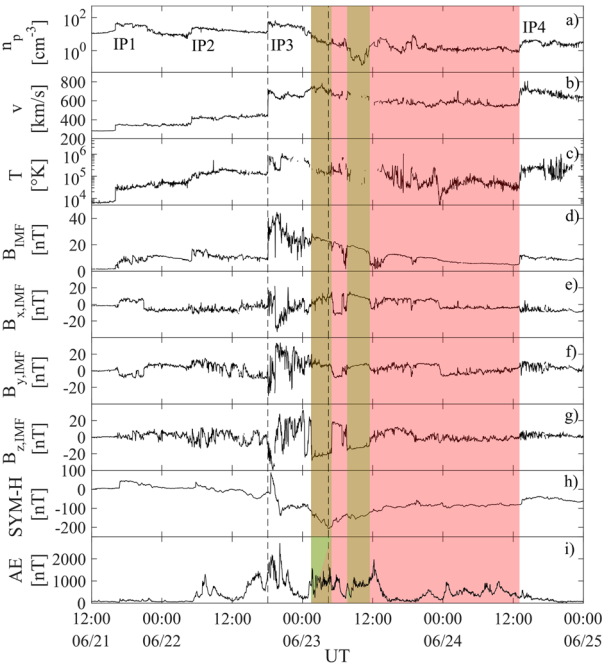

Figure 23 Solar wind parameters as measured at L1 by the *Wind* spacecraft: **a**) proton density, **b**) velocity, **c**) proton temperature, **d**) IMF intensity, and **e–g**) IMF x, y, z components in geocentric solar ecliptic (GSE) coordinate system. **h**) and **i**): The SYM-H and AE indices, respectively, between 21 June and 24 June 2015. The two *dashed lines* indicates the ICME associated shock as observed by *Wind* on 22 June at 17:59 UT (IP3) and the minimum values reached by SYM-H during the storm main phase on 23 June at 04:27 UT. The *white area* behind the IP3 shock is the sheath (Burlaga *et al.*, 1981), while the *red shaded region* corresponds to the overall ejecta interval. The *greenish shaded regions* show two small magnetic clouds and/or flux ropes identified within the ICME (Tsurutani *et al.*, 1988).

tained for the M2.6 flare (with a longitude of W00) associated with the 21 June SEP event are 0.16 J/m^2 for the SXR fluence and 7.8×10^6 sfu $\times$ min for the $\sim$ 1 MHz Type III time-integrated intensity. Figure 22 shows that they are higher (see the magenta asterisk) than the probability threshold. Hence, a positive forecast is issued at 02:46 UT (10 min after the SXR peak) for the 21 June 2015 SEP event, with a leading time of $\sim$ 19 hours before the actual occurrence of the SEP event at 21:35 UT.

6. Analysis of the Interplanetary Medium as Observed by *Wind*

Figure 23 shows the ICME signatures obtained by the *Wind* spacecraft located at the Lagrangian L1 point. A cluster of interplanetary (IP) shocks passed *Wind* at 16:05 UT on 21 June (IP1), 05:02 UT (IP2) and 18:07 UT(IP3) on 22 June, and 13:12 UT (IP4) on 24 June, respectively. Liu *et al.* (2015) showed that the first shock was driven by the 18 June CME, while the second shock was associated with a CME from 19 June. Moreover, they showed that the ICME (and its preceding shock – IP3) were produced by the 21 June CME, and the fourth shock (IP4) was associated with the 22 June CME. The 23 June ICME boundaries are determined taking into account the magnetic field in conjunction with the proton temperature (panel c) and density (panel a). Indeed, between 23 June 01:29 UT and 24 June 13:04 UT, a decrease in the temperature coupled with a smooth rotation of the magnetic field can be seen (Zurbuchen and Richardson, 2006). The presence of current sheets was suggested by a series of dips in the magnetic field strength that are observed inside the ICME. Liu *et al.* (2015) explained that this signature was due to the heliospheric current sheet (Smith, Tsurutani, and Rosenberg, 1978) cutting through the ejecta, which may lead to a chain of small flux ropes within the ICME.

7. Magnetospheric Response

The impact of the two magnetic clouds produces several effects on the magnetosphere–plasmasphere system by generating magnetic field variations, destabilizing magnetospheric current systems, particle injection, and precipitation. These effects can be investigated using different datasets related to *in situ* measurements of fields and particles.

7.1. The Response to the 21 June 2015 ICME at Geosynchronous Orbits

Figure 24 shows the solar wind (SW) and the IMF observations by *Wind* (Figure 24a) and the magnetospheric field observations at geosynchronous orbits (Figure 24b) by the GOES 13 (LT = UT-5, where LT stands for local time) and GOES 15 spacecraft (LT = UT-9). The IP3 shock was observed by *Wind* on 22 June 2015, ∼ 18:07 UT, located (in GSE coordinates indicated by the subscript SE) at $X_{SE} \sim 203.0\ R_E$, $Y_{SE} \sim -34.1\ R_E$, and $Z_{SE} \sim -11.0\ R_E$. It was characterized by a remarkable variation in SW pressure ($\Delta P_{SW} \sim 31.5$ nPa) and IMF strength ($\Delta B_{IMF} \sim 22.3$ nT), associated with a relevant increase of the southward IMF component ($B_{z,IMF} \sim -20.0$ nT), persisting for ∼ 90 min. According to the Rankine–Hugoniot relations, the shock normal was oriented at $\Phi_{SE} \sim 186°$, $\Theta_{SE} \sim -9.8°$, and the estimated shock speed was $V_{Sh} \sim 770\ km\,s^{-1}$. Consequently, the shock impact onto the magnetosphere was predicted at ∼ 18:34 UT (∼ 27 min after the *Wind* observations). The SI at geosynchronous orbits was observed by both GOES spacecraft at ∼ 18:33 UT (Figure 24b), more clearly in the magnitude of the magnetic field. Interestingly, GOES 13 and GOES 15 observed a small and rapid enhancement in the B_z ($B13_z$ and $B15_z$ in the geocentric solar magnetospheric (GSM) coordinate system) component (associated with the field compression), preceding a sharp transition from ∼ 100 nT to ∼ −100 nT; at the same time, the other components underwent strong variations. According to Suvorova *et al.* (2005), Dmitriev *et al.* (2005), these features are indicative of magnetopause crossing. On the other hand, according to Shue *et al.*'s (1998) model, the magnetopause nose is expected to move inward up to ∼ 4.9 R_E based on the extreme values of the SW parameters. Figure 24c shows the predicted configuration of the magnetospheric field lines in the noon/midnight plane before (black lines) and after (red lines) the shock impact (TS04 model, Tsyganenko and Sitnov, 2005) and reveals the extreme field compression in the period of interest. Figure 25 (top panel) shows the southward orientation of the $B_{z,IMF}$ between 18:33 – 19:50 UT. Correspondingly, GOES 13 (central panel) and GOES 15 (bottom panel) show, in conflict with the northward orientation expected in the wide noon region, a strongly negative orientation at a geosynchronous orbit. This feature can be interpreted in terms of a relevant erosion of the magnetosphere caused by the strong southward component of $B_{z,IMF}$ observed in the corresponding interval. In particular, the correlation coefficients between the two B_z ($B13_z$ and $B15_z$) components observed by geostationary spacecraft and $B_{z,IMF}$ are $r_{13} = 0.89$ at GOES 13 and $r_{13} = 0.93$ at GOES 15, respectively. On the other hand, in this time interval, GOES 13 was located between 13:40 – 15:10 LT and GOES 15 between 09:40 – 11:10 LT, suggesting a way out of both spacecrafts into the transition region.

7.2. Plasmasphere Dynamics

Of the large variety of phenomena produced in the magnetosphere by a geomagnetic storm, a very important one is the significant effect on the cold and dense plasma located in the inner magnetosphere (the plasmasphere). This region, populated by the outflow of ionospheric plasma along low- and mid-latitude field lines (Chappell, Harris, and Sharp, 1970; Lemaire

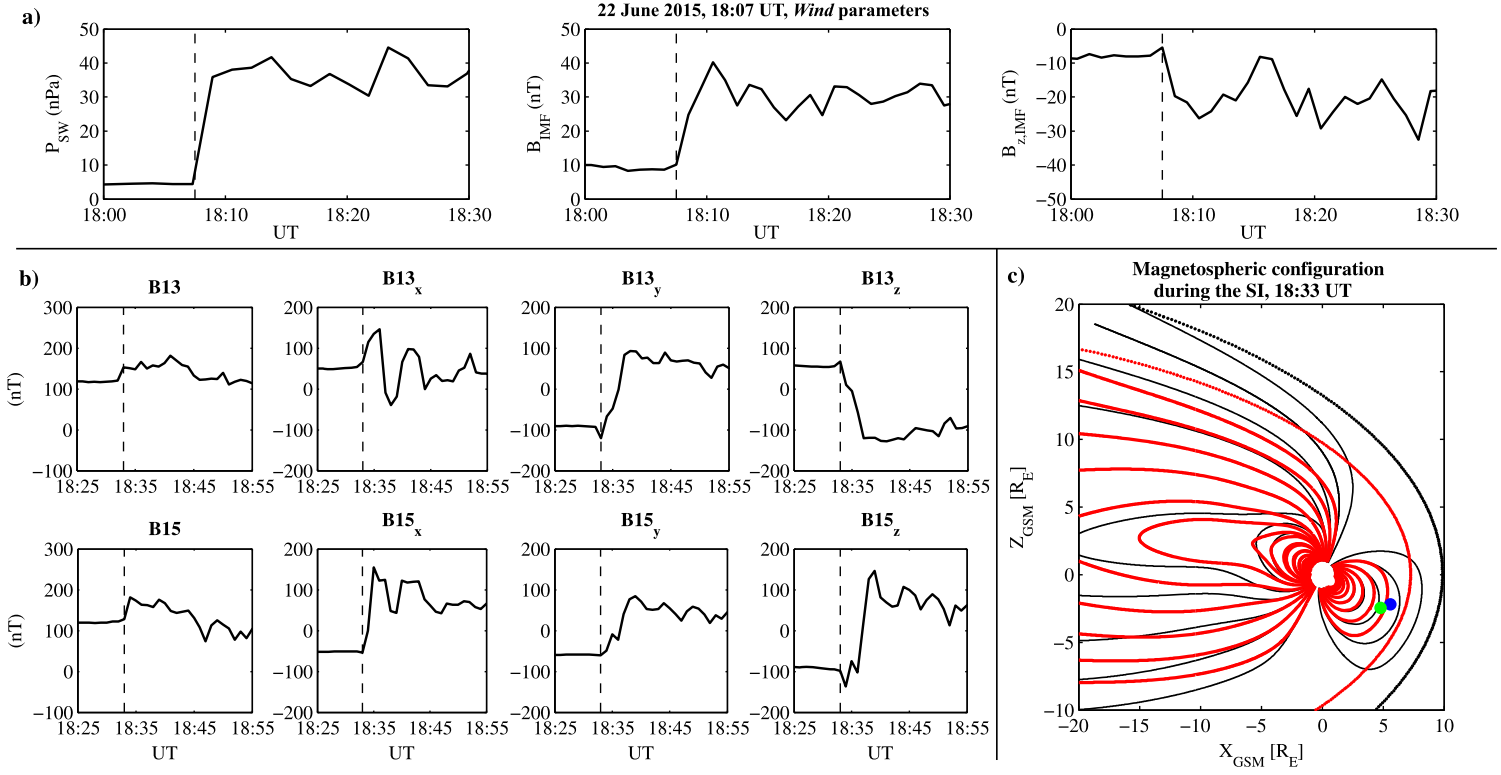

Figure 24 SW parameters as measured by *Wind*. (**a**): Dynamic pressure, total magnetic field, and Z component, in GSM coordinates, of the IMF. (**b**): Magnetic field magnitude and components in the GSM coordinate system as measured by GOES 13 and GOES 15. (**c**): Position of the two geosynchronous satellites and the magnetospheric configuration before (*black lines*) and after (*red lines*) the shock impact.

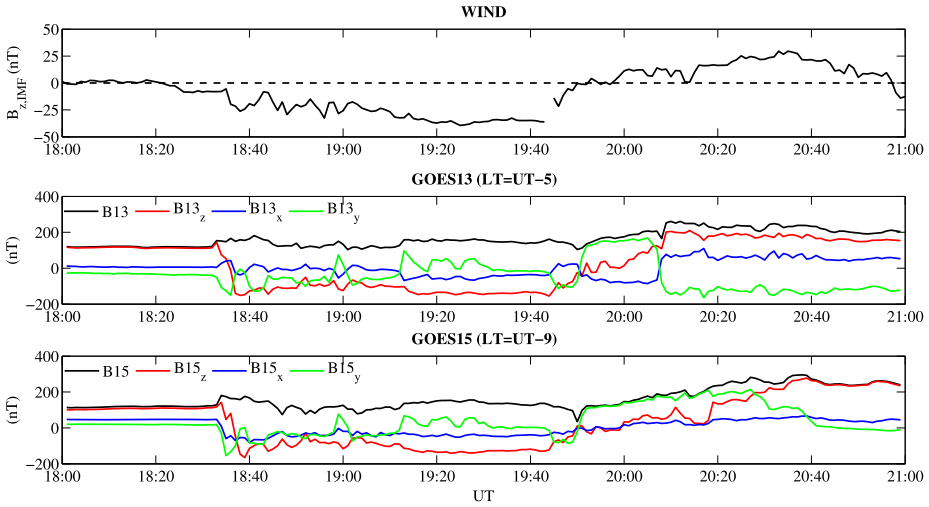

Figure 25 *Top panel*: Z component of the IMF in GSM coordinates shifted by 27 min. *Central panel*: Magnitude of the magnetic field (*black line*), the X component (*red line*), the Y component (*blue line*), and the Z component (*green line*) in the GSM coordinate system for GOES 13. *Bottom panel*: Same for GOES 15.

et al., 2005), approximately corotates with the Earth and typically extends up to $4-5\ R_E$. There is often an abrupt transition (plasmapause) between the dense plasma of the plasmasphere and the more tenuous plasma of the plasmatrough, which is generally convected toward the dayside magnetopause by a large-scale electric field imposed across the magnetosphere by the interaction of the solar wind with the magnetosphere. During a GS, the magnetospheric convection intensifies, and consequently, the plasmasphere is eroded and the plasmapause moves closer to Earth. The plasma concentration inside the new boundary is also subjected to significant variations, either a decrease or an increase, depending on different competing processes.

These phenomena have been mostly investigated in the past years by *in situ* measurements (Moldwin, 1997) or by whistlers recording on the ground (Carpenter, 1963; Park, 1973). An alternative, more recent, remote-sensing technique is based on the detection of geomagnetic field line resonances (FLR) by means of a pair of magnetometer stations slightly separated in latitude (Menk *et al.*, 2014). Cross-phase and amplitude-ratio analysis of the ultra low frequency (ULF) signals recorded at the two stations are used to determine the eigenfrequencies of the field line crossing the midpoint of the station pair (Baransky *et al.*, 1985; Waters, Menk, and Fraser, 1991). The FLR frequency determined in this way (usually the fundamental frequency) is converted into an estimate ρ_{eq} of the cold plasma mass density at the equatorial point of the field line (r_{eq}). This is done by solving magnetohydrodynamic (MHD) wave equations under an appropriate geomagnetic field model and assuming a reasonable profile of the normalized density distribution, ρ/ρ_{eq}, along the field line (Vellante, Piersanti, and Pietropaolo, 2014; Vellante *et al.*, 2014).

By means of a latitudinally extended network of stations, it is then possible to monitor both temporal and spatial variations of the cold plasma mass density in a considerable portion of the magnetosphere. To this purpose, we used the measurements provided by EMMA, a meridional network of 25 magnetometer stations extending from central Italy to the north of Finland ($36° < \lambda < 67°$, LT $\sim$ UT + 2 hour; Lichtenberger *et al.*, 2013). MHD wave equations were solved assuming the T01 Tsyganenko magnetic field model (Tsyga-

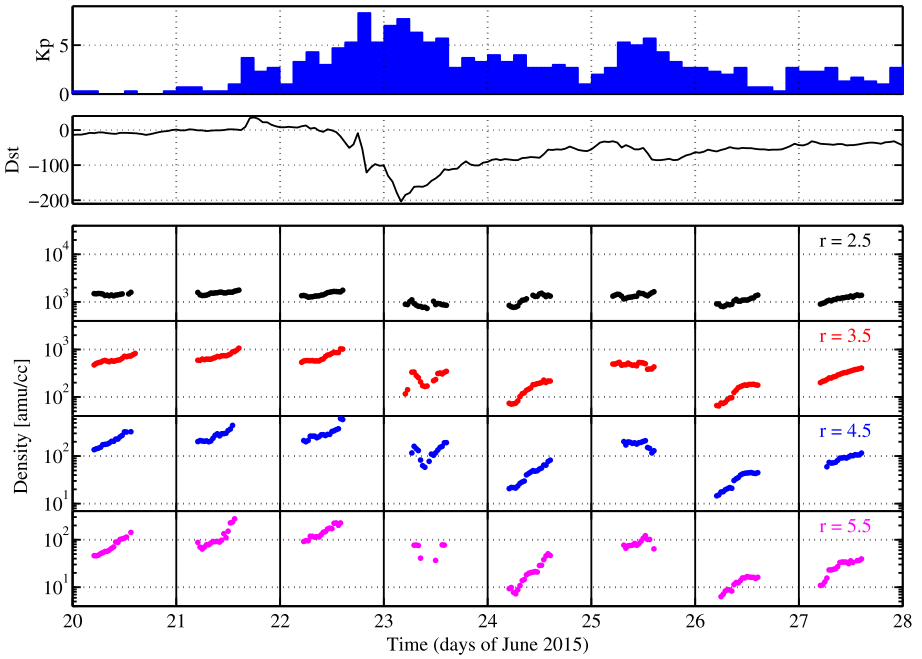

Figure 26 *From top to bottom*: Kp index, Dst index, and FLR-derived equatorial plasma mass densities at different Earth distances during 20 – 27 June 2015.

nenko, 2002) and the following radial dependence of the field aligned density distribution: $\rho/\rho_{eq} = (r/r_{eq})^{-1}$ (Vellante and Förster, 2006). As the equatorial densities derived from a given station pair may refer to a time-changing equatorial distance (especially at high latitudes and for disturbed magnetospheric conditions), ρ_{eq} values were determined at fixed radial distances by interpolating at each time the experimental data points by a smoothing spline curve.

Figure 26 shows the temporal variation of the inferred equatorial plasma mass density at $r = 2.5, 3.5, 4.5,$ and 5.5 R_E during 20 – 27 June 2015. The data cover only the dayside region ($\sim$07 – 17 LT), where FLRs are more efficiently excited and the evaluation of the FLR frequency (and the derived density) is more reliable.

Through 20 – 22 June, *i.e.* before the SI of 22 June (18:36 UT, marked by a distinct peak in Dst), a recurrent daytime pattern of the density is observed at each r value, characterized by a trend of increasing values through the day; this is more pronounced at higher radial distances. This daytime density increase is caused by the gradual refilling of the magnetospheric flux tubes by the ionosphere. These flux tubes are partially depleted during nighttime hours. We also note a day-to-day increase at 5.5 R_E, indicating that at this radial distance, the flux tubes are still in a phase of recovery following a previous event of high geomagnetic activity.

On 23 June, *i.e.* during the first stage of the storm recovery phase, the general level of density is significantly decreased by a factor of $\sim$2 everywhere, but the daily pattern is more confusing because of the rapid change in the magnetospheric field configuration and the competitive interplay between the refilling from the ionosphere and the depletion by the enhanced magnetospheric convection.

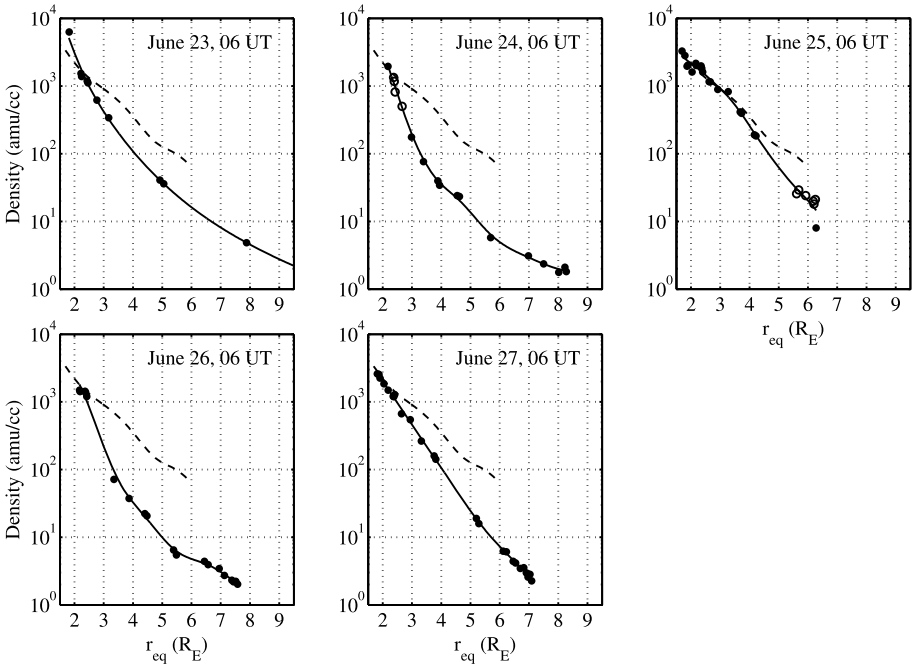

Figure 27 Radial profiles of the inferred equatorial plasma mass density at 06 UT (∼08 LT) for 23 – 27 June 2015. A smoothing spline curve (*solid line*) is drawn through the data points to guide the eye. The *dashed line* in each panel is the radial profile of 22 June, which is drawn as a reference profile representative of the pre-storm condition at the same hour. *Dots* are values derived by cross-phase maxima (typical situation), and *circles* are values derived by cross-phase minima (which are possible indicators of plasmapause).

On 24 June, the density at 3.5 – 5.5 R_E has further decreased (by a factor ∼5 – 7 with respect to 22 June), while at 2.5 R_E, it has returned to the typical pre-storm level. The significant plasma depletion also gives rise to a more pronounced daytime refilling process at all radial distances.

At the very beginning of 25 June there appears to be an almost complete recovery with respect to the same hours of 22 June, but the typical daytime refilling appears to be inhibited by a reintensified geomagnetic activity (see Kp and Dst behavior). The effect of this apparently milder reintensification of the geomagnetic activity gives rise to an even stronger plasma depletion on 26 June, with a density decrease of a factor ∼10 at 5.5 R_E. Moreover, the recovery from the plasma depletion event of 26 June is slower than that observed for the depletion event of 24 June: the median density on 27 June recovered to ∼90% of the pre-storm value at 2.5 R_E, ∼45% at 3.5 R_E, ∼35% at 4.5 R_E, and only ∼20% at 5.5 R_E.

Further information on the temporal-spatial variation of the plasma density is provided by the radial profiles shown in Figures 27 and 28. The profiles in Figure 27 are representative of the radial density variation on the morning side (∼08 LT), while those in Figure 28 correspond to the post-noon region (∼15 LT). A smoothing spline curve (solid line) is drawn through the data points to guide the eye. The dashed line in each panel is the radial profile of 22 June, which is drawn as a reference profile representative of the pre-storm condition at the same hour. This reference profile is well fit by the equation $\log_{10}(\rho) = 4.1 - 0.40r$ at 06 UT and $4.1 - 0.32r$ at 13 UT, which are typical of an extended plasmasphere (Carpenter and Anderson, 1992). We also note that the radial profiles for 23 – 27 June extend to distances

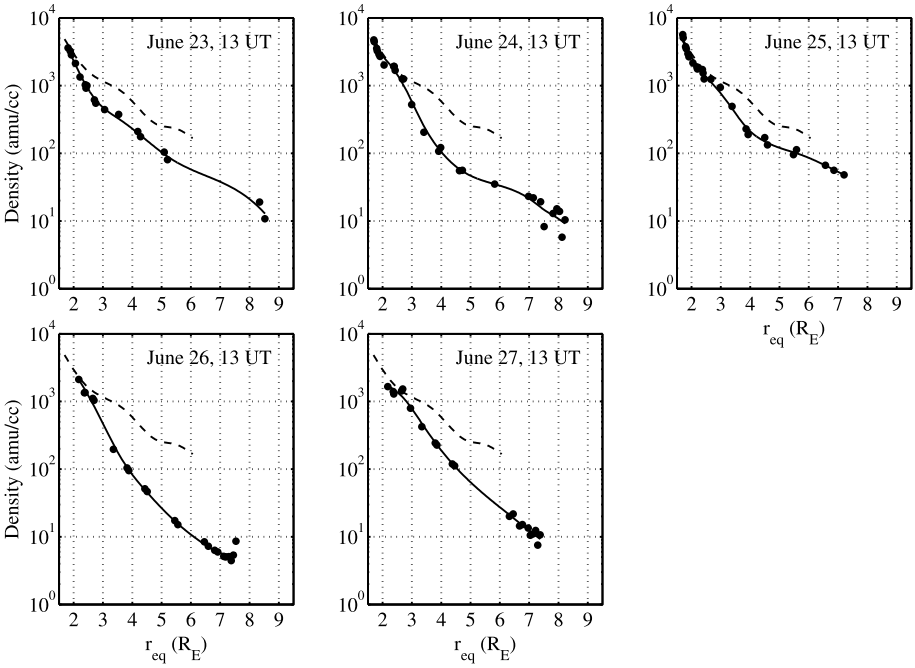

Figure 28 Same as in Figure 27, but at 13 UT (∼15 LT).

greater than the maximum distance (∼6 R_E) covered by the 22 June reference profile. The reason is that the solar wind and magnetospheric conditions for 23–27 June (in particular, the ring current effects) cause a significant field line stretching that is modeled by the T01 model (Berube, Moldwin, and Ahn, 2006).

The morning profile shows a dramatic change on 24 June with a steep density falloff starting from ∼2.2 R_E. This behavior is indicative of a plasmapause formation between 2–3 R_E. This is also confirmed by the detection of cross-phase reversals in the FLR analysis between 2.3 R_E and 2.7 R_E, which are indicated by circles. This circumstance occurs when the station pair maps an equatorial region where the radial density variation is steeper than r^{-8} as for the plasmapause (Kale *et al.*, 2007). On the next day (25 June), flux tubes up to ∼3.5 R_E completely recovered their plasma content, while for $r > 3.5$ R_E, there was still some level of depletion. There is also possible evidence of a plasmapause at 5–6 R_E. A new inward displacement of the plasmapause is visible on 26 June at a location (∼2.5 R_E) similar to that of 24 June. The results for 27 June confirm that in this case the recovery is slower.

The results for the post-noon region (Figure 28) are similar to those of the morning side, except for some evidence of a plasmapause on 24 June and 26 June located at a slightly higher distance. This is in agreement with empirical model predictions by O'Brien and Moldwin (2003).

8. Ionospheric Response

This section shows a detailed analysis of the ionospheric response to the ICME impact into the magnetosphere. We analyzed the flare effect on the ionosphere, the low-latitude

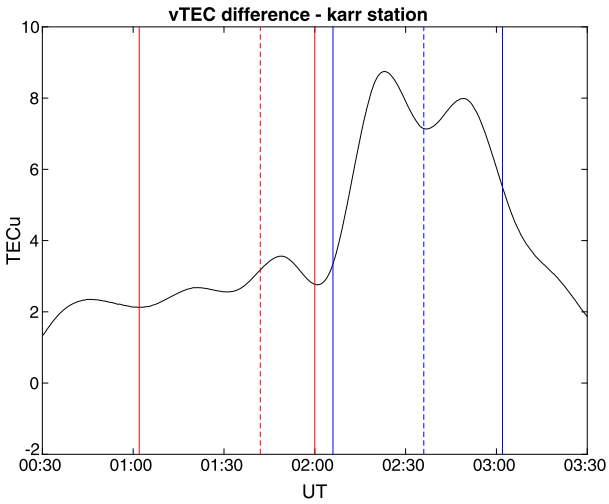

Figure 29 Difference between vertical TEC measured by the Karratha receiver (western Australia) on 20 and 21 June in the time range between 00:30 and 03:30 UT. The *red* and *blue solid lines* represent the beginning and the end of the two flares in UT, while the corresponding *dashed lines* represent the flare peaks in UT.

ionospheric response during the GS, and the high-latitude ionospheric convection pattern as detected by the *Super Dual Auroral Radar Network* (SuperDARN) in the northern polar regions.

8.1. Flare Effect on the Ionosphere

To catch the effect on the dayside ionosphere of the flares, difference values between the vertical total electron content (TEC) measured by the Karratha receiver (Australia, 20.98°S 117.10°E) on 20 June and on 21 June in the time range between 00:30 and 03:30 UT are reported in Figure 29. 20 June is taken as the reference for the quiet conditions. According to the timing reported in Table 1, red and blue solid lines represent the beginning and the end of the two flares in UT, while the corresponding dashed lines represent the flare peaks in UT. The Karratha receiver was selected because it is located below the dayside ionosphere (LT = UT + 8). The arrival of the two flares corresponds with an increase of the TEC difference, which is more pronounced for the second flare. For both flares, the vTEC differences also present a double-peak structure, again more evident for the second flare. These difference values are in agreement with Tsurutani *et al.* (2005), who in the case of the 2003 Halloween storm found vTEC differences of up to 22 TECu in correspondence with the surroundings of the subsolar points. In our case, the values are lower because of the different intensity of the flares characterizing the June 2015 storm with respect to those of the 2003 Halloween storm.

8.2. Low-Latitude Ionosphere

The low-latitude ionospheric response to the event under investigation was measured by means of three types of instruments: ionosondes, GNSS receivers, and the Langmuir probe onboard the *Swarm* satellites. Specifically, the assessment was made above the low-latitude regions of South America and Southeast Asia. These sectors were chosen because they are in opposite local time day and night sectors. The analysis is focused on the morphology of the crests of the equatorial ionospheric anomaly (EIA), which is strongly influenced by the disturbance of an electric field that is induced by geomagnetic storms (Muella *et al.*, 2010; Alfonsi *et al.*, 2013; Tulasi Ram *et al.*, 2016; Spogli *et al.*, 2016).

Concerning the ionosonde data, the critical frequency of the F2 layer (foF2) and the virtual height of the base of the F region (h′F) are considered for the Cachoeira Paulista (Brazil, 22.7°S, 315.0°E) and Sanya (China, 18.3°N, 109.4°E) ionosondes, which are located close to the southern and northern crest of the EIA, respectively. Both stations are equipped with a digisonde (Bibl and Reinisch, 1978). In June 2015, the sounding repetition rate and the sweeping frequency range were set to 15 min and 7.5 min, respectively, at Cachoeira Paulista and Sanya, and from 1 to 20 MHz. Data from both stations were downloaded from the Global Ionospheric Radio Observatory web portal (Reinisch and Galkin, 2011) and were then manually validated. For the GNSS, data from the South America sector are from the Brazilian Network for Continuous Monitoring of the Institute of Brazilian Geography and Statistics (RBMC/IBGE), while the Southeast Asian (SEA) sector data are from the International GNSS Service (IGS) network stations (www.igs.org). The TEC is obtained by applying the calibration technique introduced by Ciraolo *et al.* (2007) and detailed in Cesaroni *et al.* (2015) to GNSS code and carrier phase measurements. Plasma density data acquired by the *Swarm* constellation (Friis-Christensen *et al.*, 2008) were also used. In particular, data from satellite *Swarm Alpha*, orbiting at an altitude of about 470 km, provide evidence of the changes in the electron density distribution in the topside ionosphere. Following a similar approach as Spogli *et al.* (2016), the combined information provided by TEC from GNSS, *in situ* electron density from *Swarm Alpha* and the h′F from ionosondes allows identifying how the changes in the electric field influence the uplift and downdraft of the ionospheric plasma that result in a modification of the morphology of the EIA during storm time.

Plasma uplift and downdraft is mainly caused by ionospheric electric fields and currents that during geomagnetic disturbed periods can significantly differ from their quiet-day patterns at low and mid latitudes. This is due to a simultaneous action of two processes: the magnetospheric dynamo and the ionospheric disturbance dynamo (Blanc and Richmond, 1980).

Dynamic interactions between the SW and the magnetosphere are at the base of the magnetospheric dynamo. This mechanism generates electrical currents that with their associated electric fields (called prompt penetrating electric fields (PPEFs)) can reach the lower latitudes through the conducting ionosphere (Mannucci *et al.*, 2005; Huang *et al.*, 2007; Fejer, Jensen, and Su, 2008; Zhao *et al.*, 2008; Tsurutani *et al.*, 2008). Specifically, the interaction between the southward IMF and the Earth's magnetic field gives rise to significant dawn-to-dusk electric fields that may severely affect the terrestrial ionosphere. In particular, dawn-to-dusk electric fields are eastward in the daytime and westward at night, uplifting the ionosphere during the day and lowering it during the night (Tsurutani *et al.*, 2004). The ionospheric disturbance dynamo instead is generated by an energy input into the thermosphere that alters the global thermospheric circulation, modifying the electric fields and currents that are produced by the ionospheric wind dynamo action for quiet conditions at low and mid latitudes (Fejer and Scherliess, 1995; Fejer, Jensen, and Su, 2008; Nicolls *et al.*, 2006). The polarity and duration of the electric fields related to the disturbance dynamo can trigger uplifts and descents of the ionospheric plasma that are at the base of large-scale local time dependent increases and decreases of the TEC.

This is clear on the TEC maps that are calculated for the Brazilian and Southeast Asian sectors (Figures 30 and 31), which show a very different scenario. While the Brazilian sector is characterized by a suppression of the EIA on 23 June, the Southeast Asian sector shows an intensification of the EIA crests for the same day. Both scenarios are supported by *Swarm* data shown in Figure 32 and Figure 33.

Our explanation for this, following Tsurutani *et al.* (2004), is that the Southeast Asian dayside local time sector is closer to the interplanetary shock, and the ionospheric plasma is

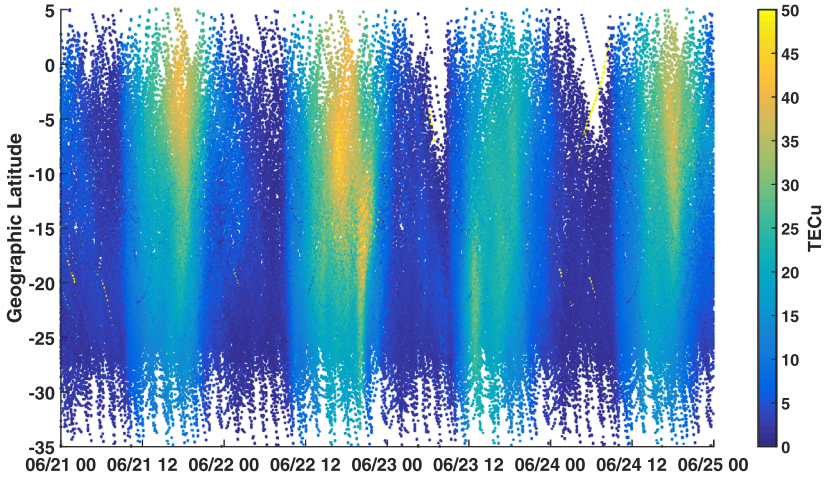

Figure 30 Vertical TEC in TEC units as a function of time and geographic latitude measured from 21 to 24 June 2015 between 35°S and 5°N. The considered longitudinal sector spans from 313°E to 318°E (Brazilian sector).

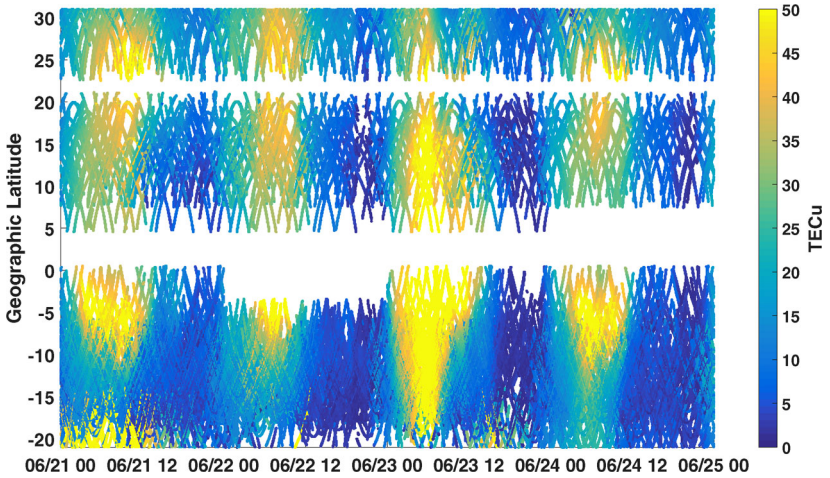

Figure 31 Vertical TEC in TEC units as a function of time and geographic latitude measured from 21 to 24 June 2015 between 20°S and 30°N. The considered longitudinal sector spans from 100°E to 115°E (Southeast Asian sector).

lifted up due to the eastward PPEFs; this, along with the photoionization of neutrals at lower altitudes, caused the recorded TEC increase. Conversely, the Brazilian local time sector that is located closer to the interplanetary shock is the nighttime sector, for which the PPEFs are westward and add up to the westward electric fields that are related to the ionospheric dynamo. According to Tsurutani *et al.* (2004), this means that for this sector the dayside region of 23 June cannot be affected by the significant uplift that has earlier (in local time) characterized the dayside region of the Southeast Asian sector, highlighting the dominant role of a disturbance dynamo westward electric field.

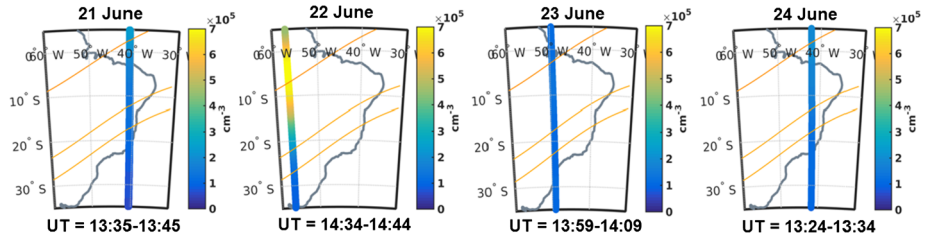

Figure 32 Electron density as measured by the *Swarm Alpha* satellite passing over the eastern part of South America during local morning of 21, 22, 23, and 24 June 2015.

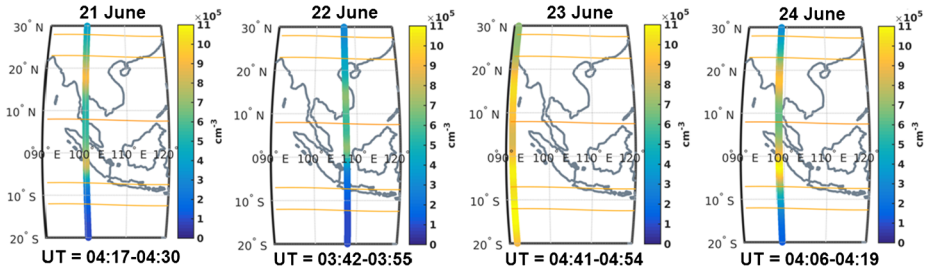

Figure 33 Same as Figure 30, but for the Southeast Asian sector.

For the intensification of the TEC that is visible in Figure 31 on 23 June, it is also indicative to point out the following two features: 1) the EIA presents an asymmetry (the southern crest is significantly larger than the northern one), which is likely the result of the prevailing quiet-time interhemispheric (summer-to-winter) winds that cause larger increases of electron densities in the winter hemisphere; 2) if compared with the previous and following days, the daytime TEC increase extends to the dusk sector, and as suggested by Tsurutani *et al.* (2004), this could result from a longitudinal extension to the dusk sector of the large dayside disturbance eastward electric field.

Figures 34 and 35 show the foF2 (top plots) and the h′F (bottom plots) as recorded by Cachoeira Paulista and Sanya ionosondes. After the interplanetary shock, Cachoeira Paulista, close to the southern crest of the EIA, is characterized by an uplift of the F layer that lasts about 12 hours. Cachoeira Paulista is located in the winter hemisphere, and according to Prölss (1995), this uplift can be attributed to both traveling atmospheric disturbances (TADs) and large-scale changes in the wind circulation, both of them caused by the significant amount of energy injected into the polar atmosphere. This long-duration upward drift is responsible for the foF2 increase that is well visible on 23 June and peaks at about 11 UT; on the other hand, this foF2 increase cannot be attributed to an intensification of the equatorial fountain effect, as is proved by the TEC map of Figure 30. Sanya, close to the northern crest of the EIA, presents a very different scenario. The h′F plot in the 24 hours following the interplanetary shock does not show any significant uplift, with the exception of an intensification of the pre-reversal enhancement (Woodman, 1970) in the evening of 23 June. The foF2 plot presents only a slight increase on 23 June, confirming the asymmetry of the EIA visible from the TEC map of Figure 31, showing an EIA with the southern crest more elongated in latitude than the northern one.

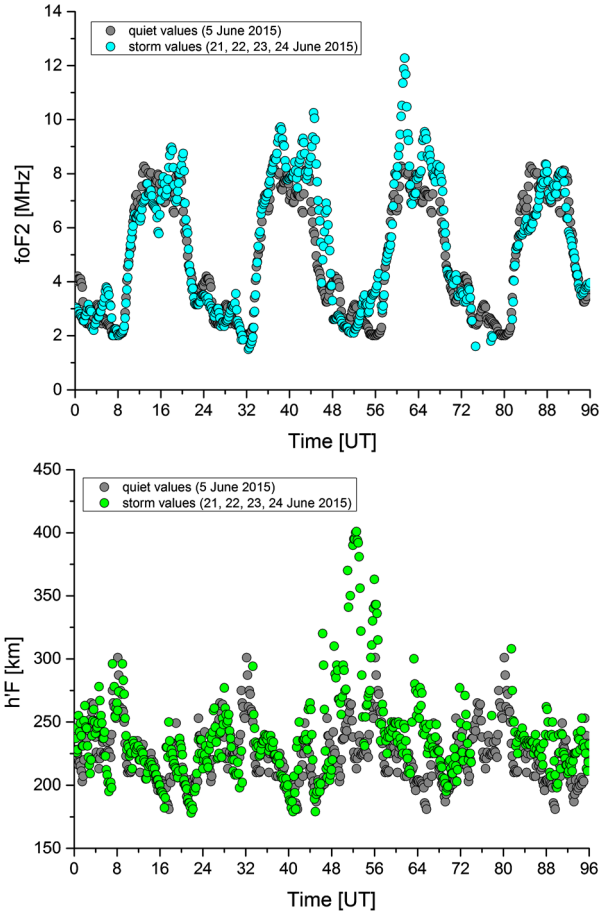

Figure 34 *Cyan full circles* correspond to the foF2 and *green full circles* to the h′F as measured at Cachoeira Paulista (22.7 S, 315.0 E) from 21 to 24 June 2015. *Gray full circles* in both plots represent values measured on 5 June 2015, which we here considered as the quiet reference day.

8.3. Ionospheric Polar Convection

In this subsection we present the observations of the ionospheric convection pattern as observed by SuperDARN in the northern polar ionosphere. This network consists of more than 30 high-frequency (8 – 20 MHz) coherent scatter radars that via the Doppler shift between the emitted and the reflected signal provide an estimation of the velocity of the ionospheric plasma convection over the polar regions. Furthermore, SuperDARN is also able to provide information on the features of the decameter-scale plasma irregularities in the E and F regions of the ionosphere (Chisham *et al.*, 2007).

To reconstruct the 2D ionospheric plasma flow, we make use of the representation developed by Ruohoniemi and Baker (1998) in terms of "potential maps". This representation combines the measurements from all the available SuperDARN radars with data from the statistical model by Ruohoniemi and Greenwald (1996) to yield a convection pattern covering the entire convection zone.

Figure 36 shows the increase of the ionospheric polar convection observed in the northern ionosphere during the occurrence of the SI. The SuperDARN radar back-scatter echoes are very few before the SI, but the measured velocity vectors are consistent with the two-cell convection pattern expected for a predominately negative $B_{y,\mathrm{IMF}}$, although the convection

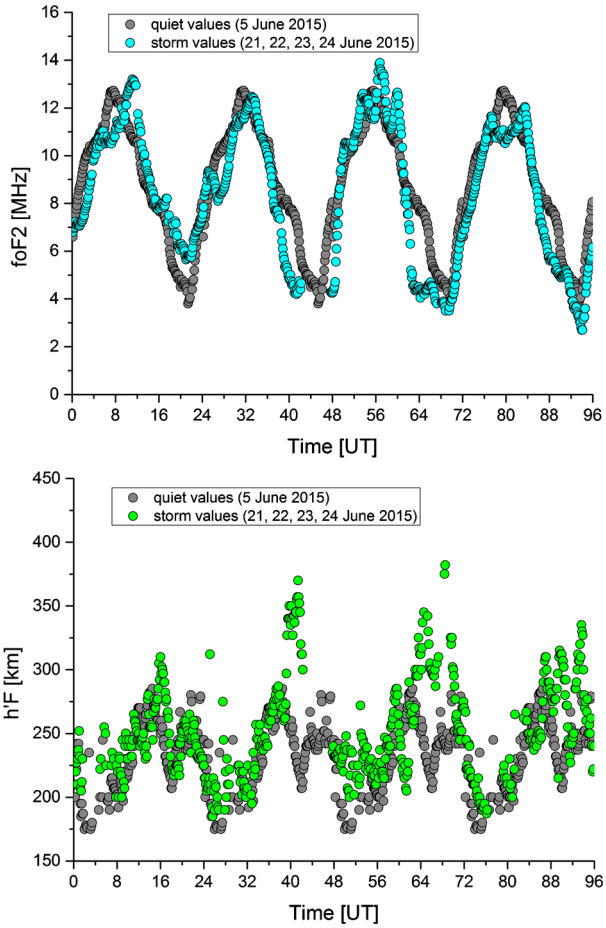

Figure 35 Same as Figure 34, but for the Sanya ionosonde (18.3 N, 109.4 E).

around 12 MLT (MLT being magnetic local time) is probably mainly determined by the statical model. At the time of the SI and in the following period, the two symmetric cells with the anti-sunward flow in the polar cap, which are characteristic of the predominately negative $B_{z,\mathrm{IMF}}$ convection pattern, show a large increase. In particular, the lower boundary of the convection region (the Heppner–Maynard boundary, the black–green dashed circle in the polar maps) shows an expansion toward low latitudes (from 60°N to 50°N). This boundary follows the expansion of the auroral oval in that regions. The increase in ionospheric polar convection is also clearly demonstrated by the increase in cross polar cap potential, Φ_{pc}, up to the very high value of 108 kV near the saturation limit (Shepherd, Greenwald, and Ruohoniemi, 2002).

Figure 37 shows the ionospheric convection pattern in proximity of the maximum level of the geomagnetic disturbance (SYM-H ~ -200 nT) occurring on 23 June at 04:27 UT. The SuperDARN radars back-scatter echoes are only present on the nightside around 24 MLT. The two convection cells reach low latitudes (~ 50°N) in the midnight sector, indicating a large expansion down to these latitudes of the auroral oval, as also shown by the profile of the Heppner–Maynard boundary.

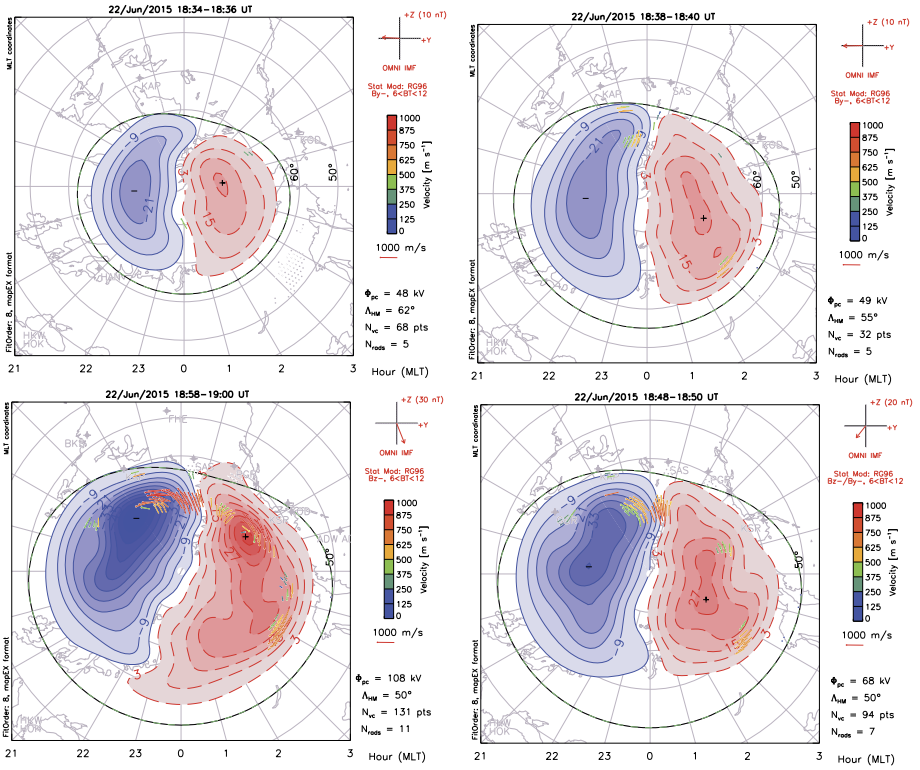

Figure 36 Evolution of the northern ionospheric polar convection pattern during the SI of 22 June from 18:34 UT to 19:00 UT. Images are shown in a clockwise sequence starting from the one at the *top left*.

During the recovery phase, the two-cell convection structure shrinks (see, *e.g.*, Figure 38) and the entire auroral oval contracts to high-latitude regions ($\lambda_g > 60°$N). This also implies a strong reduction of the polar cap potential toward low values (few kV). These effects are very well visible in Figure 38, which shows a characteristic situation during the late recovery phase.

9. Ground-Based Magnetic Response

In this section, we describe the ground effects of the impact of the solar ejecta. During the main phase of a geomagnetic storm, several phenomena can be detected by ground stations that reflect into variations of both the magnetospheric and ionospheric currents. In particular, after a brief introduction to the general features of the ground response as measured by SYM-H and AE indices, we evaluate the ionospheric currents generated during the SI occurrence and the long-timescale contribution of the geomagnetic field as a function of the latitude of the observatory.

9.1. General Features

In Figure 23i we report the high-latitude geomagnetic AE index (Davis and Sugiura, 1966), which is an indirect measure of the energy deposition rate in the polar ionosphere (Ahn, Aka-

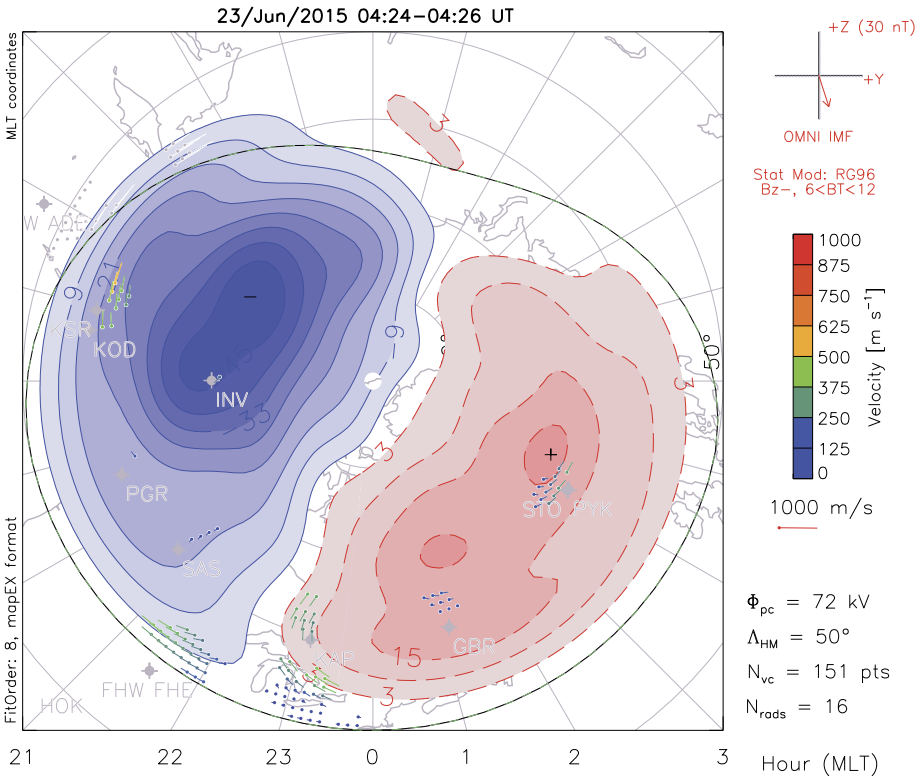

Figure 37 Ionospheric polar convection pattern near the minimum of SYM-H on 23 June at 04:25 UT as reconstructed from SuperDARN. The *green–black dashed curve* is the Heppner–Maynard boundary.

sofu, and Kamide, 1983), and the low-latitude geomagnetic SYM-H index (Figure 23h). The geomagnetic response is compared to the SW variations observed by the *Wind* spacecraft.

A simple visual inspection of the data reported in Figure 23 shows that the observed high-latitude and low-latitude geomagnetic response during the investigated time period is highly complex. On 22 June at 18:37 UT, SYM-H shows a large increase (SI) up to 88 nT, which follows the increase of the solar wind flow velocity, v, and proton density, n_p, observed by *Wind* at 18:07 UT (Figure 23a). According to Joselyn and Tsurutani (1990), this increase can be considered as the SI of the GS occurring on 22 June. The structure of the GS suggests that this is a double storm. Indeed, after the first rapid decrease of the SYM-H value down to -139 nT at 20:17 UT, we observe another large negative peak (SYM-H $= -208$ nT) on 23 June at 04:27 UT. This double structure resembles the trend of the $B_{z,\mathrm{IMF}}$ component, which shows two periods of nearly stable time intervals of $B_{z,\mathrm{IMF}} < 0$: the first starts at 17:43 UT of 22 June and the second at 01:22 UT of 23 June. The first period is clearly related to the negative $B_{z,\mathrm{IMF}}$ carried by the sheath of the ejecta following the shock arrival (Tsurutani *et al.*, 1988; Smith, Tsurutani, and Rosenberg, 1978). The second is related to the negative $B_{z,\mathrm{IMF}}$ carried by the first magnetic cloud or flux rope (Burlaga *et al.*, 1981; Liu *et al.*, 2015). As a consequence of these long intervals of negative $B_{z,\mathrm{IMF}}$, the solar wind plasma can flow inside the Earth's magnetosphere due to the possible occurrence of magnetic reconnection at the Earth's magnetopause between the IMF and Earth's magnetic field. At high latitude, the

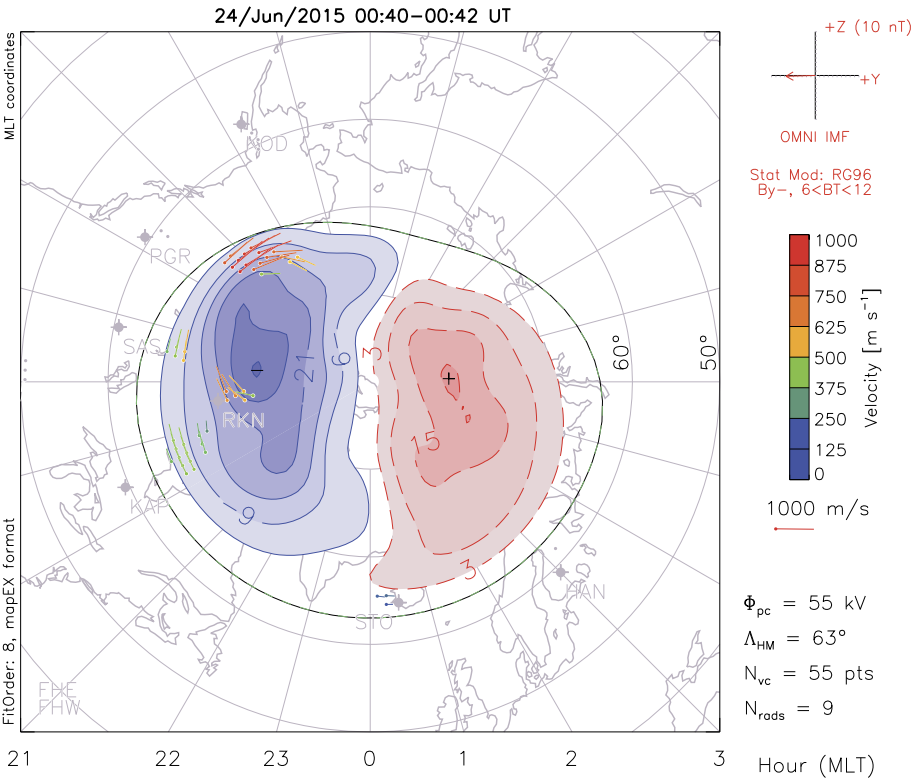

Figure 38 Ionospheric polar convection pattern at the end of the recovery phase on 25 June at 00:03 UT. The *green–black dashed curve* is the Heppner–Maynard boundary.

geomagnetic activity is characterized by large bursts of activity, as is clearly shown by the AE index. This is the evidence of a series of fast-relaxation events, perhaps a consequence of an activity in the near-Earth geomagnetic tail regions, which are due to the occurrence of a series of loading and unloading energy releases (Kamide and Kokubun, 1996; Consolini and De Michelis, 2005). The activity of the AE index resembles the changes of SYM-H with time quite well. The first AE index burst is quite well correlated with the SI. This correlation suggests that this AE enhancement is directly driven by the interplanetary shock because it also occurs in the case of northward IMF quiescent substorms (Zhou and Tsurutani, 2001; Lyu, 2002; Tsurutani and Zhou, 2003). The successive peaks occur in phase with the decreasing of SYM-H, suggesting that these can be the consequence of the overall magnetospheric activity and of what is named "storm-substorm relationship". Furthermore, the high-latitude geomagnetic activity also continues during the first stage of the storm recovery phase. This successive AE-index activity is very well correlated with the successive negative turnings of the $B_{z,\mathrm{IMF}}$ (green shaded regions in Figure 23) that occurs on 23 June after 10:00 UT and was interpreted as two magnetic clouds or flux ropes by Liu *et al.* (2015). However, these successive turnings of $B_{z,\mathrm{IMF}}$ do not affect the recovery phase because they are correlated with a time interval during which the solar wind density decreases to values below $n_\mathrm{p} = 1\ \mathrm{cm}^{-3}$.

9.2. The SI Characteristics and the Ionospheric Current Flow Pattern

Generally, the main phase of a GS is preceded by the SI, caused by interplanetary fast shocks or discontinuities of the incoming solar wind (SW) that collides with the magnetopause and compresses the magnetosphere. The morphological aspects of SIs at a geosynchronous orbit and in the outer magnetosphere have been studied in several works (Patel and Coleman, 1970; Kokubun, 1983; Lee and Lyons, 2004; Villante and Piersanti, 2008, 2009; Piersanti *et al.*, 2012). At a geosynchronous orbit, they show that the SI amplitude was remarkably dependent on LT, with highest values at noon and very low values (or even negative, in some cases) in the night sector. On the other hand, at the ground, the SI signature shows a more complex behavior, depending upon LT and geomagnetic latitude. The current understanding suggests that the total disturbance field (D_{SI}) can be decomposed into different subfields, namely $D_{SI} = DL + DP$ (Araki, 1994). They consist of a step-like structure of magnetospheric origin that is dominant at low latitudes (DL field, where L stands for low latitude) and a double-pulse structure of ionospheric origin (DP field, where P stands for polar latitude) that is dominant at high latitudes; the first and the second pulse are called preliminary impulse (PI) and main impulse (MI), respectively.

Araki (1994) developed a model to explain the global behavior of the SI waveform, considering the horizontal component (H) of the geomagnetic field (north–south) alone. According to this model, the SW pressure enhancement increases the magnetopause current that generates a step-like increase, with maximum amplitude at the equator. Two-cell ionospheric currents (DP, two-type currents), induced by a dusk-to-dawn electric field along the compressional wavefront, produce a preliminary impulse of polar origin (PI). On the other hand, if the SW dynamic pressure persists high, the magnetospheric convection adjusts itself to the compressed state, determining a new ionospheric vortex system (opposite to the PI), corresponding to the main impulse (MI). It is driven by the electric field that originates in the polar region and is transmitted from the outer magnetosphere through field-aligned currents (FAC), which flow into the ionosphere on the morning side and away on the afternoon side. The amplitude and waveform of the magnetic field variation strongly depend on latitude and LT (Araki, 1994; Piersanti and Villante, 2016; Carter *et al.*, 2016). At low latitudes, the DP field is characterized by a positive variation along the H component, whose amplitude maximizes around local noon, and by a negligible or null variation along the east–west component (D). Araki, Tsunomura, and Kikuchi (2009) showed that both PI and MI fields are produced by a combination of FACs and ionospheric currents (IC), so that

$$\begin{aligned} DP &= PI + MI, \\ PI &= PI_{FAC} + PI_{IC}, \\ MI &= MI_{FAC} + MI_{IC}. \end{aligned}$$

Recently, Piersanti and Villante (2016) developed a technique to distinguish between the DL and the DP fields from ground SI observations, inferring double ionospheric current vortices for both the PI and the MI. They estimated the DL field by comparing the magnetospheric field observations and predictions from the model of Tsyganenko and Sitnov (2005). The DP field is obtained by subtracting the estimated DL field from ground observations.

Here, we applied the Piersanti and Villante (2016) technique to 63 ground magnetic observatories in the northern hemisphere to derive the ionospheric current flow pattern associated with the 22 June 2015 SI. For this purpose, we used the *International Real-time Magnetic Observatory Network* (INTERMAGNET, http://www.intermagnet.org/index-eng.php)

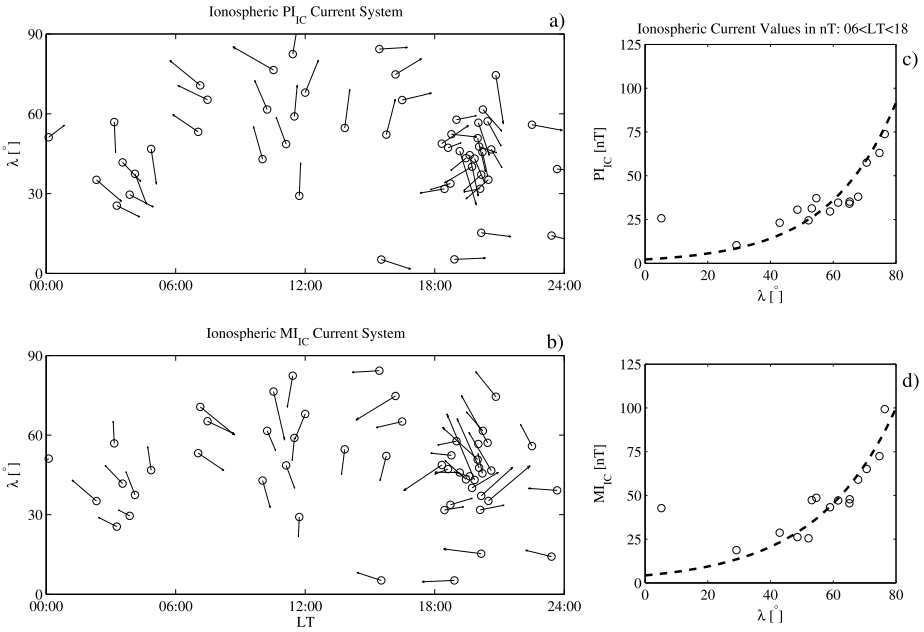

Figure 39 (**a**) and (**b**): Direction of the ionospheric currents for the PI_{IC} panel **a**) and for the MI_{IC} panel **b**) as a function of latitude and local time after a 90° rotation of the disturbance magnetic field. (**c**) and (**d**): Characteristics of the PI_{IC} panel **c**) and MI_{IC} panel **d**) amplitude fields as a function of latitude in the dayside sector ($06 < LT < 18$); *dashed lines* represent the exponential fits, and *black circles* represent the morning PI_{IC} and MI_{IC}.

global network of observatories for ground measurements and the *Van Allen* probes (formerly known as the *Radiation Belt Storm Probes*, RBSP-A and RBSP-B) data for magnetospheric observations. On the basis of the Piersanti and Villante (2016) scheme, we compared both RBSP-A and RBSP-B magnetospheric field data with the TS04 (Tsyganenko and Sitnov, 2005) predictions for different magnetospheric current configurations (not shown), obtaining that the sum of the Chapman–Ferraro current and the tail current (B_{CF+T}) provides the best representation of the magnetospheric response to the SI disturbance. This result, at the ground, allows us to estimate the DL field by means of the B_{CF+T} field along both the H and the D components. The residual DP fields is determined by subtracting the estimated DL_H and DL_D fields from ground magnetic observations.

On the basis of the results obtained for the DP fields, we evaluated the ionospheric origin fields (PI_{IC} and MI_{IC}) at each ground station. The global results for PI_{IC} and MI_{IC} vectors, as obtained at 63 ground stations, are summarized in Figure 39, which shows the direction of the ionospheric current for the PI_{IC} (Figure 39a) and the MI_{IC} (Figure 39b). The behavior is consistent with a morning counter-clockwise (CCW) and an afternoon clockwise vortices (CW) for the PI_{IC} and a morning CW and an afternoon CCW vortices for the MI_{IC}, respectively. The focus for each vortex results to be approximately located at $\lambda \sim 58°$ and LT ∼ 06:30 and at $\lambda \sim 58°$ and LT ∼ 17:00. Lower latitude stations show almost horizontal directions (west–east for the PI_{IC} and east–west MI_{IC}), as expected for the equatorial SI ionospheric circulation. These results are in agreement with Araki (1994) and with Piersanti and Villante (2016). Figure 39c and d show the amplitude of the PI_{IC} and MI_{IC} fields *vs.* latitude in the dayside sector ($06 < LT < 18$). In agreement with Piersanti and Villante (2016), both

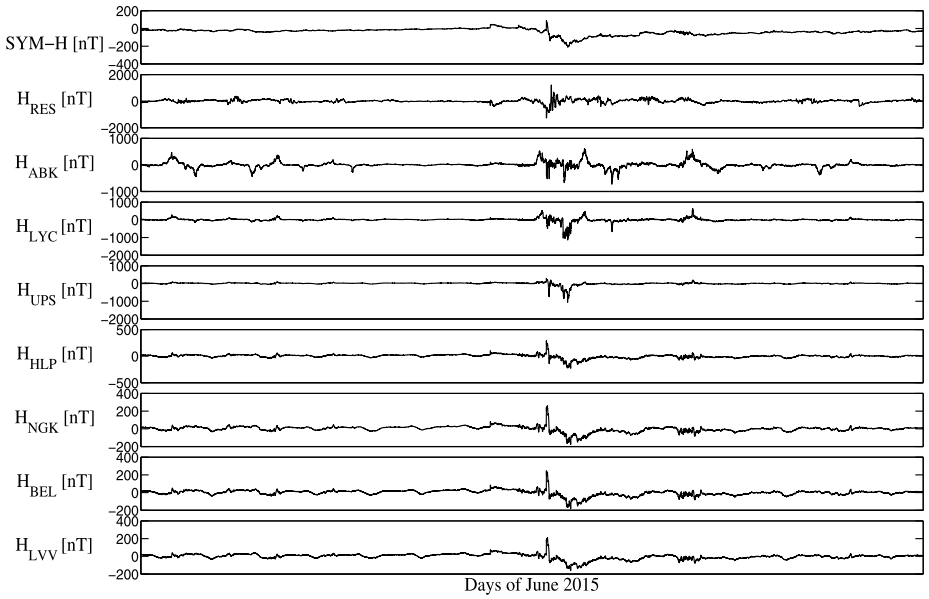

Figure 40 *From top to bottom*: SYM-H index and H component measured at each geomagnetic observatory (with decreasing latitude). The horizontal axis extends from 15 to 30 June.

PI_{IC} and MI_{IC} field amplitudes increase with latitude, and the experimental points can be approximated by an exponential function (black dashed lines), such as $PI_{IC}(\lambda) = PI_0 \cdot e^{A \cdot \lambda}$, $MI_{IC}(\lambda) = MI_0 \cdot e^{B \cdot \lambda}$, with $PI_0 = 2.19$ nT, $A = 0.06^{\circ -1}$, and $MI_0 = 5.25$ nT, $B = 0.10^{\circ -1}$. Here, PI_0 and MI_0 are the PI_{IC} and MI_{IC} amplitude inferred at the equator ($\lambda = 0^{\circ}$). The outliers at lower latitudes might be related to the equatorial electrojet and could be used as an estimate of its strength.

9.3. Baseline Response

For our analysis, we used 1-minute data from the horizontal component of the geomagnetic field (H) measured at permanent geomagnetic observatories distributed in the northern hemisphere from mid-latitude to high-latitude, obtained from INTERMAGNET as shown in Figure 40.

The data were collected from eight permanent geomagnetic observatories as reported in Table 3 during the period 15 – 30 June 2015. To study the large-timescale variations of the geomagnetic field during the occurrence of a geomagnetic storm, we used the Alberti *et al.* (2016) method for the identification of the different magnetic field contributions during a geomagnetic storm via the empirical mode decomposition (EMD) technique (Huang *et al.*, 1998; Alberti *et al.*, 2017b). An example of the EMD results is reported in Figure 41, where the decomposition is applied to the high-latitude Resolute Bay (RES) time series and to the low-latitude Lviv (LVV) record, respectively.

In this way, we extracted the intrinsic timescale components of each time series, ranging from a few minutes to days. Typically, processes on short timescales (≤ 24 hours) are involved in the magnetosphere–ionosphere coupling and produce effects on the ground through the current systems flowing in the ionospheric region and in the Earth's upper mantle (Feldstein and Zaitzev, 1968; Dominici, Cander, and Zolesi, 1997; De Michelis, Tozzi,

Table 3 List of geomagnetic observatories.

Station name	IAGA code	Geographic latitude (λ_g)	Geographic longitude (ϕ_g)
Lviv	LVV	49.90 N	23.75 E
Belsk	BEL	51.83 N	20.80 E
Niemegk	NGK	52.07 N	12.68 E
Hel	HLP	54.60 N	18.82 E
Uppsala	UPS	59.90 N	17.35 E
Lycksele	LYC	64.06 N	18.07 E
Abisko	ABK	68.36 N	18.82 E
Resolute Bay	RES	74.70 N	26.10 E

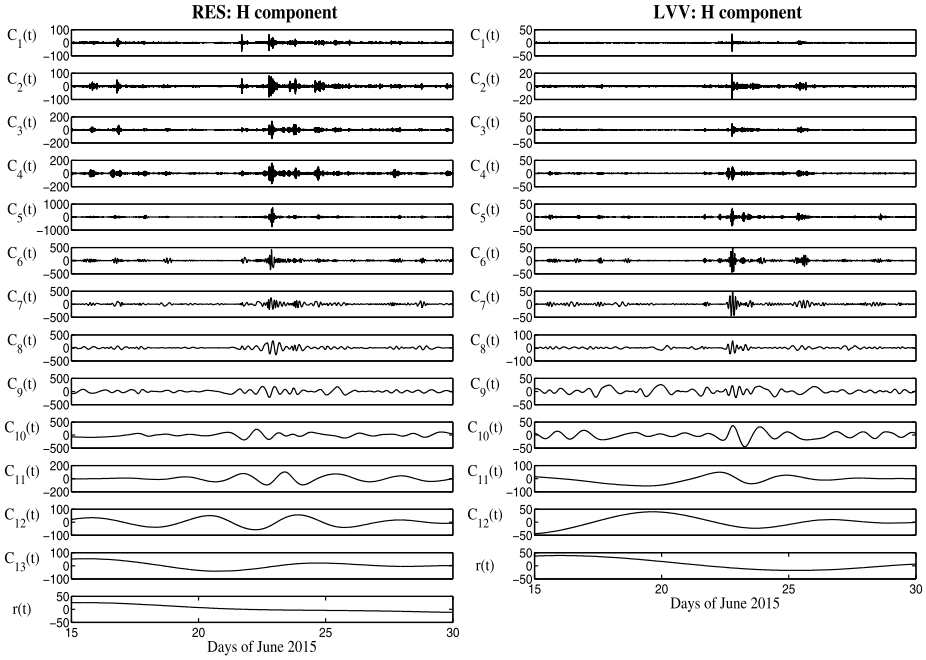

Figure 41 EMD results from the H component measured at the RES (*left panels*) and LVV (*right panels*) geomagnetic stations, respectively. In each column, the vertical axes, C_i, correspond to the EMD components from highest to lower frequency.

and Consolini, 2010). Conversely, long-timescale processes (> 24 hours) are related to the direct contribution of the geomagnetic field variations, which we identified as the baseline component of the time series. For these reasons, we divided each set of modes into two different subsets: the short-timescale component, which involves empirical modes with a characteristic timescale shorter than 24 hours, and long-timescale components (named H_0), characterized by intrinsic oscillations on timescales greater than 24 hours. Here, we are particularly interested in the study of the long-timescale components because they can be used as a measure of the geomagnetic response to solar wind changes, related to the ring current and equatorial electrojet activities. Indeed, several low-latitude geomagnetic indices

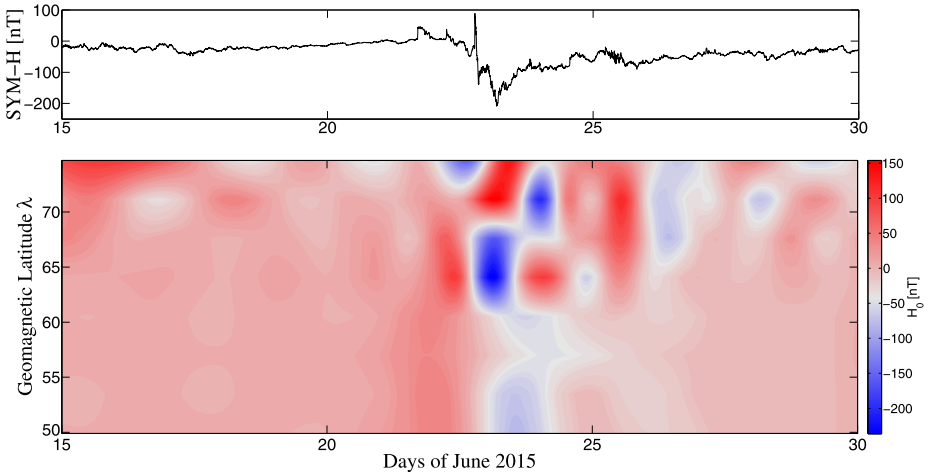

Figure 42 *Top panel*: Time behavior of the SYM-H index during the time period under investigation. *Bottom panel*: Time-latitude behavior of the baseline extracted via the EMD procedure from each geomagnetic station.

(*i.e.* SYM-H, ASY-H, and Dst) have been proposed to monitor changes in the equatorial current systems (*e.g.* ring current and equatorial electrojet). Particularly, the SYM-H index is determined by the geomagnetic H component derived from six near-equatorial ground magnetometers that are unevenly distributed in longitude and latitude, far from the auroral oval region to eliminate the effects of the ionospheric auroral electrojets (Gonzalez *et al.*, 1994; Wanliss and Showalter, 2006). It is calculated by removing the geomagnetic main field and the quiet solar daily variation from the observed magnetometer data by transforming it into a dipole coordinate system and finally by evaluating the weighted average over the six stations of the deviation of the H component from a quiet day (with a weighting factor that is the reciprocal of the cosine of the magnetic latitude of each station). In this way, it represents the average disturbance of the H component that is thought to be symmetric about Earth, and which is generally attributed to the symmetric ring current activity. For these reasons, since the long-timescale component extracted *via* the EMD procedure does not contain any oscillation with a characteristic timescale lower than one day (for example, a signature of the ionospheric solar quiet variation), it is similar to the SYM-H, index but it can be evaluated for each station (not only for equatorial stations) and can be used as a local measure of the time-dependent geomagnetic average field.

Figure 42 shows the time-latitude behavior of the baselines H_0 obtained from EMD reconstructions and the time behavior of the SYM-H index.

As shown in Figure 42, the intensity of the baseline increases with latitude for each day, indicating that large-amplitude fluctuations are more pronounced in the auroral region, which is particularly evident during the geomagnetic storm (22 – 23 June 2015). This suggests that the long-timescale field, which is free of short-timescale contributions related to the internal dynamics of the magnetosphere and to the ionospheric effects, follows the solar wind driver that impacts the magnetosphere. Indeed, by a comparison with the SYM-H index, we note that the time behavior of the baseline is similar to the SYM-H index time-evolution, but with different polarity patterns, according to the different latitude considered. Particularly, in the high-latitude region (from geomagnetic latitudes $\geq 70°$), the baseline behavior is different from the mid-latitude one. While mid-latitude baselines follow

the time behavior of the SYM-H index with a time shift when the latitude decreases (as a consequence of the effects of the perturbation at different latitudes), high-latitude baselines present an opposite time-behavior with respect to the SYM-H index. This could be related to the different current systems encountered by the perturbation when it propagates from high to mid-latitudes.

10. Summary and Conclusions

The solar trigger of the halo CME was a violent energy release that occurred in the δ complex of AR NOAA 12371. Two subsequent M2.0 and M2.6 flares took place in this region. The X-ray emission showed no interruption, so that these flares can be considered a unique event. The plasma dynamics along the PIL exhibited long-lasting upflows and downflows, suggesting shear accumulation in this location. The flares involved a large area, as shown in EUV images. The events evolved through the destabilization of several coronal structures, in a manner reminiscent of a domino effect. The analysis of the shear angle, the gradient of the vertical magnetic field, and the electric currents indicates that an energy storage mechanism, compatible with shear accumulation, was active before the eruption. After the flares, the region of the δ complex achieved a more relaxed state.

The comparison between the EUV observations of SDO/AIA and the force-free extrapolation allowed us to determine a negative value of the force-free parameter (α) for the magnetic system involved in the solar eruption. The negative value of α corresponds to a flux rope characterized by negative helicity, which is usually associated with a left-handed magnetic cloud. Moreover, from the full-disk extrapolated magnetic field using the PFSS model, we found several open magnetic field lines around NOAA 12371 that were directed toward Earth. The peculiar location of AR NOAA 12371, surrounded by open field, is an interesting setting for any space weather prediction model.

The availability of polarized images acquired exactly at the time of the transit of the halo-CME front in the LASCO-C2 FOV allowed us to perform a 3D reconstruction of the eruption with the polarization ratio technique. Results show that the plasma is expanding almost homogeneously at all latitudes, but with a prominent inclination with respect to the POS around 25°. This allowed us to derive a deprojected CME front speed which, due to CME deceleration, is quite small at large distances (330 km s^{-1} at $\simeq 27.6 R_{sun}$). The application of a simple 1D drag-based model for the interplanetary CME propagation led us to conclude that the early arrival time observed by ACE at 1 AU can be reproduced only by assuming an average propagation speed of about 1440 km s^{-1}, much higher than the estimated deprojected CME front speed.

An SEP event was observed on 21 June 2015, which can be associated with the M2.6 flare (peak time on 21 June at 02:36 UT) that occurred in AR 12371, located at N13 W00, and the concomitant full-halo CME at 02:36 UT. This SEP event was also accompanied by Type II and Type IV radio bursts, indicating the presence of a propagating interplanetary shock, and Type III radio signatures. The observed proton fluxes at all of the energy channels up to 80 MeV show a gradual rise in the prompt phase (as expected for a central meridian event); at > 10 MeV the maximum value was 1070 pfu. This flux level corresponds to a "strong" radiation storm (as classified by the NOAA space weather center), producing biological, space operation, and high frequency (HF) propagation impacts. Using the ESPERTA model developed by Laurenza *et al.* (2009), we were able to forecast the 21 June 2015 SEP event at 02.46 UT (10 min after the SXR peak), with a warning time of ~ 19 hours before its actual occurrence.

A remarkable interplanetary shock, characterized by high values of the solar wind dynamic pressure and of the southward component of the IMF, was observed by *Wind* at 18:07 UT on 22 June 2015. The associated ICME produced a noticeable Forbush decrease in the cosmic-ray intensity of about 5% at rigidity ≥ 6.27 GV, as observed in the Rome neutron monitor (SVIRCO Observatory) records. The magnetospheric response to the shock arrival (18:33 UT) is characterized by a relevant erosion of the magnetospheric field caused by the strong southward component of B_{IMF} observed in the corresponding interval.

The plasmasphere dynamics shows a first significant erosion up to $\sim 2.5\ R_{\mathrm{E}}$ on 24 June. Most of the plasma loss was presumably due to a strong electric field convection toward the dayside magnetopause during 23 June. An almost complete recovery (at least up to $\sim 4\ R_{\mathrm{E}}$) was observed on the morning of the next day (25 June). A similar (or even stronger) plasmasphere depletion (density decrease of a factor ~ 10 at 5.5 R_{E}) was observed on 26 June in correspondence with a new magnetospheric disturbance occurring on 25 June. In this case, the subsequent plasmasphere recovery appeared to be much slower than in the first case and more in line with previous observations (Park, 1974; Chi *et al.*, 2000). The results demonstrate that the FLR-technique is indeed a very powerful method for monitoring the dynamics of the plasmasphere. However, the typical lack of FLR signatures during the nighttime does not allow us to completely follow all phases of the geomagnetic storm. A larger longitudinally extended network would be necessary to obtain a more complete picture of the plasmaspheric dynamics during such events.

On 22 June at 18:37 UT, SYM-H shows a large SI (up to 88 nT) that precedes the geomagnetic storm occurring on 22 June, due to the 21 June ICME. The SI is characterized by a double-pulse structure ($\mathrm{PI_{IC}}$ and $\mathrm{MI_{IC}}$) whose amplitude and wave forms depend on the latitude and local time of the observatories. Both $\mathrm{PI_{IC}}$ and $\mathrm{MI_{IC}}$ produced twin ionospheric current vortices that completely modified the quiet ionospheric current pattern. We found that the behavior of the ionospheric current associated with the 22 June SI is consistent with a morning counter-clockwise (CCW) and an afternoon clockwise (CW) vortices for the $\mathrm{PI_{IC}}$ and a morning CW and an afternoon CCW vortices for the $\mathrm{MI_{IC}}$, respectively. The focus for each vortex to be approximately located at $\lambda \sim 58°$ and LT $\sim$ 06:30 and at $\lambda \sim 58°$ and LT $\sim$ 17:00. Lower latitude stations show almost horizontal directions (west–east for the $\mathrm{PI_{IC}}$ and east–west $\mathrm{MI_{IC}}$), as expected for the equatorial SI ionospheric circulation. These results are in agreement with Araki (1994) and Piersanti and Villante (2016). Moreover, the ionospheric convection pattern as observed by SuperDARN in the northern polar ionosphere is characterized by the well-known two-cells structure, with the antisunward flow in the polar cap (typical of the predominately negative $B_{z,\mathrm{IMF}}$), which shows a large increase during and after the SI. In particular, the lower boundary of the convection region (the Heppner–Maynard boundary, the black–green dashed circle in the polar maps) shows an expansion toward low latitudes (from $\lambda_g = 60°$N to $\lambda_g = 50°$N), especially in the midnight sector. This boundary follows the expansion of the auroral oval in these regions. The increase in ionospheric polar convection is also clearly demonstrated by the increase in polar cap potential, Φ_{pc}, up to 108 kV.

The low-latitude ionospheric response to the GS shows different behavior in different local time sectors. While the Brazilian sector is characterized by a suppression of the EIA, the Southeast Asian sector shows an intensification of the EIA crest. This would suggest that in the Southeast Asian sector, the eastward PPEFs caused an intensification of the daytime equatorial ionospheric dynamo eastward electric field, with a consequent intensification of the fountain effect at the base of the EIA; in the Brazilian sector the situation is instead reversed, with a significant weakening of this electric field and a dominant role of a disturbance dynamo westward electric field. Furthermore, the ionosonde data analysis suggests

that the travelling atmospheric disturbance (TAD) propagation and large-scale changes in the wind circulation also affected the low-latitude ionospheric dynamics.

In addition, applying the empirical mode decomposition technique (Huang *et al.*, 1998) on data collected from eight permanent geomagnetic observatories, we studied the long-timescale variations of the geomagnetic field during the occurrence of the geomagnetic storm. We identified two characteristic timescale ranges of variability:

i) processes on short timescales (≤ 24 hours) that are involved in the magnetosphere–ionosphere coupling, producing ground effects through the current systems flowing in the ionospheric region and in the Earth's upper mantle (Feldstein and Zaitzev, 1968; Dominici, Cander, and Zolesi, 1997; De Michelis, Tozzi, and Consolini, 2010)
ii) long-timescale processes (baseline, > 24 hours) that we related to the direct contribution of the geomagnetic field variations (baseline component).

We found that the baseline increases with latitude, suggesting that the long-timescale field, which is free of short-timescale contributions related to the internal dynamics of the magnetosphere and to the ionospheric effects, follows the solar wind driver that impacts the magnetosphere. Moreover, by a comparison between the SYM-H index and the baselines, we note that their time behavior is similar, but with different polarity patterns depending on the different latitude considered.

Interestingly, observations of the ionospheric convection pattern from SuperDARN in the northern polar ionosphere during the maximum level of geomagnetic disturbance (SYM-H ~ -200 nT) shows two convection cells that reach low latitudes ($\sim 50^\circ$ N) in the midnight sector, indicating a large expansion down to these latitudes of the auroral oval, as also shown by the profile of the Heppner–Maynard boundary. On the other hand, the same observations, made during the recovery phase of the geomagnetic storm, show a shrinking of the two-cell convection structure and a contraction of the entire auroral oval to higher latitudes ($\lambda_g > 65^\circ$N). This also implies a strong reduction of the polar cap potential toward low values (a few kV).

As far as we know, this article represents the first attempt to provide a comprehensive analysis of the different aspects of a solar and interplanetary event, from its appearance in the solar atmosphere to the manifestation of the related disturbances in the Earth's environment. Although several features still deserve further analysis (in particular, those related to the development, evolution, and configuration of the magnetospheric and ionospheric current systems), similar analyses are important in the space weather context for a better understanding of the aspects that determine the geoeffectiveness of solar activity manifestations.

Acknowledgements The results presented in this paper rely on data collected at magnetic observatories. We thank the national institutes that support them and INTERMAGNET for promoting high standards of magnetic observatory practice (www.intermagnet.org). We thank the entire PAMELA Collaboration for the data used in this research. This work is supported by the Italian National Program for Antarctic Research (PNRA) Research Project 2013/AC3.08. We thank the national scientific funding agencies of Australia, Canada, China, France, Italy, Japan, South Africa, UK, and USA that funded the radars of the SuperDARN network. The authors also acknowledge the use of the SuperDARN software and web tools made available at Virginia Tech. The authors kindly acknowledge N. Papitashvili and J. King at the National Space Science Data Center of the Goddard Space Flight Center for the use permission of 1-minute OMNI data and the NASA CDAWeb team for making these data available. The Rome neutron monitor (SVIRCO Observatory) is supported by the IAPS/INAF-UNIRoma3 collaboration. This research work is supported by the Italian MIUR-PRIN grant 2012P2HRCR on *The active Sun and its effects on Space and Earth climate*

References

Aarons, J.: 1991, The role of the ring current in the generation or inhibition of equatorial f layer irregularities during magnetic storms. *Radio Sci.* **26**(4), 1131. DOI.

Adriani, O., Barbarino, G.C., Bazilevskaya, G.A., Bellotti, R., Boezio, M., Bogomolov, E.A., *et al.*: 2011, Observations of the 2006 December 13 and 14 solar particle events in the 80 MeV n^{-1} – 3 GeV n^{-1} range from space with the PAMELA detector. *Astrophys. J.* **742**, 102. DOI. ADS.

Adriani, O., *et al.*: 2014, The PAMELA mission: heralding a new era in precision cosmic ray physics. *Phys. Rep.* **544**, 323. DOI. ADS.

Ahn, B.-H., Akasofu, S.-I., Kamide, Y.: 1983, The Joule heat production rate and the particle energy injection rate as a function of the geomagnetic indices ae and al. *J. Geophys. Res., Space* **88**(A8), 6275. DOI.

Alberti, T., Piersanti, M., Vecchio, A., De Michelis, P., Lepreti, F., Carbone, V., Primavera, L.: 2016, Identification of the different magnetic field contributions during a geomagnetic storm in magnetospheric and ground observations. *Ann. Geophys.* **34**(11), 1069. DOI.

Alberti, T., Laurenza, M., Cliver, E., Storini, M., Consolini, G., Lepreti, F.: 2017a, Solar activity from 2006 to 2014 and short-term forecasts of solar proton events using the "esperta" model. *Astrophys. J.* **838**, 59. DOI.

Alberti, T., Consolini, G., Lepreti, F., Laurenza, M., Vecchio, A., Carbone, V.: 2017b, Timescale separation in the solar wind-magnetosphere coupling during St. Patrick's Day storms in 2013 and 2015. *J. Geophys. Res.* **122**(4), 4266. DOI.

Alfonsi, L., Spogli, L., Pezzopane, M., Romano, V., Zuccheretti, E., De Franceschi, G., Cabrera, M., Ezquer, R.: 2013, Comparative analysis of spread-f signature and gps scintillation occurrences at Tucumán, Argentina. *J. Geophys. Res.* **118**(7), 4483. DOI.

Alissandrakis, C.: 1981, On the computation of constant alpha force-free magnetic field. *Astron. Astrophys.* **100**, 197.

Araki, T.: 1994, A physical model of the geomagnetic sudden commencement. In: *Geoph. Monog.* **81**, AGU, Washington, 183.

Araki, T., Tsunomura, S., Kikuchi, T.: 2009, Local time variation of the amplitude of geomagnetic sudden commencements (sc) and sc-associated polar cap potential. *Earth Planets Space* **61**(4), e13. DOI.

Aschwanden, M.J.: 2002, Particle acceleration and kinematics in solar flares – a synthesis of recent observations and theoretical concepts. *Space Sci. Rev.* **101**(1–2), 1. DOI.

Astafyeva, E., Zakharenkova, I., Patrick, A.: 2016, Prompt penetration electric fields and the extreme topside ionospheric response to the June 22 – 23, 2015 geomagnetic storm as seen by the Swarm constellation. *Earth Planets Space* **68**(1), 152. DOI.

Baker, D.N., Jaynes, A., Kanekal, S., Foster, J., Erickson, P., Fennell, J., Blake, J., Zhao, H., Li, X., Elkington, S., *et al.*: 2016a, Highly relativistic radiation belt electron acceleration, transport, and loss: large solar storm events of March and June 2015. *J. Geophys. Res.* **121**(7), 6647. DOI.

Baker, D., Jaynes, A., Turner, D., Nakamura, R., Schmid, D., Mauk, B., Cohen, I., Fennell, J., Blake, J., Strangeway, R., *et al.*: 2016b, A telescopic and microscopic examination of acceleration in the June 2015 geomagnetic storm: magnetospheric multiscale and van Allen probes study of substorm particle injection. *Geophys. Res. Lett.* **43**(12), 6051. DOI.

Balan, N., Shiokawa, K., Otsuka, Y., Kikuchi, T., Vijaya Lekshmi, D., Kawamura, S., Yamamoto, M., Bailey, G.: 2010, A physical mechanism of positive ionospheric storms at low latitudes and midlatitudes. *J. Geophys. Res.* **115**(A2). DOI.

Baransky, L., Borovkov, J., Gokhberg, M., Krylov, S., Troitskaya, V.: 1985, High resolution method of direct measurement of the magnetic field lines' eigen frequencies. *Planet. Space Sci.* **33**(12), 1369. DOI.

Bemporad, A., Pagano, P.: 2015, Uncertainties in polarimetric 3D reconstructions of coronal mass ejections. *Astron. Astrophys.* **576**, A93. DOI. ADS.

Berube, D., Moldwin, M.B., Ahn, M.: 2006, Computing magnetospheric mass density from field line resonances in a realistic magnetic field geometry. *J. Geophys. Res., Space* **111**(A8), A08206. DOI.

Bibl, K., Reinisch, B.W.: 1978, The universal digital ionosonde. *Radio Sci.* **13**(3), 519. DOI.

Blake, J.B., Kolasinski, W.A., Fillius, R.W., Mullen, E.G.: 1992, Injection of electrons and protons with energies of tens of mev into l < 3 on 24 March 1991. *Geophys. Res. Lett.* **19**(8), 821. DOI.

Blanc, M., Richmond, A.: 1980, The ionospheric disturbance dynamo. *J. Geophys. Res.* **85**(A4), 1669. DOI.

Bobra, M.G., Couvidat, S.: 2015, Solar flare prediction using SDO/HMI vector magnetic field data with a machine-learning algorithm. *Astrophys. J.* **798**, 135. DOI. ADS.

Bobra, M.G., Sun, X., Hoeksema, J.T., Turmon, M., Liu, Y., Hayashi, K., Barnes, G., Leka, K.: 2014, The helioseismic and magnetic imager (hmi) vector magnetic field pipeline: sharps–space-weather hmi active region patches. *Solar Phys.* **289**(9), 3549. DOI.

Burlaga, L., Sittler, E., Mariani, F., Schwenn, R.: 1981, Magnetic loop behind an interplanetary shock: voyager, helios, and imp 8 observations. *J. Geophys. Res.* **86**(A8), 6673. DOI.

Cane, H.V.: 2000, Coronal mass ejections and Forbush decreases. *Space Sci. Rev.* **93**(1), 55. DOI.
Carpenter, D.L.: 1963, Whistler evidence of a knee in the magnetospheric ionization density profile. *J. Geophys. Res.* **68**(6), 1675. DOI.
Carpenter, D., Anderson, R.: 1992, An isee/whistler model of equatorial electron density in the magnetosphere. *J. Geophys. Res.* **97**(A2), 1097. DOI.
Carter, B.A., Yizengaw, E., Pradipta, R., Weygand, J.M., Piersanti, M., Pulkkinen, A., Moldwin, M.B., Norman, R., Zhang, K.: 2016, Geomagnetically induced currents around the world during the 17 March 2015 storm. *J. Geophys. Res.* **121**(10), 10,496. DOI.
Cesaroni, C., Spogli, L., Alfonsi, L., De Franceschi, G., Ciraolo, L., Monico, J.F.G., Scotto, C., Romano, V., Aquino, M., Bougard, B.: 2015, L-band scintillations and calibrated total electron content gradients over Brazil during the last solar maximum. *J. Space Weather Space Clim.* **5**, A36. DOI.
Chappell, C., Harris, K., Sharp, G.: 1970, The morphology of the bulge region of the plasmasphere. *J. Geophys. Res.* **75**(19), 3848. DOI.
Chi, P., Russell, C., Peterson, W., Le, G., Angelopoulos, V., Reeves, G., Moldwin, M., Chun, F.: 2000, Plasmaspheric depletion and refilling associated with the September 25, 1998 magnetic storm observed by ground magnetometers at $l = 2$. *Geophys. Res. Lett.* **27**, 633. DOI.
Chisham, G., Lester, M., Milan, S.E., Freeman, M.P., Bristow, W.A., Grocott, A., McWilliams, K.A., Ruohoniemi, J.M., Yeoman, T.K., Dyson, P.L., Greenwald, R.A., Kikuchi, T., Pinnock, M., Rash, J.P.S., Sato, N., Sofko, G.J., Villain, J.-P., Walker, A.D.M.: 2007, A decade of the super dual auroral radar network (superdarn): scientific achievements, new techniques and future directions. *Surv. Geophys.* **28**(1), 33. DOI.
Ciraolo, L., Azpilicueta, F., Brunini, C., Meza, A., Radicella, S.: 2007, Calibration errors on experimental slant total electron content (tec) determined with gps. *J. Geod.* **81**(2), 111. DOI.
Consolini, G., De Michelis, P.: 2005, Local intermittency measure analysis of ae index: the directly driven and unloading component. *Geophys. Res. Lett.* **32**(5), L05101. DOI.
Cristaldi, A., Guglielmino, S.L., Zuccarello, F., Romano, P., Falco, M., van der Voort, L.R., de la Cruz Rodríguez, J., Ermolli, I., Criscuoli, S.: 2014, Dynamic properties along the neutral line of a delta spot inferred from high-resolution observations. *Astrophys. J.* **789**(2), 162. DOI.
Daglis, I., Axford, W., Sarris, E., Livi, S., Wilken, B.: 1997, Particle acceleration in geospace and its association with solar events. *Solar Phys.* **172**(1–2), 287. DOI.
Davis, T.N., Sugiura, M.: 1966, Auroral electrojet activity index AE and its universal time variations. *J. Geophys. Res.* **71**(3), 785. DOI.
De Michelis, P., Tozzi, R., Consolini, G.: 2010, Principal components' features of mid-latitude geomagnetic daily variation. *Ann. Geophys.* **28**(12), 2213. DOI.
Dessler, A.J., Parker, E.N.: 1959, Hydromagnetic theory of geomagnetic storms. *J. Geophys. Res.* **64**(12), 2239. DOI.
Dmitriev, A., Chao, J.-K., Thomsen, M., Suvorova, A.: 2005, Geosynchronous magnetopause crossings on 29 – 31 October 2003. *J. Geophys. Res.* **110**(A8). DOI.
Dominici, P., Cander, L.R., Zolesi, B.: 1997, On the origin of medium-period ionospheric waves and their possible modelling: a short review. *Ann. Geophys.* **40**(5), 338. DOI.
Dungey, J.W.: 1961, Interplanetary magnetic field and the auroral zones. *Phys. Rev. Lett.* **6**(2), 47. DOI.
Ermolli, I., Giorgi, F., Romano, P., Zuccarello, F., Criscuoli, S., Stangalini, M.: 2014, Fractal and multifractal properties of active regions as flare precursors: a case study based on SOHO/MDI and SDO/HMI observations. *Solar Phys.* **289**, 2525. DOI.
Falconer, D.A., Moore, R.L., Gary, G.A.: 2002, Correlation of the coronal mass ejection productivity of solar active regions with measures of their global nonpotentiality from vector magnetograms: baseline results. *Astrophys. J.* **569**, 1016. DOI. ADS.
Fejer, B.G., Jensen, J.W., Su, S.-Y.: 2008, Seasonal and longitudinal dependence of equatorial disturbance vertical plasma drifts. *Geophys. Res. Lett.* **35**(20). DOI.
Fejer, B.G., Scherliess, L.: 1995, Time dependent response of equatorial ionospheric electric fields to magnetospheric disturbances. *Geophys. Res. Lett.* **22**(7), 851. DOI.
Feldstein, Y.I., Zaitzev, A.N.: 1968, Quiet and disturbed solar-daily variations of magnetic field at high latitudes during the igy. *Tellus* **20**(2), 338. DOI.
Forbush, S.E.: 1937, On diurnal variation in cosmic-ray intensity. *Terr. Magn. Atmos. Electr.* **42**(1), 1. DOI.
Freeland, S., Handy, B.: 1998, Data analysis with the solarsoft system. *Solar Phys.* **182**(2), 497. DOI.
Friis-Christensen, E., Lühr, H., Knudsen, D., Haagmans, R.: 2008, Swarm – an Earth observation mission investigating geospace. *Adv. Space Res.* **41**(1), 210. DOI.
Georgoulis, M.K.: 2005, A new technique for a routine azimuth disambiguation of solar vector magnetograms. *Astrophys. J. Lett.* **629**(1), L69. DOI.
Georgoulis, M.K., LaBonte, B.J.: 2004, Vertical Lorentz force and cross-field currents in the photospheric magnetic fields of solar active regions. *Astrophys. J.* **615**(2), 1029. DOI.

Getley, I., Duldig, M., Smart, D., Shea, M.: 2005, The applicability of model based aircraft radiation dose estimates. *Adv. Space Res.* **36**(9), 1638. DOI.
Giacalone, J., Kóta, J.: 2006, Acceleration of solar-energetic particles by shocks. *Space Sci. Rev.* **124**(1–4), 277. DOI.
Giorgi, F., Ermolli, I., Romano, P., Stangalini, M., Zuccarello, F., Criscuoli, S.: 2015, The signature of flare activity in multifractal measurements of active regions observed by SDO/HMI. *Solar Phys.* **290**, 507.
Gonzalez, W.D., Tsurutani, B.T., de Gonzalez, A.L.C.: 1999, Interplanetary origin of geomagnetic storms. *Space Sci. Rev.* **88**(3–4), 529. DOI.
Gonzalez, W.D., Joselyn, J.A., Kamide, Y., Kroehl, H.W., Rostoker, G., Tsurutani, B.T., Vasyliunas, V.M.: 1994, What is a geomagnetic storm? *J. Geophys. Res.* **99**(A4), 5771. DOI.
Gosain, S., Venkatakrishnan, P.: 2010, The evolution of the twist shear and dip shear during x-class flare of 2006 December 13: Hinode observations. *Astrophys. J. Lett.* **720**(2), L137. DOI.
Hoeksema, J.T., Liu, Y., Hayashi, K., Sun, X., Schou, J., Couvidat, S., Norton, A., Bobra, M., Centeno, R., Leka, K.D., Barnes, G., Turmon, M.: 2014, The helioseismic and magnetic imager (hmi) vector magnetic field pipeline: overview and performance. *Solar Phys.* **289**(9), 3483. DOI.
Hoff, J., Townsend, L., Zapp, E.: 2004, Interplanetary crew doses and dose equivalents: variations among different bone marrow and skin sites. *Adv. Space Res.* **34**(6), 1347. DOI.
Huang, N.E., Shen, Z., Long, S.R., Wu, M.C., Shih, H.H., Zheng, Q., Yen, N.-C., Tung, C.C., Liu, H.H.: 1998, The empirical mode decomposition and the Hilbert spectrum for nonlinear and non-stationary time series analysis. *Proc. Roy. Soc. A, Math. Phys.* **454**(1971), 903. DOI.
Huang, C.-S., Sazykin, S., Chau, J.L., Maruyama, N., Kelley, M.C.: 2007, Penetration electric fields: efficiency and characteristic time scale. *J. Atmos. Solar-Terr. Phys.* **69**(10), 1135. DOI.
Hundhausen, A.J.: 1993, Sizes and locations of coronal mass ejections: smm observations from 1980 and 1984-1989. *J. Geophys. Res., Space* **98**(A8), 13177. DOI.
Hunsucker, R.D.: 1992, Auroral and polar-cap ionospheric effects on radio propagation. *IEEE Antennas Propag.* **40**(7), 818. DOI.
Iucci, N., Levitin, A., Belov, A., Eroshenko, E., Ptitsyna, N., Villoresi, G., Chizhenkov, G., Dorman, L., Gromova, L., Parisi, M., *et al.*: 2005, Space weather conditions and spacecraft anomalies in different orbits. *Space Weather* **3**(1). DOI.
Jiang, C., Wu, S., Feng, X., Hu, Q.: 2016, Data-driven magnetohydrodynamic modelling of a flux-emerging active region leading to solar eruption. *Nat. Commun.* **7**. DOI.
Jing, J., Xu, Y., Cao, W., Liu, C., Gary, D., Wang, H.: 2016, Unprecedented fine structure of a solar flare revealed by the 1.6 m new solar telescope. *Sci. Rep.* **6**, 24319. DOI.
Joselyn, J.A., Tsurutani, B.T.: 1990, Geomagnetic sudden impulses and storm sudden commencements: a note on terminology. *Eos, Trans. Am. Geophys. Union* **71**(47), 1808. DOI.
Kale, Z., Mann, I., Waters, C., Goldstein, J., Menk, F., Ozeke, L.: 2007, Ground magnetometer observation of a cross-phase reversal at a steep plasmapause. *J. Geophys. Res.* **112**(A10). DOI.
Kamide, Y., Kokubun, S.: 1996, Two-component auroral electrojet: importance for substorm studies. *J. Geophys. Res.* **101**(A6), 13027. DOI.
Kennel, C.F., Edmiston, J.P., Russell, C.T., Scarf, F.L., Coroniti, F.V., Smith, E.J., Tsurutani, B.T., Scudder, J.D., Feldman, W.C., Anderson, R.R.: 1984a, Structure of the November 12, 1978, quasi-parallel interplanetary shock. *J. Geophys. Res.* **89**, 5436. DOI. ADS.
Kennel, C.F., Edmiston, J.P., Russell, C.T., Scarf, F.L., Coroniti, F.V., Smith, E.J., Tsurutani, B.T., Scudder, J.D., Feldman, W.C., Anderson, R.R.: 1984b, Structure of the November 12, 1978, quasi-parallel interplanetary shock. *J. Geophys. Res.* **89**, 5436. DOI. ADS.
Kocharov, L., Torsti, J.: 2002, Hybrid solar energetic particle events observed on board SOHO. *Solar Phys.* **207**(1), 149. DOI.
Kokubun, S.: 1983, Characteristics of storm sudden commencement at geostationary orbit. *J. Geophys. Res., Space* **88**(A12), 10025. DOI.
Kosugi, T., Matsuzaki, K., Sakao, T., Shimizu, T., Sone, Y., Tachikawa, S., Hashimoto, T., Minesugi, K., Ohnishi, A., Yamada, T., *et al.*: 2007, The hinode (solar-b) mission: an overview. *Solar Phys.* **243**(1), 3. DOI.
Laurenza, M., Cliver, E., Hewitt, J., Storini, M., Ling, A., Balch, C., Kaiser, M.: 2009, A technique for short-term warning of solar energetic particle events based on flare location, flare size, and evidence of particle escape. *Space Weather* **7**(4). DOI.
Lee, D.-Y., Lyons, L.R.: 2004, Geosynchronous magnetic field response to solar wind dynamic pressure pulse. *J. Geophys. Res., Space* **109**(A4), A04201. DOI.
Leka, K.D., Barnes, G.: 2003, Photospheric magnetic field properties of flaring versus flare-quiet active regions. I. Data, general approach, and sample results. *Astrophys. J.* **595**, 1277. DOI. ADS.
Leka, K.D., Barnes, G.: 2007, Photospheric magnetic field properties of flaring versus flare-quiet active regions. IV. A statistically significant sample. *Astrophys. J.* **656**, 1173. DOI. ADS.

Lemaire, J.F., Gringauz, K.I., Carpenter, D.L., Bassolo, V.: 2005, *The Earth's Plasmasphere*, Cambridge University Press, Cambridge, 18.
Lemen, J.R., Akin, D.J., Boerner, P.F., Chou, C., Drake, J.F., Duncan, D.W., Edwards, C.G., Friedlaender, F.M., Heyman, G.F., Hurlburt, N.E., *et al.*: 2011, The Atmospheric Imaging Assembly (AIA) on the Solar Dynamics Observatory (SDO). In: *The Solar Dynamics Observatory*, Springer, Berlin, 17.
Li, X., Roth, I., Temerin, M., Wygant, J.R., Hudson, M.K., Blake, J.B.: 1993, Simulation of the prompt energization and transport of radiation belt particles during the March 24, 1991 SSC. *Geophys. Res. Lett.* **20**(22), 2423. DOI.
Li, X., Baker, D., Elkington, S., Temerin, M., Reeves, G., Belian, R., Blake, J., Singer, H., Peria, W., Parks, G.: 2003, Energetic particle injections in the inner magnetosphere as a response to an interplanetary shock. *J. Atmos. Solar-Terr. Phys.* **65**(2), 233. DOI.
Lichtenberger, J., Clilverd, M.A., Heilig, B., Vellante, M., Manninen, J., Rodger, C.J., Collier, A.B., Jørgensen, A.M., Reda, J., Holzworth, R.H., Friedel, R., Simon-Wedlund, M.: 2013, The plasmasphere during a space weather event: first results from the plasmon project. *J. Space Weather Space* **3**, A23. DOI.
Lites, B., Casini, R., Garcia, J., Socas-Navarro, H.: 2007, A suite of community tools for spectro-polarimetric analysis. *Mem. Soc. Astron. Ital.* **78**, 148.
Lites, B., Akin, D., Card, G., Cruz, T., Duncan, D., Edwards, C., Elmore, D., Hoffmann, C., Katsukawa, Y., Katz, N., *et al.*: 2013, The hinode spectro-polarimeter. *Solar Phys.* **283**(2), 579. DOI.
Liu, Y.D., Hu, H., Wang, R., Yang, Z., Zhu, B., Liu, Y.A., Luhmann, J.G., Richardson, J.D.: 2015, Plasma and magnetic field characteristics of solar coronal mass ejections in relation to geomagnetic storm intensity and variability. *Astrophys. J.* **809**(2), L34. DOI.
Lorentzen, K., Mazur, J., Looper, M., Fennell, J., Blake, J.: 2002, Multisatellite observations of mev ion injections during storms. *J. Geophys. Res.* **107**(A9). DOI.
Lyu, L.-H.: 2002, *Space Weather Study Using Multipoint Techniques* **12**, Elsevier, Amsterdam, 22.
Mannucci, A., Tsurutani, B., Iijima, B., Komjathy, A., Saito, A., Gonzalez, W., Guarnieri, F., Kozyra, J., Skoug, R.: 2005, Dayside global ionospheric response to the major interplanetary events of October 29–30, 2003 "Halloween storms". *Geophys. Res. Lett.* **32**(12). DOI.
Menk, F., Kale, Z., Sciffer, M., Robinson, P., Waters, C., Grew, R., Clilverd, M., Mann, I.: 2014, Remote sensing the plasmasphere, plasmapause, plumes and other features using ground-based magnetometers. *J. Space Weather Space Clim.* **4**, A34. DOI.
Moldwin, M.B.: 1997, Outer plasmaspheric plasma properties: what we know from satellite data. *Space Sci. Rev.* **80**(1), 181. DOI.
Moran, T.G., Davila, J.M.: 2004, Three-dimensional polarimetric imaging of coronal mass ejections. *Science* **305**, 66. DOI. ADS.
Muella, M., Kherani, E., de Paula, E., Cerruti, A., Kintner, P., Kantor, I., Mitchell, C., Batista, I., Abdu, M.: 2010, Scintillation-producing Fresnel-scale irregularities associated with the regions of steepest tec gradients adjacent to the equatorial ionization anomaly. *J. Geophys. Res.* **115**(A3). DOI.
Nicolls, M., Kelley, M., Vlasov, M., Sahai, Y., Chau, J., Hysell, D., Fagundes, P., Becker-Guedes, F., Lima, W.: 2006, Observations and modeling of post-midnight uplifts near the magnetic equator. *Ann. Geophys.* **24**(5), 1317. DOI.
O'Brien, T., Moldwin, M.: 2003, Empirical plasmapause models from magnetic indices. *Geophys. Res. Lett.* **30**(4). DOI.
Park, C.: 1973, Whistler observations of the depletion of the plasmasphere during a magnetospheric substorm. *J. Geophys. Res.* **78**(4), 672. DOI.
Park, C.G.: 1974, Some features of plasma distribution in the plasmasphere deduced from Antarctic whistlers. *J. Geophys. Res.* **79**(1), 169. DOI.
Patel, V.L., Coleman, P.J.: 1970, Sudden impulses in the magnetosphere observed at synchronous orbit. *J. Geophys. Res.* **75**(34), 7255. DOI.
Pesnell, W.D., Thompson, B.J., Chamberlin, P.C.: 2012, The solar dynamics observatory (sdo). *Solar Phys.* **275**(1), 3. DOI.
Pesses, M.E., Tsurutani, B.T., Smith, E.J., van Allen, J.A.: 1979, Acceleration of energetic protons by interplanetary shocks. *J. Geophys. Res.* **84**, 7297. DOI. ADS.
Petrie, G.: 2012, The abrupt changes in the photospheric magnetic and Lorentz force vectors during six major neutral-line flares. *Astrophys. J.* **759**(1), 50. DOI.
Piersanti, M., Villante, U.: 2016, On the discrimination between magnetospheric and ionospheric contributions on the ground manifestation of sudden impulses. *J. Geophys. Res., Space* **121**(7), 6674. DOI.
Piersanti, M., Villante, U., Waters, C., Coco, I.: 2012, The 8 June 2000 ulf wave activity: a case study. *J. Geophys. Res., Space* **117**(A2). DOI.
Prölss, G.: 1995, *Ionospheric F-Region Storms*, *Handbook of Atmospheric Electrodynamics* **2**, 195.

Reames, D.V.: 1999, Particle acceleration at the sun and in the heliosphere. *Space Sci. Rev.* **90**(3–4), 413. DOI.
Reiff, P., Daou, A., Sazykin, S., Nakamura, R., Hairston, M., Coffey, V., Chandler, M., Anderson, B., Russell, C., Welling, D., *et al.*: 2016, Multispacecraft observations and modeling of the 22/23 June 2015 geomagnetic storm. *Geophys. Res. Lett.* **43**(14), 7311. DOI.
Reinisch, B.W., Galkin, I.A.: 2011, Global ionospheric radio observatory (giro). *Earth Planets Space* **63**(4), 377. DOI.
Rishbeth, H.: 1971, Polarization fields produced by winds in the equatorial f-region. *Planet. Space Sci.* **19**(3), 357. DOI.
Romano, P., Zuccarello, F.P., Guglielmino, S.L., Zuccarello, F.: 2014, Evolution of the magnetic helicity flux during the formation and eruption of flux ropes. *Astrophys. J.* **794**(2), 118. DOI.
Ruohoniemi, J.M., Baker, K.B.: 1998, Large-scale imaging of high-latitude convection with super dual auroral radar network hf radar observations. *J. Geophys. Res., Space* **103**(A9), 20797. DOI.
Ruohoniemi, J.M., Greenwald, R.A.: 1996, The response of high-latitude convection to a sudden southward imf turning. *Geophys. Res. Lett.* **25**(15), 2913. DOI.
Scherrer, P.H., Schou, J., Bush, R.I., Kosovichev, A.G., Bogart, R.S., Hoeksema, J.T., Liu, Y., Duvall, T.L., Zhao, J., Title, A.M., Schrijver, C.J., Tarbell, T.D., Tomczyk, S.: 2012, The helioseismic and magnetic imager (hmi) investigation for the solar dynamics observatory (sdo). *Solar Phys.* **275**(1), 207. DOI.
Schrijver, C.J.: 2007, A characteristic magnetic field pattern associated with all major solar flares and its use in flare forecasting. *Astrophys. J. Lett.* **655**, L117. DOI. ADS.
Schrijver, C.J.: 2009, Driving major solar flares and eruptions: a review. *Adv. Space Res.* **43**, 739. DOI. ADS.
Schrijver, C.J., DeRosa, M.L.: 2003, Photospheric and heliospheric magnetic fields. *Solar Phys.* **212**(1), 165. DOI.
Sckopke, N.: 1966, A general relation between the energy of trapped particles and the disturbance field near the Earth. *J. Geophys. Res.* **71**(13), 3125. DOI.
Shepherd, S., Greenwald, R., Ruohoniemi, J.: 2002, Cross polar cap potentials measured with super dual auroral radar network during quasi-steady solar wind and interplanetary magnetic field conditions. *J. Geophys. Res.* **107**(A7). DOI.
Shimizu, T., Lites, B.W., Bamba, Y.: 2014, High-speed photospheric material flow observed at the polarity inversion line of a δ-type sunspot producing an X5.4 flare on 2012 March 7. *Publ. Astron. Soc. Japan* **66**, S14. DOI. ADS.
Shue, J.-H., Song, P., Russell, C., Steinberg, J., Chao, J., Zastenker, G., Vaisberg, O., Kokubun, S., Singer, H., Detman, T., *et al.*: 1998, Magnetopause location under extreme solar wind conditions. *J. Geophys. Res.* **103**(A8), 17691. DOI.
Smith, E.J., Tsurutani, B.T., Rosenberg, R.L.: 1978, Observations of the interplanetary sector structure up to heliographic latitudes of 16°: pioneer 11. *J. Geophys. Res., Space* **83**(A2), 717. DOI.
Spogli, L., Cesaroni, C., Di Mauro, D., Pezzopane, M., Alfonsi, L., Musicò, E., Povero, G., Pini, M., Dovis, F., Romero, R., *et al.*: 2016, Formation of ionospheric irregularities over southeast Asia during the 2015 St. Patrick's Day storm. *J. Geophys. Res.* DOI.
Suvorova, A., Dmitriev, A., Chao, J.-K., Thomsen, M., Yang, Y.-H.: 2005, Necessary conditions for geosynchronous magnetopause crossings. *J. Geophys. Res.* **110**(A1). DOI.
Tsuneta, S., Ichimoto, K., Katsukawa, Y., Nagata, S., Otsubo, M., Shimizu, T., Suematsu, Y., Nakagiri, M., Noguchi, M., Tarbell, T., Title, A., Shine, R., Rosenberg, W., Hoffmann, C., Jurcevich, B., Kushner, G., Levay, M., Lites, B., Elmore, D., Matsushita, T., Kawaguchi, N., Saito, H., Mikami, I., Hill, L.D., Owens, J.K.: 2008, The solar optical telescope for the hinode mission: an overview. *Solar Phys.* **249**(2), 167. DOI.
Tsurutani, B.T., Lakhina, G.S.: 2014, An extreme coronal mass ejection and consequences for the magnetosphere and Earth. *Geophys. Res. Lett.* **41**(2), 287. DOI.
Tsurutani, B.T., Lin, R.P.: 1985, Acceleration of greater than 47 keV ions and greater than 2 keV electrons by interplanetary shocks at 1 AU. *J. Geophys. Res.* **90**, 1. DOI. ADS.
Tsurutani, B.T., Zhou, X.-Y.: 2003, Interplanetary shock triggering of substorms: wind and polar. *Adv. Space Res.* **31**(4), 1063. DOI.
Tsurutani, B.T., Smith, E.J., Pyle, K.R., Simpson, J.A.: 1982, Energetic protons accelerated at corotating shocks – pioneer 10 and 11 observations from 1 to 6 AU. *J. Geophys. Res.* **87**, 7389. DOI. ADS.
Tsurutani, B.T., Gonzalez, W.D., Tang, F., Akasofu, S.I., Smith, E.J.: 1988, Origin of interplanetary southward magnetic fields responsible for major magnetic storms near solar maximum (1978 – 1979). *J. Geophys. Res.* **93**(A8), 8519. DOI.
Tsurutani, B., Judge, D., Guarnieri, F., Gangopadhyay, P., Jones, A., Nuttall, J., Zambon, G., Didkovsky, L., Mannucci, A., Iijima, B., *et al.*: 2005, The October 28, 2003 extreme euv solar flare and resultant extreme ionospheric effects: comparison to other Halloween events and the Bastille day event. *Geophys. Res. Lett.* **32**(3). DOI.

Tsurutani, B., Mannucci, A., Iijima, B., Abdu, M.A., Sobral, J.H.A., Gonzalez, W., Guarnieri, F., Tsuda, T., Saito, A., Yumoto, K., *et al.*: 2004, Global dayside ionospheric uplift and enhancement associated with interplanetary electric fields. *J. Geophys. Res.* **109**(A8). DOI.

Tsurutani, B., Verkhoglyadova, O., Mannucci, A., Lakhina, G., Li, G., Zank, G.: 2009, A brief review of "solar flare effects" on the ionosphere. *Radio Sci.* **44**(1). DOI.

Tsurutani, B., Verkhoglyadova, O., Mannucci, A., Saito, A., Araki, T., Yumoto, K., Tsuda, T., Abdu, M., Sobral, J., Gonzalez, W., *et al.*: 2008, Prompt penetration electric fields (ppefs) and their ionospheric effects during the great magnetic storm of 30 – 31 October 2003. *J. Geophys. Res.* **113**(A5). DOI.

Tsyganenko, N.: 2002, A model of the near magnetosphere with a dawn-dusk asymmetry 1. Mathematical structure. *J. Geophys. Res.* **107**(A8). DOI.

Tsyganenko, N.A., Sitnov, M.I.: 2005, Modeling the dynamics of the inner magnetosphere during strong geomagnetic storms. *J. Geophys. Res.* **110**(A3), A03208. DOI.

Tulasi Ram, S., Yokoyama, T., Otsuka, Y., Shiokawa, K., Sripathi, S., Veenadhari, B., Heelis, R., Ajith, K., Gowtam, V., Gurubaran, S., *et al.*: 2016, Duskside enhancement of equatorial zonal electric field response to convection electric fields during the St. Patrick's Day storm on 17 march 2015. *J. Geophys. Res.* DOI.

Valtonen, E.: 2005, Space weather effects on technology. In: *Space Weather*, Springer, Berlin, 241.

Vellante, M., Förster, M.: 2006, Inference of the magnetospheric plasma mass density from field line resonances: a test using a plasmasphere model. *J. Geophys. Res.* **111**(A11). DOI.

Vellante, M., Piersanti, M., Pietropaolo, E.: 2014, Comparison of equatorial plasma mass densities deduced from field line resonances observed at ground for dipole and igrf models. *J. Geophys. Res.* **119**(4), 2623. 2013JA019568. DOI.

Vellante, M., Piersanti, M., Heilig, B., Reda, J., Del Corpo, A.: 2014, Magnetospheric plasma density inferred from field line resonances: effects of using different magnetic field models. *2014 XXXIth URSI General Assembly Scien. Symp.*, 1. DOI.

Venkatesh, K., Tulasi Ram, S., Fagundes, P., Seemala, G.K., Batista, I.: 2017, Electrodynamic disturbances in the brazilian equatorial and low-latitude ionosphere on St. Patrick's Day storm of 17 March 2015. *J. Geophys. Res.* **122**(4), 4553. DOI.

Villante, U., Piersanti, M.: 2008, An analysis of sudden impulses at geosynchronous orbit. *J. Geophys. Res.* **113**(A8), A08213. DOI.

Villante, U., Piersanti, M.: 2009, Analysis of geomagnetic sudden impulses at low latitudes. *J. Geophys. Res.* **114**(A6), A06209. DOI.

Wang, H., Ewell Jr, M., Zirin, H., Ai, G.: 1994, Vector magnetic field changes associated with x-class flares. *Astrophys. J.* **424**, 436. DOI.

Wanliss, J.A., Showalter, K.M.: 2006, High-resolution global storm index: dst versus sym-h. *J. Geophys. Res.* **111**(A2), A02202. DOI.

Waters, C.L., Menk, F.W., Fraser, B.J.: 1991, The resonance structure of low latitude pc3 geomagnetic pulsations. *Geophys. Res. Lett.* **18**(12), 2293. DOI.

Welsch, B.T., Fisher, G.H., Sun, X.: 2013, A magnetic calibration of photospheric Doppler velocities. *Astrophys. J.* **765**, 98. DOI. ADS.

Woodman, R.F.: 1970, Vertical drift velocities and East–West electric fields at the magnetic equator. *J. Geophys. Res.* **75**(31), 6249. DOI.

Zhao, B., Wan, W., Liu, L., Igarashi, K., Nakamura, M., Paxton, L., Su, S.-Y., Li, G., Ren, Z.: 2008, Anomalous enhancement of ionospheric electron content in the Asian–Australian region during a geomagnetically quiet day. *J. Geophys. Res.* **113**(A11). DOI.

Zhou, X., Tsurutani, B.T.: 2001, Interplanetary shock triggering of nightside geomagnetic activity: substorms, pseudobreakups, and quiescent events. *J. Geophys. Res.* **106**(A9), 18957. DOI.

Žic, T., Vršnak, B., Temmer, M.: 2015, Heliospheric propagation of coronal mass ejections: drag-based model fitting. *Astrophys. J.* **218**, 32. DOI. ADS.

Zong, Q.-G., Reinisch, B., Song, P., Wei, Y., Galkin, I.: 2010, Dayside ionospheric response to the intense interplanetary shocks–solar wind discontinuities: observations from the digisonde global ionospheric radio observatory. *J. Geophys. Res.* **115**(A6). DOI.

Zuccarello, F., Romano, P., Farnik, F., Karlicky, M., Contarino, L., Battiato, V., Guglielmino, S., Comparato, M., Ugarte-Urra, I.: 2009, The x17. 2 flare occurred in noaa 10486: an example of filament destabilization caused by a domino effect. *Astron. Astrophys.* **493**(2), 629. DOI.

Zurbuchen, T.H., Richardson, I.G.: 2006, In-situ solar wind and magnetic field signatures of interplanetary coronal mass ejections. *Space Sci. Rev.* **123**, 31. DOI.